Contents

Part I
Particle Physics

The various groups of the *Physik-Institut* in the fields of particle physics are using for their experiments external accelerators at the large international research institutions PSI (Villigen), CERN (Genf), DESY (Hamburg) and Brookhaven. Further activities in the field of particle physics which are connected to questions of astroparticle physics and cosmology do not require accelerators or they are carried out at a nuclear reactor.

Most of these experiments are motivated in a broader sense by the fact that the present, highly successful standard model of particle physics cannot be understood as the ultimate truth for several, often cited reasons: There are too many free parameters, the origin of the masses and the nature of the neutrinos is not known, no symmetry is known which leads to the conservation of the lepton number separately for the three generations, the strong force is not yet unified with the electroweak force, the quantization of the gravitational force is unsolved, the question of the existence of other forces is still open.

A test of the standard model can be done by either a search for new particles or states of matter at medium and high energies, or complementary by a search with high precision at low energies for forbidden lepton number violating processes, a search for the magnetic moment of the neutrino at a reactor power station.

Mainly on the basis of this motivation Part I of the annual report presents the following experiments:

- Tests of lepton-flavor conservation at PSI
- Meson spectroscopy at LEAR with the Crystal Barrel
- Measurement of the neutrino magnetic moment at the Bugey nuclear reactor
- Particle physics at LHC/CMS
- Particle physics at DESY/HERA
- Rare kaon decays
- Neutrino masses and mixing
- Measurement of the gravitational constant G

1 Tests of Lepton-Flavor Conservation at PSI

R. Engfer, E.A. Hermes, G. Kurz, H. Pruys,
F. Riepenhausen, A. van der Schaaf and P. Wintz

in collaboration with III. Phys. Institut der RWTH Aachen and PSI Villigen.

One of the great mysteries in present-day particle physics is the origin of the generation pattern of quark and lepton states. Transitions between the generations, as observed in charged weak interactions among quarks, can be attributed to mixing of the quark eigenstates. Within the framework of the minimal Standard Model the mass degeneracy of the neutrino states precludes this mechanism in the leptonic sector, in accordance with the apparent conservation of leptonic generation number (lepton-flavor conservation, LFC).

Although various anomalies in the fluxes of solar, atmospheric and beam dump neutrinos may be interpreted in terms of neutrino oscillations, no convincing signal for the violation of LFC has been found so far. Searches for LFC-violating decay modes of charged leptons, mesons and Z^0 have resulted in upper limits only.

Most extensions of the Standard Model allow neutral interactions between the generations. Whereas higher order charged interactions among quarks lead to effective flavor-changing neutral currents (FCNC), i.e. responsible for the decay $b \to s\gamma$, FCNC's among leptons would yield an unambiguous signal for new physics.

Which LFC-violating mode gives the best constraints is model-dependent. For this reason many different searches are done in parallel and at PSI, for example, three different processes are studied:

- A search for muonium-antimuonium conversion with the SINDRUM I spectrometer resulted in an improvement in sensitivity by almost four orders of magnitude.
- A search for $\mu \to e$ conversion on titanium with the SINDRUM II spectrometer resulted in an upper limit on $B_{\mu e}$ of $6.1 \cdot 10^{-13}$, the lowest upper limit on any decay mode reached so far. A further improvement of the sensitivity by another order of magnitude depends on the question whether the PMC magnet will reach the required field of 1.2 Tesla.
- A letter of intent has been submitted to PSI describing a new search for $\mu \to e\gamma$ at the level of a few times 10^{-14}. This would be an improvement of the present sensitivity by three orders of magnitude.

1.1 $\mu \to e$ conversion in muonic atoms: the SINDRUM II project

Neutrinoless $\mu^- \to e^-$ conversion in muonic atoms, $\mu^-(A,Z) \to e^-(A,Z)$ with A mass number and Z atomic number, gives the best constraints on LFC violation in a large variety of models. For conversions leaving the nucleus in its ground state the nucleons act coherently, which boosts the conversion probability relative to the rate of the dominant process of nuclear muon capture.

Muonic atoms mostly reach their ground state before decaying by muon decay in orbit $\mu^-(A,Z) \to e^-\overline{\nu}_e\nu_\mu(A,Z)$ or nuclear muon capture $\mu^-(A,Z) \to \nu_\mu(A,Z-1)$. In the case of muonic titanium the capture probability amounts to $f^{\mathrm{Ti}}_{\mathrm{capt}} = 85.3\%$, which corresponds to a lifetime of 329 ns. In the usual convention the branching ratio for $\mu \to e$ conversion is quoted relative to the rate for nuclear muon capture:

$$B_{\mu e} \equiv \frac{\Gamma_{\mu^-(A,Z)\to e^-(A,Z)^{g.s.}}}{\Gamma_{\mu^-(A,Z)\mathrm{capture}}} \,. \tag{1.1}$$

Earlier calculations predicted a steady rise of the branching ratio until $Z \approx 30$, from where on it was expected to drop again. For this reason most experiments have been performed on medium-heavy nuclei. More recently it has been estimated that $B_{\mu e}$ may keep increasing with Z. The dependence of $B_{\mu e}$ on the normalized neutron excess $(N-Z)/(N+Z)$, with $N \equiv A-Z$, depends on the nature of the LFC-violating propagator. A model-independent analysis requires at least two measurements with significantly different values for $(N-Z)/(N+Z)$.

The signature of coherent $\mu^- \to e^-$ conversion is a monoenergetic electron which is emitted at the kinematical endpoint for bound muon decay, i.e. with an energy equal to the muon mass minus the muon binding energy and the kinetic energy of the recoiling atom.

There are several sources of electron background in the energy region around 100 MeV, involving either beam particles or cosmic rays. Beam-related background may originate from muons, pions or electrons in the beam. Muons may produce background by *muon decay in flight* or, after the formation of a muonic atom, by *muon decay in orbit* or *radiative muon capture*. Pions may produce background by *radiative pion capture*. Capture gammas produce electrons mostly through e^+e^- pair production inside the target. Electrons in the beam may produce background through scattering off the target.

The SINDRUM II experiment aims at a sensitivity of a few times 10^{-14} for the branching ratio of $\mu^- \to e^-$ conversion in muonic atoms. In a first stage data were taken on titanium and lead at the old μE1 beam line at PSI. Below we report on the results of the third and final measurement at the μE1 beam line, a renewed search for $\mu^- \to e^-$ conversion on titanium with a sensitivity below 10^{-12}. The result of a search in this data-set for $\mu^- \to e^+$ conversion was presented in last years annual report and was published recently [3].

The sensitivity of the experiment is limited by beam flux and purity. A dedicated beam was designed, aiming at 10^8 s^{-1} stopped μ^- and a π^- contamination below 10^{-10}. The major beam element, an 8.5 m long solenoid, reached superconductivity by the beginning of 1997, but could not yet be operated at fields above 0.75 T, which is 50% of the design value. For this reason it was decided to change the beam concept temporarily and tune the πE5 channel to stop 20-30 MeV/c cloud muons which require a field around 0.2 T only.

Presently a number of improvements is made to the magnet which may allow operation at the full field after the 1998 six months shutdown period.

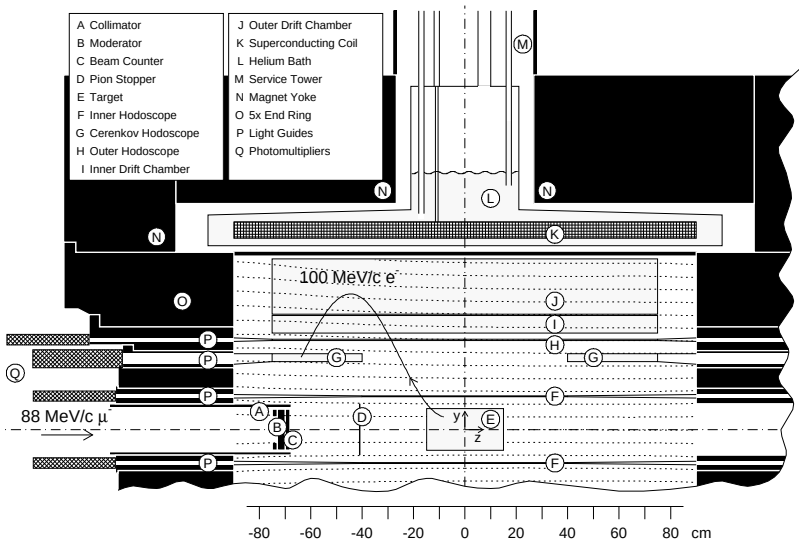

Figure 1.1: SINDRUM II

1.1.1 Search for $\mu \to e$ conversion on titanium

The SINDRUM II spectrometer (see Fig.1.1) consists of a set of concentric cylindrical detectors inside a superconducting solenoid. The muon beam enters the setup on the axis and traverses a CH_2 moderator and a plastic beam counter before reaching the target at the center. The particles of interest make 1-3 full turns before reaching a Čerenkov hodoscope. Two radial drift chambers are used for tracking.

The experiment was performed at the μE1 beam line at PSI. During a measurement life time of 50.4 days with beam switched on $(3.09 \pm 0.14) \times 10^{13}$ muons stopped in the target. Cosmic background was recorded during 44 days without beam.

Figure 1.2 shows an example of a reconstructed trajectory of an electron making two

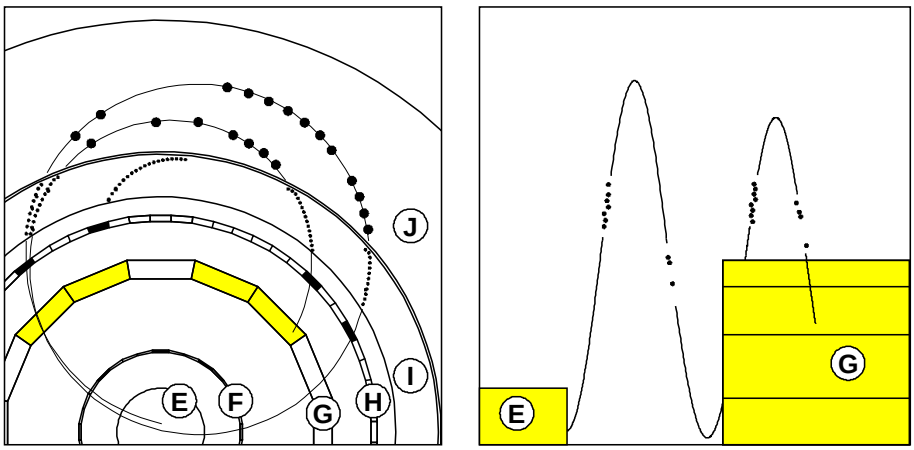

Figure 1.2: *Tracks left in the spectrometer by a 100 MeV/c e^-. The labeling of the detector components is as in Fig. 1.1.*

turns before reaching a Čerenkov hodoscope. The particle momentum and the origin of its trajectory are determined from a fit to the first revolution of the reconstructed helix. The events are then checked for additional detector signals characteristic for prompt and cosmic ray background.

In the spatial distribution of the point of closest approach, shown in Fig. 1.3, one easily recognizes the contours of the various objects in the beam.

Fig. 1.4 shows an example of a waveform trace taken from an radiative pion capture (RPC) event. In addition to the 700 ns history of the beam counter signal, a time marker and some periods of the cyclotron rf signal are recorded. The marker has a fixed time relation with the start signal of the hodoscope TDC's.

$\mu \to e$ conversion would lead to an enhancement of the number of events at the endpoint of the energy distribution for muon-induced electrons. Fig. 1.5 shows energy distributions for three stages in the event selection. The energy distribution of the final sample, which contains 3580 events with an energy above 85 MeV, falls steeply towards zero with an endpoint below 100 MeV. Both prompt and cosmic ray background could be removed completely. No candidate events have been found.

The upper limit on the branching ratio is calculated using:

$$\frac{\Gamma(\mu^- \mathrm{Ti} \to e^- \mathrm{Ti}^{\mathrm{g.s.}})}{\Gamma(\mu^- \mathrm{Ti}_{\mathrm{capture}})} < \frac{n^{\mu e}_{\mathrm{max}}(1 + n^{\mu e}_{\mathrm{max}}\sigma_r^2/2)}{f_{\mathrm{capt}} N_{\mathrm{stop}} \mathcal{E}^{\mu e}_{99\,\mathrm{MeV}}}\,, \tag{1.2}$$

where $n^{\mu e}_{\mathrm{max}} = 2.3$ is the upper limit on the number of candidate events, $f_{\mathrm{capt}} = 0.853$

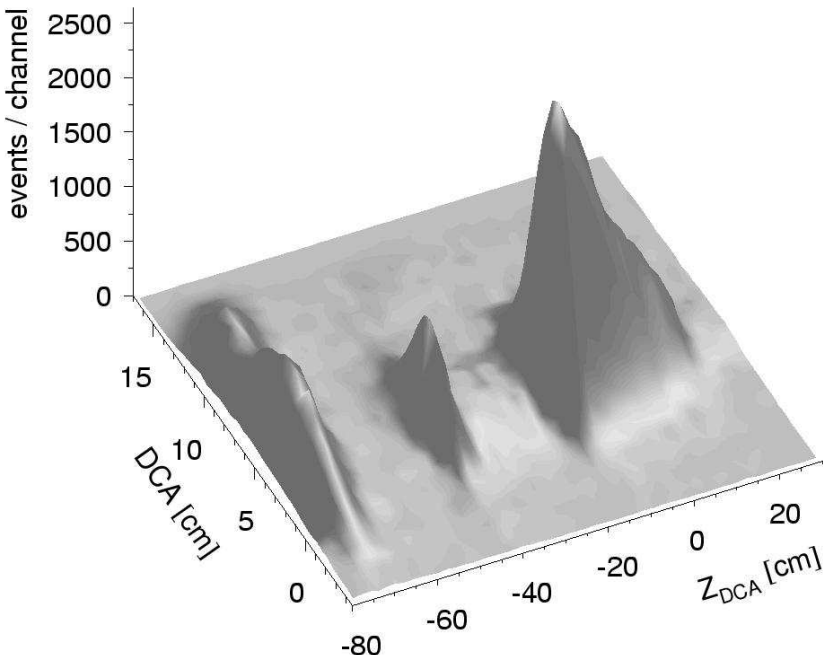

Figure 1.3: *Spatial distribution of the point of closest approach to the beam axis of the reconstructed trajectories showing event accumulations at the locations of the beam counter and collimator, the second moderator and the target (from the left).*

is the probability for nuclear muon capture on titanium, $N_{\rm stop} = (3.09 \pm 0.14) \times 10^{13}$ is the total number of muons stopping in the target during the life time of the experiment, $\mathcal{E}^{\mu e}_{99\,\rm MeV} = 0.146 \pm 0.012$ is the overall probability that a $\mu - e$ conversion in the target leads to the observation of an e^- event with energy above 99 MeV and σ_r is the relative uncertainty

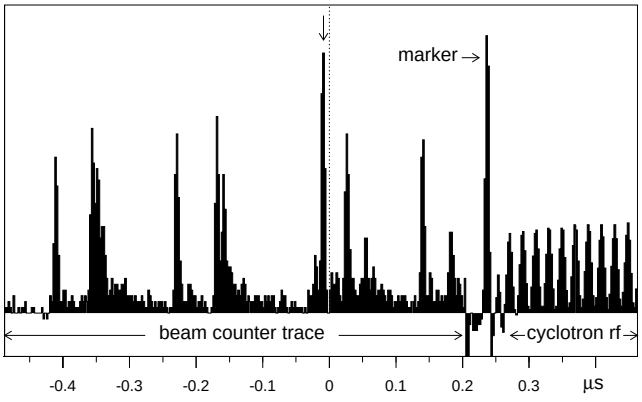

Figure 1.4: *Digitized waveform from a π^- induced event showing the beam counter trace, a time marker indicating the start signal for the hodoscope TDC's and the cyclotron rf signal. The position for prompt events at t=0 is calculated, assuming beam particles traveling between the beam counter and the target at light speed. Since pions move typically at one third of this velocity they cross the beam counter around t=-6 ns, where a large π signal is found.*

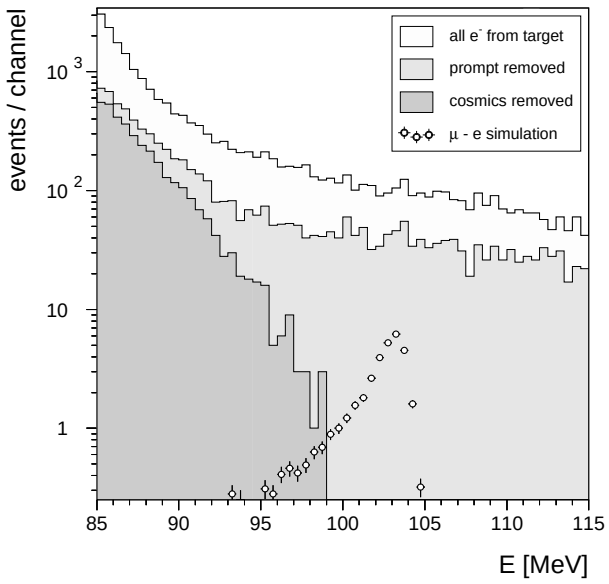

Figure 1.5: *Electron energy distribution at three stages of the event selection and as predicted by a GEANT simulation of $\mu - e$ conversion on titanium assuming $B_{\mu e} = 4 \cdot 10^{-12}$.*

of the denominator. One obtains:

$$\frac{\Gamma(\mu^- \mathrm{Ti} \to e^- \mathrm{Ti}^{\mathrm{g.s.}})}{\Gamma(\mu^- \mathrm{Ticapture})} < 6.1 \times 10^{-13} \quad (90\% \text{ C.L.}) \,, \tag{1.3}$$

which improves over the previous results [1] by a factor 7.

1.1.2 Search for $\mu \to e$ conversion on gold

These measurements were done during the second half of 1997 when it became clear that the PMC magnet could not be operated above 0.75 T. For this reason it was decided to use a cloud muon beam instead with a central momentum around 27 MeV/c. To transport this beam to the experimental target inside the spectrometer vacuum had to be maintained all the way from the pion production target to the exit of the spectrometer.

The only purpose of the PMC magnet was to reduce the pion flux by increasing the length of the πE5 channel. At this low momentum the beam can be stopped in a very thin target, which had a total mass of 10 g only, i.e. 100 times less than foreseen for the PMC mode. The reduced size leads to a reduction of the cosmic background and a better definition of the acceptance and trigger. The low mass has a large number of advantages:

- All background sources which scale with the target mass are reduced correspondingly:
  - radiative π and μ capture followed by asymmetric external e^+e^- production
  - the cosmic background component which requires a target interaction.
- The energy resolution is no longer given by the spread in target energy loss, but by the intrinsic spectrometer resolution of 1%.
- Signal losses by bremsstrahlung (at least 30% for the heavy targets) have become negligible.
- It is not necessary to limit the acceptance to the upstream hemisphere as is necessary in PMC operation due to the large scattering background in forward directions.

- The remaining background will be purely muon decay in orbit, rather than an uncertain mixture of various processes.

During a beam period with $1.6 \cdot 10^6$ mA·s about $2 \cdot 10^{12}$ muons stopped in the target. Since the overall efficiency is expected to raise by $\approx 50\%$ compared to the titanium measurement (no prompt veto, better energy resolution) the single-event sensitivity would be around $3 \cdot 10^{-12}$, or six times higher than achieved in our previous measurement on a heavy target [2].

References

[1] SINDRUM II Collab., C. Dohmen *et al.*, Phys. Lett. B **317**, 631 (1993).

[2] SINDRUM II Collab., W. Honecker *et al.*, Phys. Rev. Lett. **76** 200 (1996).

[3] SINDRUM II Collab., J. Kaulard *et al.*, Phys. Lett. B **422**, 334 (1998).

2 Meson Spectroscopy at LEAR with the Crystal Barrel

C. Amsler, M. Büchler, P. Giarritta, M. Heinzelmann, F. Ould-Saada,
C. Pietra, C. Regenfus and S. Spanier

In collaboration with: Academy of Science (Budapest); Universities of Bochum, Bonn, Hamburg, Karlsruhe, Mainz, München, Paris VI; CERN; Carnegie Mellon University (Pittsburgh); CRN (Strasbourg); QMWC (London); RAL; UC (Berkeley).

The Crystal Barrel experiment started data taking in late 1989 and was completed in autumn 1996 with the closure of LEAR. We collected very large samples of $\bar{p}p$ annihilations at low energy. The total number of minimum bias annihilations (i.e. requiring only an incident antiproton) collected at rest in liquid hydrogen is 10^8. Data were also taken in gaseous hydrogen (13 bar), in liquid deuterium and in liquid hydrogen with a multiplicity trigger requiring 0-prong or n-prong with long tracks in the jet drift chamber. Since 0-prong occur with a probability of 4%, the 0-prong data correspond to 6.3×10^8 annihilations. In addition, we collected data with specialized triggers enhancing specific final states. Data were also taken with antiprotons annihilating in flight between 600 and 1900 MeV/c.

The physics emphasis was (i) in the study of the annihilation mechanism and (ii) on a search for new mesons, in particular still missing $q\bar{q}$ states and glueballs. A comprehensive review of all Crystal Barrel results published until the end of 1997 can be found in ref. [1]. In this report we shall describe two important results achieved in 1997, (i) a confirmation of the isovector (isospin 1) scalar meson $a_0(1450)$ discovered earlier by our collaboration and (ii) the evidence for the exotic meson $\hat{\rho}(1405)$ with quantum numbers incompatible with a $q\bar{q}$ state.

2.1 Confirmation of $a_0(1450)$

Crystal Barrel has discovered a scalar ($J^P = 0^+$) meson decaying to $\eta\pi$ in the annihilation channel $\bar{p}p \to \pi^0\pi^0\eta$, with mass 1450 $\pm$ 40 MeV and width 270 $\pm$40 MeV [2]. This state was then also observed to decay into $\eta'\pi$ in the annihilation channel $\pi^0\pi^0\eta'$ [3]. The relative branching ratio $\eta'\pi/\eta\pi$ was found to be in good agreement with predictions from SU(3), assuming that $a_0(1450)$ is a quark-antiquark meson. Therefore two isovectors, $a_0(980)$ and $a_0(1450)$, compete for being the π-like $q\bar{q}$ state of the 0^+ $q\bar{q}$ ground state mesons. The $a_0(980)$ is generally believed to be a $K\bar{K}$ molecule and hence $a_0(1450)$ defines the mass scale for the 0^+ $q\bar{q}$ mesons.

According to the quark model nine mesons should build up the 0^+ ground states: three isovectors $a_0(1450)$ (a_0^+, a_0^-, a_0^0), the four well known $K_0^*(1430)$ (K_0^{*+}, K_0^{*-}, K_0^{*0}, $\overline{K_0^{*0}}$) and two isoscalars (isospin 0). Crystal Barrel has established two isoscalars, $f_0(1370)$ and $f_0(1500)$. The $f_0(1500)$ has been discovered by us and has become one of the best established meson resonances. It decays into $\pi^0\pi^0$ [4], $\eta\eta$ [5], $\eta\eta'$ [6], $4\pi^0$ [7] and $K\bar{K}$ [8]. The decay branching ratio of both $f_0(1370)$ and $f_0(1500)$ into $K\bar{K}$ have been observed, but are much too small and incompatible with either state having a large $s\bar{s}$ content [8, 9]. Therefore $f_0(1370)$ and $f_0(1500)$ cannot both belong to the 0^+ nonet while the $s\bar{s}$ meson still remains to be found.

Lattice gauge theories predict the ground state glueball - a 0^+ - state, to lie around 1500 MeV. This and the fact that $f_0(1500)$ is narrow ($\simeq$ 100 MeV) compared to the other 0^+ states led to the conclusion that $f_0(1500)$ is the supernumerary meson in the nonet, most likely the ground state glueball. A detailed discussion can be found in ref. [10].

This conclusion rests on the crucial fact that the $f_0(1500)$ coupling to $K\bar{K}$ is indeed small. The branching ratio to $K\bar{K}$ was determined from a study of the annihilation channel $K_L K_L \pi^0$ [8, 9]. However, $f_0(1370)$, $f_0(1500)$ and $a_0(1450)$ all contribute to this final state and therefore their $K\bar{K}$ branching ratios cannot be determined independently, due to interferences. Nonetheless, the small coupling to $K\bar{K}$ could be derived by fixing the $a_0(1450)$ contribution to about 10%. This number was derived from our rate for $a_0(1450) \to \eta\pi$ [2], using SU(3).

On the other hand, the isoscalar resonances $f_0(1370)$ and $f_0(1500)$ do not contribute to the channel $\bar{p}p \to \pi^{\pm} K^{\mp} K_L$. This channel therefore allows a direct measurement of the $a_0(1450)$ contribution to $K\bar{K}\pi$. Crystal Barrel has studied the reaction $\bar{p}p \to \pi^{\pm} K^{\mp} K_L$ with a non-interacting K_L in the barrel [11, 12]. This channel is selected from 2-prong data by requiring exactly two clusters in the CsI barrel from $\pi^{\pm}$ and $K^{\mp}$. Particle identification is achieved by measuring the ionisation in the drift chamber and a (1C) kinematic fit which ensures momentum and energy conservation. The Dalitz plot (Fig. 2.1) has been corrected for background and acceptance and for the K_L interaction probability.

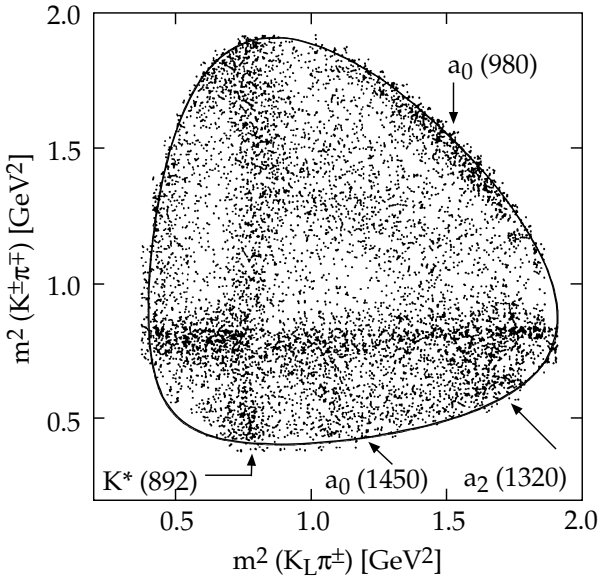

Figure 2.1: $\pi^{\pm} K^{\mp} K_L$ Dalitz plot (11,373 events).

The Dalitz plot shows clear signals from $K^*(892) \to K\pi$, $a_2(1320)$ and $a_0(980) \to \eta\pi$. The amplitude analysis did not provide a satisfactory description of the Dalitz plot and the fitted $a_2(1320)$ mass, 1290 MeV, was significantly lower than the accepted well known value (1318 MeV). A substantial improvement in the χ^2 (Fig. 2.2) was obtained when introducing the $a_0(1450) \to K\bar{K}$ with an optimum contribution of (10.8 ± 2.0) %, in accord with the SU(3) assumptions in ref. [11, 12]. The mass and width are 1480 ± 30 and 265 ± 15 MeV, respectively, in agreement with the $\eta\pi$ decay mode [2]. The $a_2(1320)$ mass now becomes compatible with the standard value.

From SU(3) one expects a ratio of branching ratios [10]

$$\frac{\Gamma(a_0^{\pm}(1450) \to K^{\pm} K^0)}{\Gamma(a_0^0(1450) \to \eta\pi^0)} = 0.72 \pm 0.03, \tag{2.1}$$

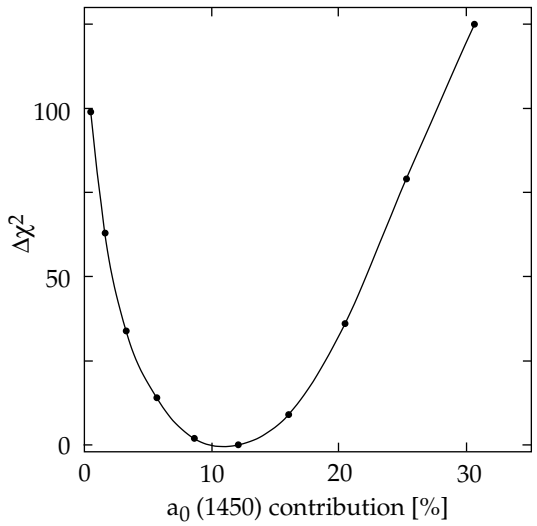

Figure 2.2: χ^2 dependence of the fractional contribution from $a_0(1450)$ to $\pi^{\pm}K^{\mp}K_L$.

while Crystal Barrel finds

$$\frac{B(a_0^{\pm}(1450) \to K^{\pm}K^0)}{B(a_0^0(1450) \to \eta\pi^0)} = 0.88 \pm 0.23. \tag{2.2}$$

The signals in $K\bar{K}$ and $\eta\pi$ are therefore compatible for a $q\bar{q}$ isovector scalar state. This establishes the existence of $a_0(1450)$ which has now been observed to decay into $\eta\pi$, $\eta'\pi$ and $K\bar{K}$ with consistent rates. Furthermore, its contribution of about 10% to $K\bar{K}\pi$ confirms the small coupling of $f_0(1370)$ and $f_0(1500)$ to $K\bar{K}$ that was predicted from $K_LK_L\pi^0$ data.

2.2 Evidence for $\hat{\rho}(1405)$

Quantum number conservation implies that a meson with quantum numbers $J^{PC} = 1^{-+}$ does not couple to $q\bar{q}$ and therefore the discovery of such a state would prove unambiguously the existence of exotic (non-$q\bar{q}$) mesons. Apart from glueballs, exotic mesons made of $q\bar{q}$ and a valence gluon (the so-called $q\bar{q}g$ hybrids) are also predicted by QCD. According to lattice gauge theories the lightest hybrid is a $J^{PC} = 1^{-+}$ state and lies around 2000 MeV. However, the bag model predicts a 1^{-+} hybrid meson at a much lower mass, around 1400 MeV.

A 1^{-+} hybrid in this mass region would decay to $\eta\pi$ (and $\eta'\pi$), where the two pseudoscalars are in a relative P-wave. This state would be isovector and hence could not be confused with a glueball, which is isoscalar. A candidate, $\hat{\rho}(1405)$, with a mass of 1370 $^{+52}_{-34}$ MeV and a width of 385 $^{+76}_{-112}$ MeV has been reported in the partial wave analysis of $\pi^-p \to \eta\pi^-p$ at 18 GeV [13].

Crystal Barrel has searched for a resonance in the $\eta\pi$ P-wave in $\bar{p}n$ annihilation into $\pi^-\pi^0\eta$, using a liquid deuterium target [14]. Events with a single π^- and $\pi^0\eta \to 4\gamma$ were selected from an 8.1 million 1-prong triggered data sample in liquid deuterium. The single track requirement restricts the spectator proton momentum to less than 200 MeV/c under which protons do not escape from the target. A 3C fit was applied to select $\pi^-\pi^0\eta$ with a missing proton. The missing proton momentum was then limited to 100 MeV/c. This procedure permits the channel $\pi^-\pi^0\eta$ to be treated as quasifree, i.e. insensitive to final state rescattering with the spectator proton.

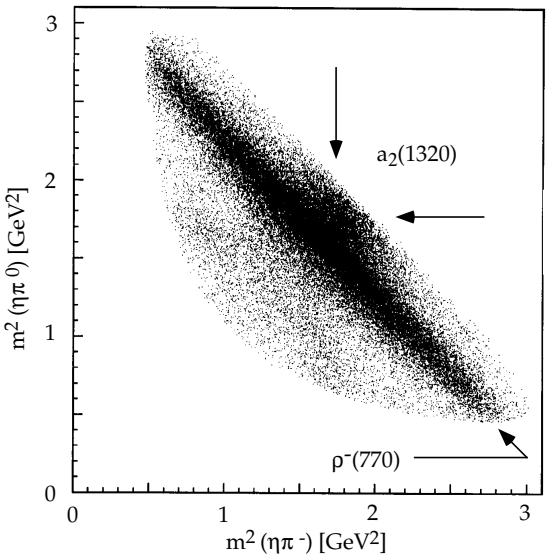

Figure 2.3: Dalitz plot of $\bar{p}n \to \pi^-\pi^0\eta$.

The Dalitz plot from the resulting 52,567 events is shown in Fig. 2.3. Conspicuous is the strong production of ρ^- and the accumulation of events in the $\eta\pi$ mass regions around 1300 MeV but only above the ρ band. This points to the presence of destructive interferences between $a_2(1320)$ and some other amplitude. A partial wave analysis was performed, introducing contributions from $\rho^-(770) \to \pi^-\pi^0$ and $a_2(1320) \to \eta\pi$. Contributions from other $q\bar{q}$ mesons were found to be negligible. The fit could not describe the observed interference pattern in Fig. 2.3. The inclusion of a resonant $\eta\pi$ P-wave led, however, to a good description of the data. The Breit-Wigner mass and width of the 1^{-+} resonance are

$$\hat{\rho}(1405): \; m = 1400 \pm 28, \; \Gamma = 310 \; ^{+71}_{-58} \text{ MeV}. \tag{2.3}$$

The resonance contributes about 11% to the Dalitz plot. It interferes with both $a_2(1320)$ and $\rho^-(770)$. The accumulation of events above the ρ (Fig. 2.3) leads to a forward/backward asymmetry in the $\eta\pi$ rest frame along the $a_2(1320)$ band.

These findings are consistent with the observation of an exotic 1^{-+} resonance in the 1400 MeV mass region. Mass and width are in good agreement with Thompson et al. [13]. However, an adequate fit can also be obtained with a 1 GeV broad enhancement in the $\eta\pi$ P-wave, coupling to the inelastic channel $f_1(1285)\pi$ and generating a distortion around threshold at 1420 MeV. This should be clarified by measuring the branching ratio for $f_1(1285)\pi$ production in deuterium. If not a threshold effect, this meson could be a hybrid but also a four-quark state. A measurement of the partial width into $\eta'\pi$ would help to distinguish between the two alternatives.

We note that another hybrid candidate, $\eta_2(1870)$, with the (non-exotic) quantum numbers $J^{PC} = 2^{-+}$ has been reported earlier by Crystal Barrel [15]. It decays into $\pi^0\pi^0\eta$ and is observed in $\bar{p}p$ annihilation into $3\pi^0\eta$ with 1.9 GeV/c antiprotons. Crystal Barrel finds the dominant decay modes $a_2^0(1320)\pi^0$ and $f_2(1270)\eta$. The ratio of partial widths is is in good agreement with the predicted ratio for a 2^{-+} hybrid meson [16].

References

[1] C. Amsler, Rev. Mod. Phys. (in print)

[2] C. Amsler *et al.*, Phys. Lett. **B 333** (1994) 277

[3] A. Abele *et al.*, Phys. Lett. **B 404** (1997) 179

[4] C. Amsler *et al.*, Phys. Lett. **B 342** (1995) 433

[5] C. Amsler *et al.*, Phys. Lett. **B 353** (1995) 571

[6] C. Amsler *et al.*, Phys. Lett. **B 340** (1994) 259

[7] A. Abele *et al.*, Phys. Lett. **B 380** (1996) 453

[8] A. Abele *et al.*, Phys. Lett. **B 385** (1996) 425

[9] S.v. Dombrowski, Ph.D. thesis, University of Zurich (1996)

[10] C. Amsler C. and F.E. Close, Phys. Rev. **D 53** 1996) 295; see also Phys. Lett. **B 353** (1995) 385

[11] M. Heinzelmann, Diploma thesis, University of Zurich (1996)

[12] A. Abele *et al.*, Phys. Rev. **D** (in print)

[13] D.R. Thompson *et al.*, Phys. Rev. Lett. **79** (1997) 1630

[14] A. Abele *et al.*, Phys. Lett. **B** (in print)

[15] J. Adomeit *et al.*, Z. Phys. **C 71** (1996) 227

[16] F.E. Close and P.R. Page, Nucl. Phys. **B 443** (1995) 233

3 Measurement of the Neutrino Magnetic Moment at the Bugey Nuclear Reactor

C. Amsler, P. Giarritta, M. Heinzelmann, O. Link, and F. Ould-Saada

In collaboration with Universität Bochum, Institut des Sciences Nucléaires (Grenoble), Université de Neuchâtel, Università di Padova
(MUNU Collaboration)

The MUNU experiment studies low energy $\overline{\nu}_e e^-$ elastic scattering at the Bugey nuclear power plant (2.8 GW thermal power) near Lyon. Its aim is to improve on the present laboratory upper limit for the magnetic moment of the electron neutrino ($1.8 \times 10^{-10} \mu_B$) by an order of magnitude. A magnetic moment of the order of a few 10^{-11} μ_B would lead to spin precession in the solar magnetic field [1] and could explain the deficit of solar neutrinos.

The motivations to perform such an experiment are as follows:

- Models of stellar evolution or the neutrino pulse from supernova SN 1987A set upper limits which are an order of magnitude smaller than can be achieved by our laboratory experiment. However, one should stress that the upper limit from SN 1987A ($< 10^{-12} \mu_B$) applies to Dirac and not to Majorana neutrinos.
- The earlier Savannah plant data [2] - together with today's knowledge of ^{235}U reactor spectra - point to a finite magnetic moment in the range $(2 - 4) \times 10^{-10} \mu_B$ [3].
- By measuring for the first time the angular distribution of $\overline{\nu}_e e^-$ scattering around 1 MeV neutrino energy we will determine the Weinberg angle with a precision of 5%, comparable to that achieved in high energy $\nu_\mu e^-$ scattering.

In contrast to previous experiments, we measure both the angle and the energy of the recoil electron. In the laboratory the electron is emitted into the forward hemisphere but the magnetic moment contribution increases with increasing recoil angle (and therefore with decreasing electron energy). Hence a low energy threshold for detecting the electron is essential. Our proposal assumed a threshold of 500 keV, determined by background. The background (isotropic and expected to be 4 events/day) can be measured with reactor on by looking at events with electrons emitted into the backward hemisphere - this is where the measurement of the recoil angle is particularly useful. Another advantage of measuring both the angle and the energy of the electron is the capability to reconstruct the incident neutrino energy.

The expected signal rate is 10 events/day if $\mu_\nu = 0$ and 13 events/day if $\mu_\nu = 10^{-10} \mu_B$. If background permits, we will lower the electron threshold and reduce the pressure to increase the track lengths. For example, with a threshold of 100 keV the signal rate would increase to 40, respectively 20 events/day. This would allow a measurement of the magnetic moment at the level of $10^{-11} \mu_B$ in one year of data taking.

The detector is located in the basement below reactor Nr. 5 at a distance of 18.6 m from the core, where the flux of cosmic ray muons is attenuated by 20 m of water equivalent. The intensity of antineutrinos reaching the detector is 10^{13} s^{-1} cm^{-2}. The detector consists of a time projection chamber (TPC) filled with CF_4 gas at 5 bar, 158 cm long and 90 cm in diameter. CF_4 is a high density gas which does not contain free protons. Thus the otherwise overwhelming inverse β-decay $\overline{\nu}_e p \rightarrow e^+ n$ does not occur. The TPC is surrounded by an anticompton shield (NE235 based liquid scintillator, attenuation length of 8 m at 430 nm), 50 cm thick, to convert and veto γ-rays which scatter in the gas and generate low energy recoil electrons. The scintillation light is detected by 48 EMI 8" photomultipliers, 24 on each

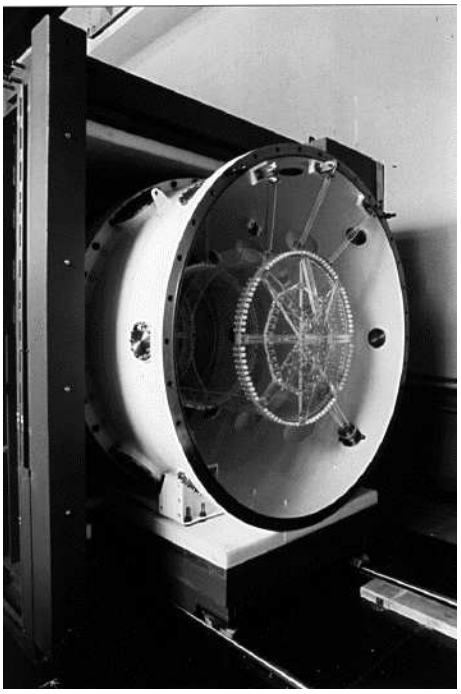

Figure 3.1: View of the TPC suspended in the scintillator tank.

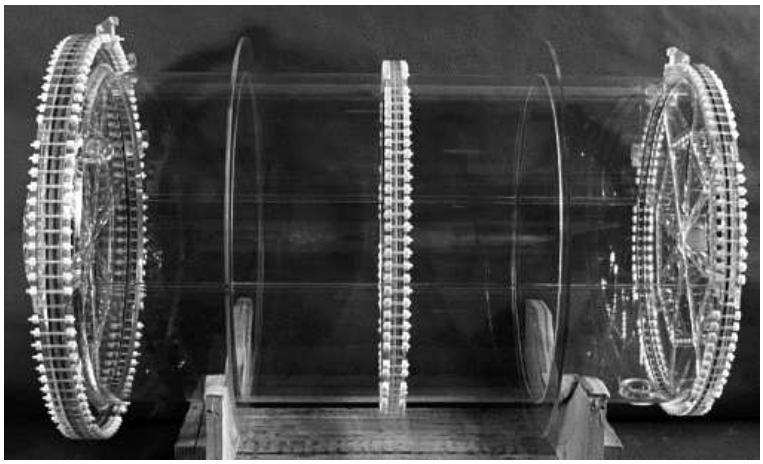

Figure 3.2: The acrylic vessel of the TPC.

lid. The liquid scintillator tank is shielded by 15 cm of lead. Neutrons generated by muon capture in the lead are attenuated and absorbed by 8 cm thick CH_2 plates covered with B_4C sheets. Details on the apparatus can be found in ref. [4].

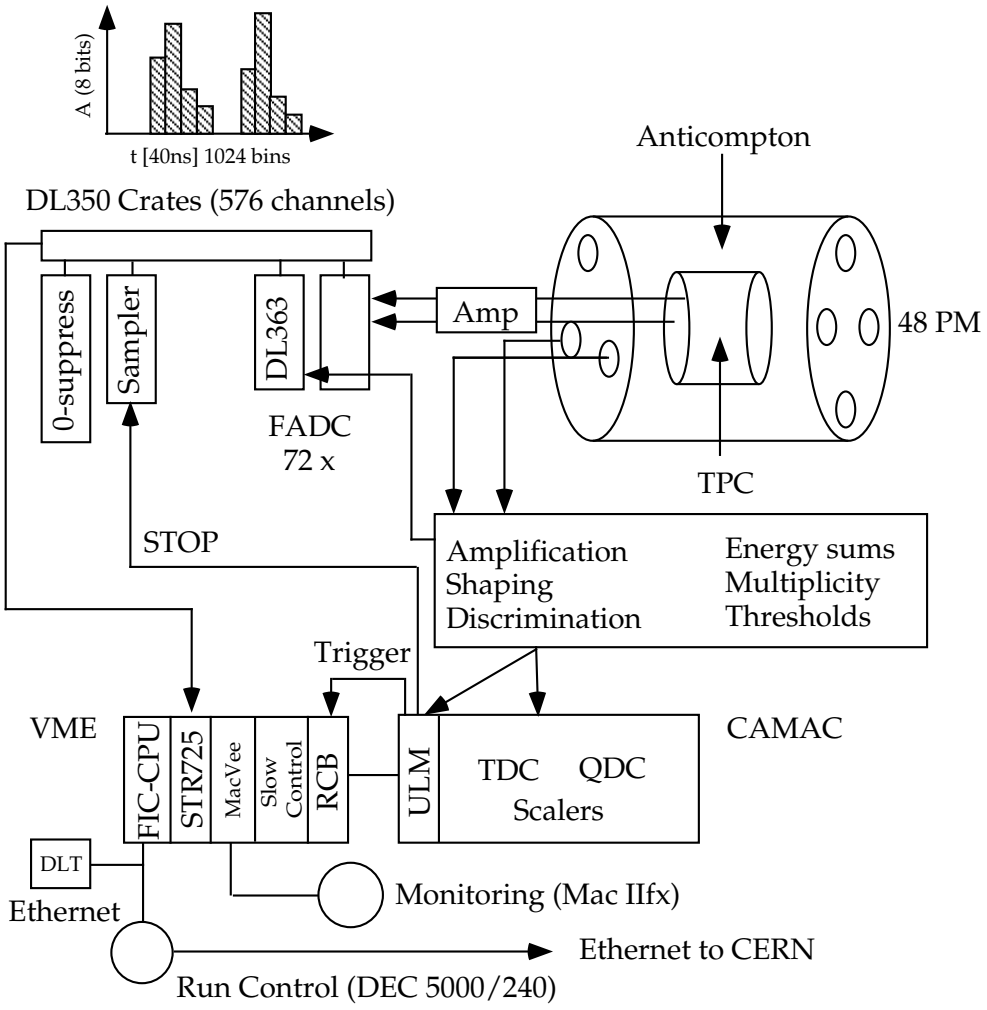

Figure 3.3: Electronics FADC readout and data acquisition system set up by the Zürich group. The photomultiplier readout was developed in collaboration with Grenoble.

Figure 3.1 shows a view of the TPC suspended in the liquid scintillator vessel. The TPC gas is enclosed in an acrylic container (Fig. 3.2). A field of 80 kV is applied between the cathode on one end of the container and the grid plane on the other end. Field shaping rings wrapped on the external circumference of the acrylic vessel provide a uniform electric field.

The z coordinate along the detector axis is calculated from the drift time. The drift velocity is 4 cm/μs at 120 V cm^{-1} bar^{-1}. Anode wires are electrically connected and provide the total energy of the electron and the timing signal for the TPC. Signals induced on the xy plane provide the two transverse coordinates. The xy plane is made of mylar covered on both sides by orthogonal copper strips with a pitch of 3.5 mm. There are 256 x and 256 y strips.

The 512 channels of x and y strips are preamplified and read out by flash ADC's (Struck DL350 system, see Fig. 3.3). We are thus able to visualize the electron track in three dimensions. The FADC response can be chosen non-linear to provide a uniform resolution

even for small pulses. The pulses are sampled with 8 bits every 40 ns and stored in memories, 1024 locations deep, which thus cover the maximum drift time (40 μs) of the TPC. The data acquisition system is based on a FIC 8234 CPU running under the OS9 operating system.

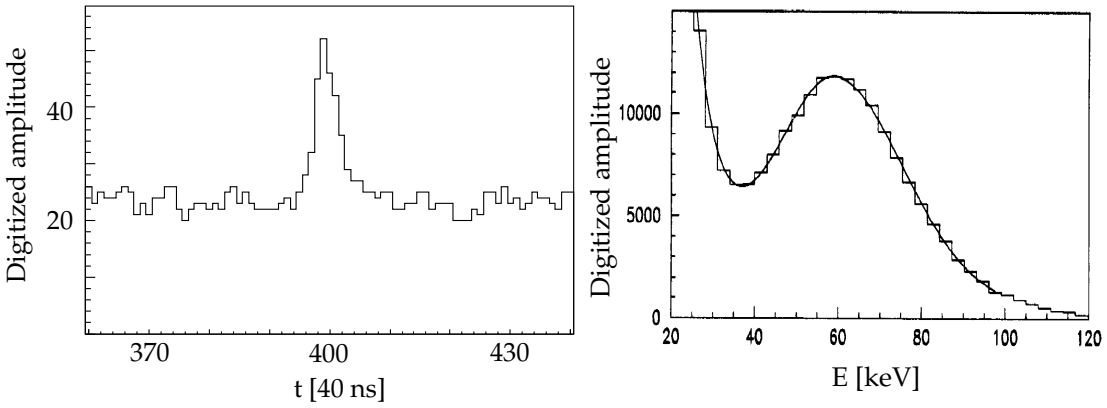

Figure 3.4: Left: amplitude distribution sampled by FADC from one photomultiplier for Čerenkov light induced by a passing muon. The signal is observed in coincidence with other photomutipliers. Right: measured energy distribution at 5 bar from the anode with 60 keV γ rays.

The Zürich group is responsible for the TPC readout and for the data acquisition system (Fig. 3.3) which is now fully implemented in the experimental area. Since several triggers (cosmic rays, neutrinos, radioactive sources, etc.) will be used, we are also preparing a general purpose trigger module (based on the LRS 2366 Universal Logic Unit, ULM) which will allow to adjust remotely the coincidences and timing for every trigger.

The FADC system is also used to read out the photomulipliers. The signals in the anti-compton shield generate on average less than one photoelectron in each of the photomultipliers for a veto threshold of 100 keV. The signals from several photomultipliers are therefore summed and shaped to a width of about 200 ns, larger than the sampling width (40 ns) of the FADC. Figure 3.4 shows the amplitude distribution from one photomultiplier from Čerenkov radiation induced by a cosmic muon traversing the acrylic vessel and detected in coincidence by at least 4 photomultipliers.

The full scale TPC has been operated in Neuchâtel at 3 bar with the FADC readout system using cosmic ray muons. Signals of the order of 10 mV were observed at 3 bar with an rms noise of less than 2 mV. The energy resolution was measured with 60 keV photons from an ^{241}Am source. Figure 3.4 shows the energy distribution of the anode signals. The resolution is $\sigma = 25$ % at 60 keV. Assuming that the resolution scales as the square root of the energy, we expect an energy resolution of $\sigma \simeq 10$ % at 500 keV.

A spatial resolution of $\sigma = 1.6$ mm has been achieved for the cathode strips by fitting muon tracks with straight lines. The mean attenuation length of drifting electrons at 3 bar was measured to be $22\ ^{+14}_{-6}$ m [4]. Figure 3.5 shows the projections $x - z$ and $y - z$ of an electron track initiated by a photon from a radioactive source.

With a small prototype of the TPC and a ^{112}Sn radioactive source we measured the angular resolution of electrons [5]. We obtained an angular resolution of $\sigma_{\theta_{space}} = 13°$ for 370 keV electrons, in agreement with simulation.

The detector is now fully installed under the reactor. Electric noise problems in the readout chain of the TPC are being investigated before we proceed with final calibration and data taking.

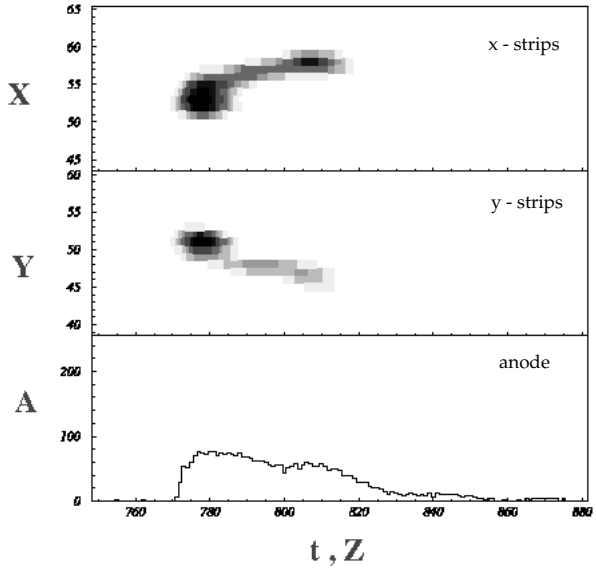

Figure 3.5: $x - z$ and $y - z$ views of a photon induced electron track, and time distribution of the anode pulse. Notice the larger ionization loss of the electron at the end of its trajectory (dark regions).

References

[1] E. K. Akhmedov *et al.*, Phys. Lett. **B 348** (1995) 124.

[2] F. Reines, H .S. Gurr and H.W. Sobel, Phys. Rev. Lett. **37** (1976) 315.

[3] P. Vogel and J. Engel, Phys. Rev. **D 39** (1989) 3378.

[4] C. Amsler *et al.*, Nucl. Instrum. Methods **A 396** (1997) 115.

[5] S. Iseli, diploma thesis, University of Zürich (1996).

4 Particle Physics at LHC/CMS

C. Amsler , M. Glättli, R. Kaufmann, F. Ould-Saada, P. Robmann, C. Regenfus,
S. Spanier, S. Steiner, P. Truöl and T. Walter
in collaboration with ETH-Zürich, Paul Scherrer Institut (PSI), Universität Basel
and the CMS collaboration.

In 1995 the Physik-Institut of the University of Zürich joined the CMS collaboration at the Large Hadron Collider. We participate (i) in the development and construction of the barrel silicon pixel detector (design of the pixels and readout chips and construction of the support structure and cooling system) and (ii) in the design and development of microstrip gas chambers (MSGC).

4.1 Pixel developments

The CMS pixel detector consists of two forward detectors and a barrel detector. The forward detectors are under the responsibility of the U.S. groups. According to the current layout [1] the barrel detector is made of three cylindrical layers, 53 cm long with radii of 4, 7 and 11 cm. The support structures are made of tubes with trapezoidal cross sections (providing water cooling) connected with carbon fibre blades and supported at both ends by carbon fibre end rings. Each layer is made of two half-cylinders to allow insertion into the CMS detector. Due to radiation damages close to the interaction point which limit the lifetime of the detectors, the two innermost layers will be used in the beginning during low luminosity run. The two outermost layers will be used during full luminosity runs and we anticipate that the 7 cm radius detector will have to be replaced after 5 years of LHC running.

A pixel cell contains 53 $\times$ 52 pixels of dimensions 150 $\times$ 150 μm^2. Two rows of 8 cells build a module and a row of 8 modules builds a facet of length 53 cm and width 1.75 cm. The total number of pixels to be read out are 6.3 $\times$ 10^6, 1.1 $\times$ 10^7 and 1.6 $\times$ 10^7, respectively.

Due to the deflection in the magnetic field which is parallel to the beam axis (z), the deposited charge in the wafer does not move to the closest pixel but drifts at an angle Θ_L, the Lorentz angle, towards the adjacent row. The charge deposit is therefore shared among several (mostly two) adjacent pixels. The averaged amplitude thus leads to an improved resolution in the $r\phi$ direction. In the z direction the charge is shared between up to 5 pixels, depending on the track polar angle. We anticipate a resolution of typically σ = 15 μm in both $r\phi$ and z directions.

With prototype detectors a depletion thickness of 150 - 200 μm has been achieved with 300 V bias voltage even after having irradiated the pixels with 6×10^{14} pions, a flux corresponding to the lifetime of the CMS experiment. The depletion thickness is larger than was expected in the experimental proposal and therefore the pixel size has now been increased from 125 $\times$ 125 μm^2 to 150 $\times$ 150 μm^2. This will still provide charge sharing among two adjacent pixels and the larger pixel size will also increase the space available on the readout chip under the pixel for the readout electronics. The total pixel thickness will be 250 μm.

Silicon has been chosen as substrate material. Gallium-arsenide and diamond were finally discarded, the former due to its poor radiation hardness and the latter due its insufficient charge collection length. We will use n-doped silicon because of the larger drift velocity of the electron charge carriers (and hence the larger Lorentz angle). Also, radiation damages will induce type inversion and the resulting p-layer will grow on the opposite side of the pixels.

Every pixel is connected to its own readout electronics on the readout chip through a pellet of indium (bump bonding). The readout contains a preamplifier, a shaper and a comparator driven by a DAC which sets the threshold. When a hit occurs in a column (2 pixel row),

the column and the time stamp is copied and stored into a column area. The readout occurs when the trigger verifies the time stamp. The pixel hit rate is typically 14 kHz in the 7 cm radius detector and the column multiplicity typically 2.

The Zürich group has prepared and performed tests of pixel detectors designed at PSI during two running periods at CERN. We used 300 μm thick detectors made of 256 pixels (125 $\times$ 125 μm^2) manufactured by CSEM (Neuchâtel). The first beam test was performed in 1995 at the CERN-SPS with 50 GeV pions to measure the position resolution [2]. Since no magnet was available for this test, data were taken at different detector inclination angles with respect to the beam axis to simulate the Lorentz angle in the magnetic field of CMS. An average signal to noise ratio of ~ 25 was achieved. We obtained a resolution $\sigma = 13$ μm for a tilt angle of 35° - which corresponds to the Lorentz angle in the CMS magnetic field of 4 T - in accord with forecasts from the experimental proposal [3].

The second beam test was performed in 1996 in a strong magnetic field with 225 GeV/c pions [4]. The Lorentz angle was determined by measuring the cluster size as a function of tilt angle. We obtained $\Theta_L = (15.5 \pm 2.4)°$ at 2 T, in good agreement with expectations (18.6°) from the known electron mobility in silicon. Details and results can be found in ref. [2, 4] and in last year's annual report.

For these first attempts the data collection efficiency was rather poor due to the large beam spot compared to the detector size. A good definition of the incident π tracks (e.g. with silicon microstrip detectors) was also not possible due to heavy multiple scattering from other detectors tested simultaneously in the same beam. An algorithm was used instead to measure indirectly the average spatial resolution without tracking, employing charge sharing between pixels [2, 4].

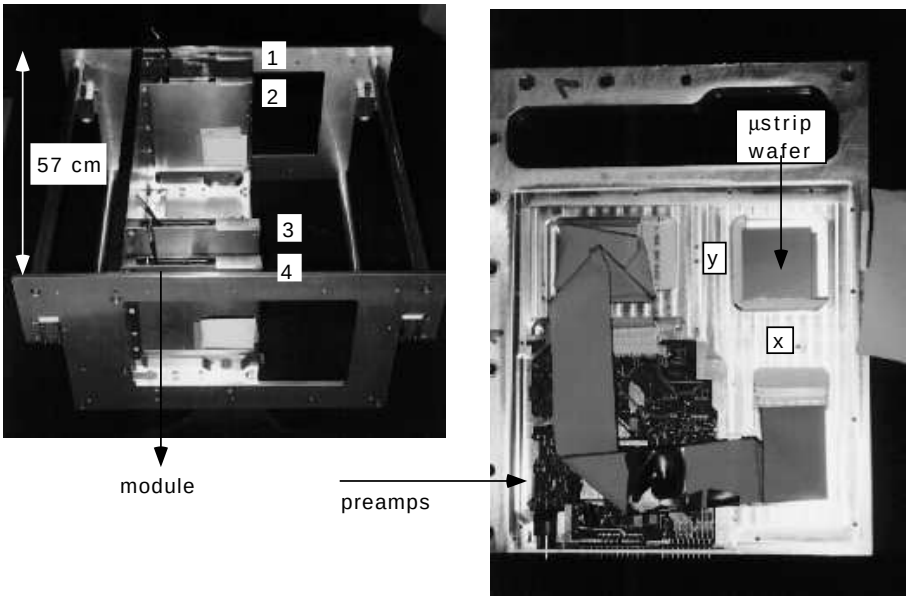

Figure 4.1: Left: telescope assembly showing the 4 $x - y$ microstrip modules; right: module with associated preamplifiers.

To alleviate the difficulties with multiple scattering from other detectors in the test beam and to perform a direct measurement of the position resolution of pixel (and later MSGC) devices we have built in the mechanical workshop of our institute a precision beam defining telescope (under the supervision of K. Bösiger). The telescope (Fig. 4.1) is made of four modules, each containing two 32 $\times$ 32 mm^2 single-sided microstrip silicon wafers, one provid-

ing the x-coordinates and the other the y-coordinates. The space between the two upstream and the two downstream modules is used for the pixel test device which will be sandwiched between two triggering diodes and mounted on a remotely controlled rotating support. The microstrip wafers were bonded at CERN.

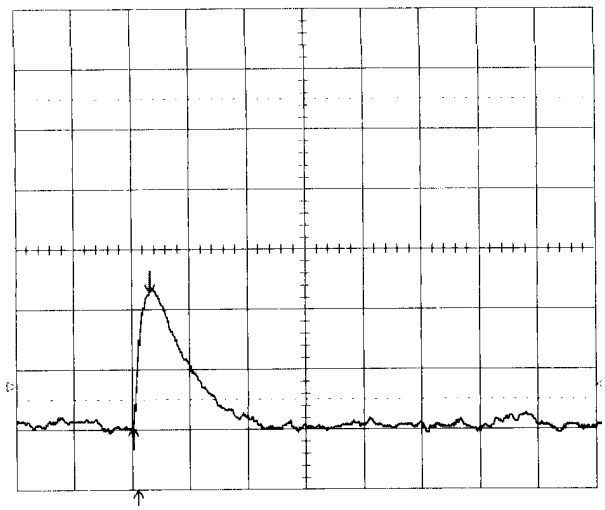

Figure 4.2: Preamplified signal from a 20 keV γ-source; horizontal scale: 5 μs/div.; vertical scale: 50 mV/div.

A microstrip wafer is 300 μm thick and contains 1280 strips with a pitch of 25 μm. However, only every second strip is connected to the readout electronics and the charge collected by the floating strips induces a charge on the readout strips by capacitive coupling. The signals from the 640 active strips are amplified, shaped and the total charge is stored (5 VA2 Viking chips each with 128 channels). Figure 4.2 shows the analog output signal from one of the preamplifiers, using a 20 keV γ-ray source.

A 2 MHz multiplexer reads sequentially the charge deposits which are then digitized by a Flash ADC (CAEN VME V550, 2 inputs for 2040 channels). The readout and data acquisition system are controlled by a VME FIC 8234 processor running on OS9. Data are written to disk or to DLT. We have developed this system for the data acquisition of our neutrino experiment at the Bugey reactor.

The telescope was tested in 1997 in a 100 GeV muon beam. The trigger signal was provided by the coincidence between two photodiodes. Seven out of the eight wafers worked satisfactorily with similar performances, while one of them had to be exchanged. Figure 4.3a shows the typical Landau distribution for the energy deposit of about 16'000 muons traversing one of the wafers. The detectors were fully depleted with a bias voltage of 45 V. A signal to noise ratio of 250 for minimum ionizing particles was achieved.

The typical cluster size was two strips per incident muon. The hit coordinates were determined accurately by using the energy deposit shared among the strips. The mechanical alignment accuracy of the detectors was typically 50 μm. A more accurate alignment was achieved by software with a large number of passing muons. We then determined the position resolution of each detector by fitting straight tracks and comparing the hit coordinates y with the predicted coordinate y(fit) from the fit. The distribution of residuals is shown in Fig. 4.3b for one of the detectors. A resolution of $\sigma \simeq 2.5$ μm was obtained for all eight detectors.

This kind of resolution represents the current state of the art in microstrip technology. It is more than sufficient for measuring the position resolution of pixel detectors. However, in the high rate environment of LHC, radiation damage will slowly reduce the depletion thickness of our pixel detectors. In spring 1998 we will therefore determine how the depletion thickness varies with radiation damage. Irradiated pixels at PSI will be submitted to a high

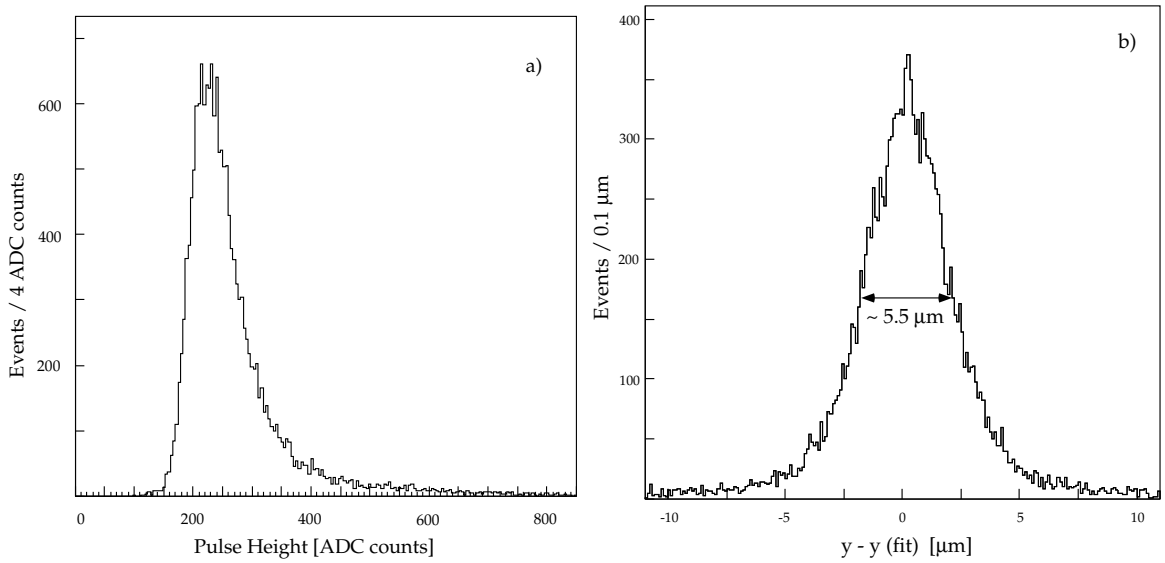

Figure 4.3: a): Distribution of the energy deposit for minimum ionizing particles in one of the microstrip detectors; b): Distribution of the residuals (differences between measured hit coordinates and expected coordinates).

energy beam at CERN. The beam will traverse the pixel detectors at grazing angles (i.e. nearly parallel to the depletion layer). The pixel cluster size, which depends on the incident angle and on the depletion thickness, will be measured. This obviously requires an accurate determination of the incident tracks which will be achieved with our telescope. At the same time we will repeat our measurement of the Lorentz angle in a strong magnetic field.

4.2 Microstrip gas chambers

The research and development effort in the area of microstrip gas chambers (MSGC), which are able to sustain high rates, still continues in many institutes within and outside of the CMS collaboration [5]. Though impressive progress has been made the final solution for the type of chamber which is going to be used has not been found, and hence the final plan for our contributions to CMS MSGC construction has not been agreed upon. Presently we are still concentrating on the chambers, which are going to be used for the inner tracking system of the HERA-B detector. Here also large fluxes of up to 10^4 cm^{-2}s^{-1} at small radii near the beam pipe demand a very high granularity, lead to a design not too different from what is planned for CMS and hence these MSCG's may serve as a realistic large scale prototype. Our partners within the HERA-B collaboration since 1995 are groups from the Universities of Heidelberg (Profs. F. Eisele, U. Straumann) and Siegen (Prof. G. Zech).

At the University of Zürich we are responsible for the design of the masks, the supervision of the production and the quality control of the substrates for all modules, the support of the complete modules within the magnet, and for the pion beam tests at PSI. It is these areas, where our work concentrated last year.

Several new masks have been laid out in Zürich in two standard sizes, 12.7×12.7 cm^2 and 30×30 cm^2, with 10 μm anode width, 170 μm cathode width and pitch 300 μm, with 305 and 767 anodes, respectively. From these masks chamber planes have been produced at IMT (Greifensee) on diamond coated AF45 glass substrates (ion conducting, surface resistivity $> 10^{16}$ Ω/square; after coating by chemical vapour deposition, 8×10^{14} Ω/square). The full

Figure 4.4: Photograph of the electrical MSGC anode break tester, designed by and built at the University of Zürich, during testing of the first larger series of HERA-B substrates at IMT (Greifensee). The cover, which contains the electronics board and anode contacts, is open. When it is closed and locked, contact is being made. The whole installation is within a clean box.

size prototypes (masks UZHHERA3 to UZHHERA5) belong to the largest MSGC's ever built. The different versions of the same size essentially differ in the distribution of high voltage feeds and reference points, but not in pitch and electrode width. Because of their large size new special tools were required and produced in our workshops. These tools were needed to handle the large substrates in the production process at IMT, and also for the transport of the finally more than 200 substrates to and from the Frauenhofer-Institut (Braunschweig), where the coating is done, IMT (Greifensee), and the University laboratories.

The quality control of large numbers of chambers is quite time consuming, if it is done solely under our microscope, even though the latter is equipped with computer controlled positioning, as shown in last years annual report. Substrates with too many anode breaks can be eliminated quicker using an electrical method which we have developed. The principle of the method was described in a diploma thesis [6], but it has been modified since then. Instead of capacitively coupling radio frequency signals to all anodes and using the height of the pickup signal as an indication for a fault, we are now contacting all the cathodes at one end and the anodes at the other end of the plate. A DC voltage (400 V) is then applied across the gap and the current of each anode measured separately. The new setup is shown in Figure 4.4, the measuring scheme in Figure 4.5, and the result of a measurement for a chamber plate in Figure 4.6. Compared to the prototype the system has also been mechanically improved to faciliate the positioning of the substrates and to guarantee reproducible contacts without damage to the electrodes, and now allows measurement of the surface resistance.

While the chamber tests in Heidelberg and Siegen with sources and X-ray tubes indicated

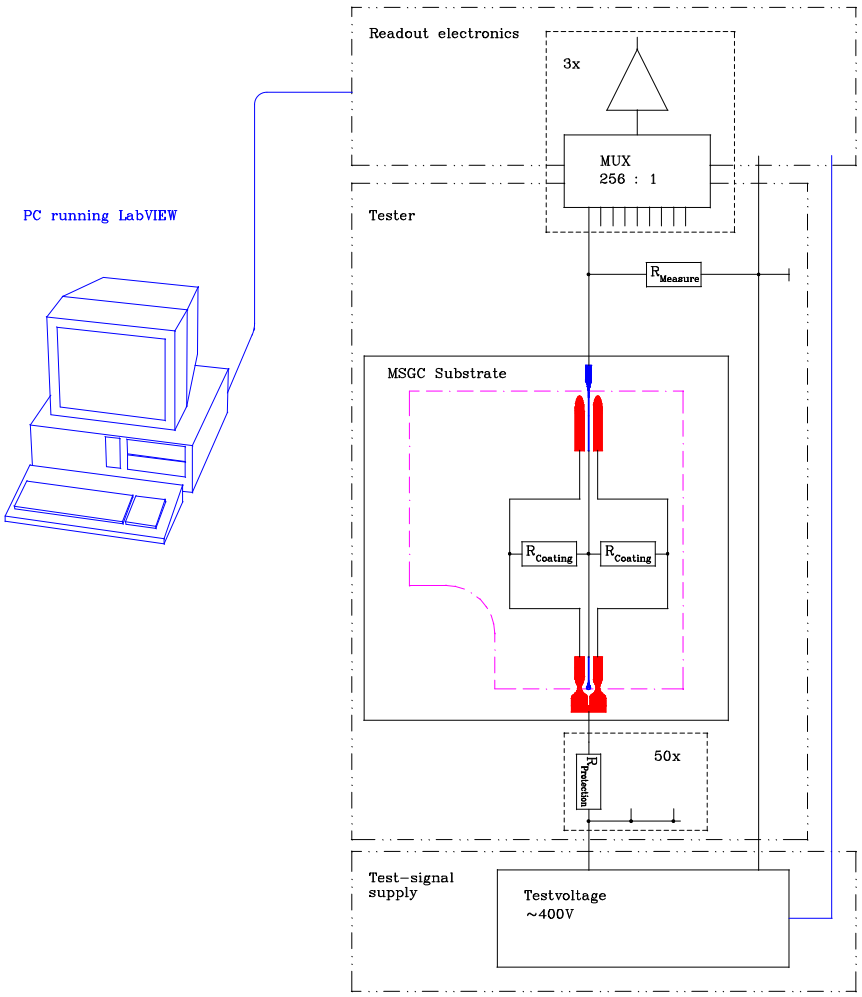

Figure 4.5: Measuring principle of the electrical MSGC anode break tester. The current over the anode to cathode gap is measured by recording the voltage drop across a control resistor with a computer controlled ADC.

satisfactory operation at gain factors around 3000 despite the sometimes microscopically poor quality of the anode borders [7], it was discovered during a PSI test in 1996, that chamber breakdowns occured at an intolerably high rate. As reported last year visual inspection of the chamber after the test indicated a close correlation of the number of anode defects and holes in cathodes with the number of sparks, most noteably for the gold plated anode, where often large pieces were found missing. This phenomenon was further investigated and confirmed in the laboratory (see the summary given by B. Schmidt [8]). Different remedies for this problem were proposed and studied by us and other groups. Only the gas electron multiplier (GEM) technique [9] showed promising features. In the GEM technique a thin mesh made from a double sided metal clad polymer is added in front of the microstrip plate (see Figure 4.7). The mesh has conical holes of 50 (or 80) μm diameter with a 140 (or 200) μm pitch (see Figure 4.8). A moderate voltage difference ($\approx$ 500 V) across the mesh produces an electrical field, that renders the mesh fully transparent and multiplies the number of electrons typically by a factor of 20, which in turn allows to operate the subsequent MSGC at lower gain and in a safer mode. Figure 4.8 shows measurements of the gas gain with and without the GEM foil.

A MSGC modified with a GEM foil was tested in Heidelberg at the tenfold HERA-B rate with X-rays and alpha particles without observation of sparks, because the cathode voltage can be reduced by 150 V. This behavior was confirmed with intense exposure to X-rays and tests in the HERA-B beam. Electron beam tests showed, that the chambers can be operated

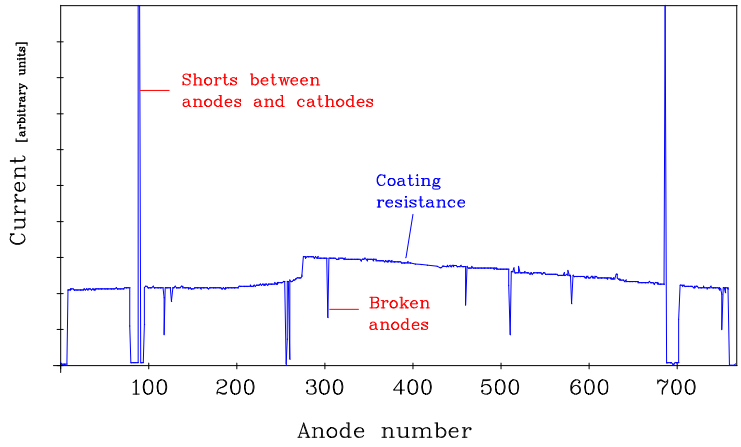

Figure 4.6: Result of a chamber plane test indicating shorts (2) and broken anodes (8). From the current measured for intact electrodes the surface resistance may be deduced.

in magnetic fields up to 0.85 T, and that the Lorentz angle of 7° (Ar/DME 50/50) only leads to a moderate increase in strip multiplicity [8]. A chamber with Au-electrodes was operated equivalent to a dose of one HERA-B year with Ar/CO_2 (70/30 %) with constant GEM and gas gain. Electrodes and GEM foil showed no damages after this exposure. No discharges induced by heavily ionizing particles were observed.

The production of large area GEM-foils has been started at CERN. To support stretched foils of up to 25 × 25 cm^2 the glas tube frame used so far for the MSGC prototypes has been replaced by a glasfibre reinforced plastic (GFK) frame of 10 mm width, closed by a Kapton cover. Twenty diamond coated glas substrates with Al electrodes, which are more robust against occasional breakdowns, are available for a preseries to be equipped with the CERN GEM foils. The number of anode breaks and shorts was found to be below the allowed tolerance, as revealed by our measurements (see e. g. Figure 4.6). For the frontend electronics the HELIX128 chip, which underwent several revisions, will be used, for the one complete station (eight detectors) to be installed in HERA-B this year.

References

[1] Technical Design Report of the CMS Tracker (1998).
[2] V. Dubacher, Diploma thesis, University of Zürich (1996).
[3] The Compact Muon Solenoid, Technical Proposal, CERN/LHCC/P1 (1994).
[4] R. Kaufmann, Diploma thesis, University of Zürich (1997).
[5] F. Sauli, 5^{th} Int. Conf. on Advanced Technology and Part. Phys., Como (1996), CERN-PPE/97-18; see also RD28 Status Report, CERN LHCC 96-18; E. Albert et al., CMS Note/1997 - 014; The Forward-Backward MSGC Milestone Report, O. Bouhali et al. (September 1997).
[6] Electrical method for detecting anode breaks on microstrip gas chamber substrates, A. Maag, Diploma Thesis, University of Zürich (1997).
[7] S. Visbeck, Diploma Thesis (1996); T. Hott, Thesis (1997); C. Bresch, Diploma Thesis (1997); all University of Heidelberg, see [10].
[8] B. Schmidt, Proc. 36. Workshop on the INFN Eloisatron Project on New Detectors, Erice (Sicily), November 1997; see [10].
[9] R. Bouclier et al., CERN preprints PPE/96-177; PPE/97-032; F. Sauli, Nucl. Instr. Meth. B (1997), in print.
[10] available at: http://www.physi.uni-heidelberg.de/groups/herab/MSGC_Info.html.

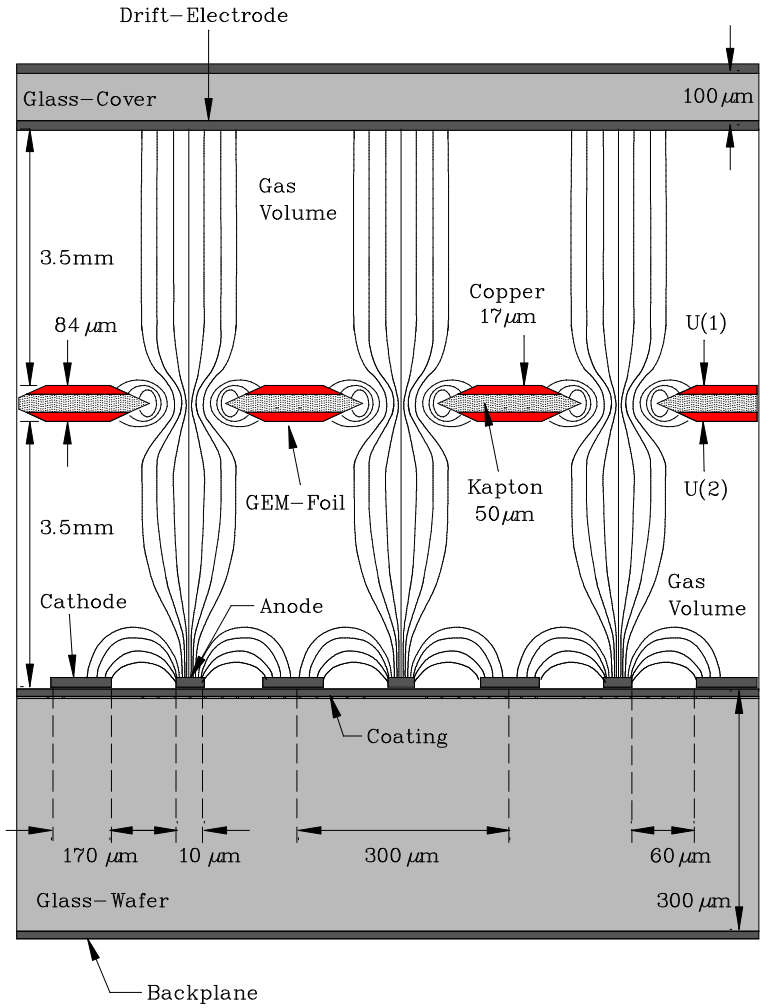

Figure 4.7: MSGC with an additional gas electron multiplier (GEM) foil.

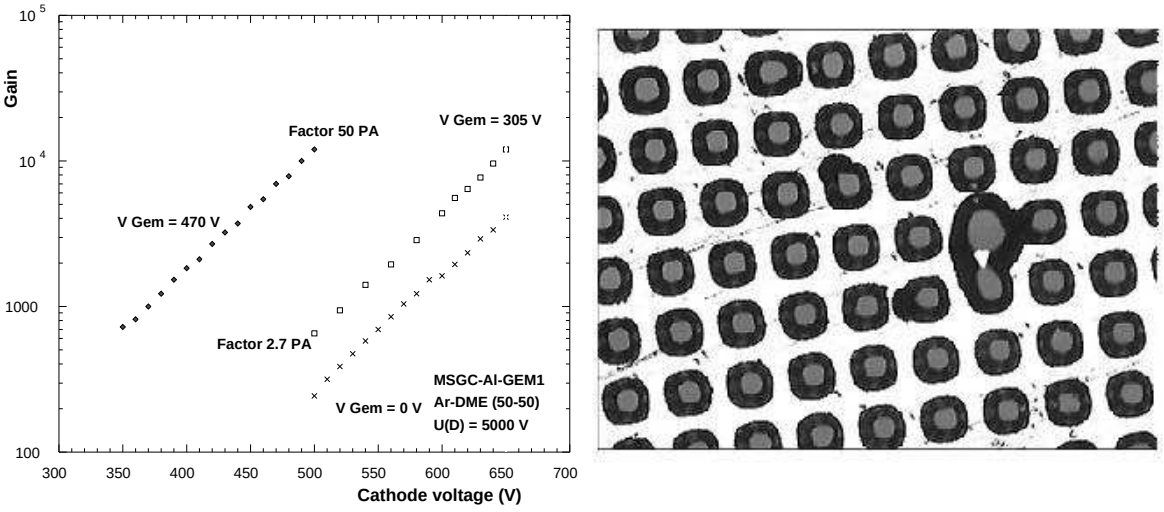

Figure 4.8: Left: gas gain in a GEM prototype compared to a standard MSGC. Right: a GEM foil with holes every 140 μm viewed under a microscope. The light area is the Cu surface, the dark shaded area is the insulating Kapton layer, the holes appear grey. This section of the foil shows a defect from the production process.

5 Particle Physics at DESY/HERA

S. Egli, S. Hengstmann, D. Müller, M. zur Nedden, P. Robmann, F. Sefkow,
P. Truöl, T. Walter,
in collaboration with
M. Biddulph, R. Eichler, J. Gassner, C. Grab, M. Hilgers, H.-C. Kästli,
S. Lüders, U. Langenegger, H. Niggli, S. Passagio, D. Pitzl, and Y. Tsipolitis,
Institut für Teilchenphysik der ETH, Zürich
K. Gabathuler, and R. Horisberger
Paul–Scherrer–Institut, Villigen,
and 34 institutes outside Switzerland
(**H1**–Collaboration)

5.1 Electron proton collisions at 300 GeV center of mass energy: overall status of the project

The operation of the HERA accelerator complex has been continously improved in reliability as well as in peak performance. This is demonstrated by the luminosity curves in Figure 5.1 and the data collected in Table 5.1. The 1997 run was particularly successful, and exceeded the scheduled goals by a factor of 1.4. Though the maximum proton and positron currents reached only 76 % and 69 %, respectively, of their design values so far, peak luminosities in H1 with 67 % of the design value (15 $(\mu\text{b s})^{-1}$) are found, because the beam dimensions (179×48 μm^2) are twice smaller than predicted. For the magnet cycling, preaccelerator preparation, storage ring filling and energy ramping of the positron and proton ring to 27.5 GeV and 820 GeV, respectively at least three hours are needed, which is why the running efficiency (luminosity delivery divided by total time) is limited to 80 %. Technical failures, repairs and deficit in controls however limited the running efficiency to 42 %, a value which is continuously increasing, in particular if no long shutdowns interupt the schedule. We are presently at the end of such a long shutdown, in which among other technical improvements the vacuum system of the electron/positron ring was upgraded in order to increase the electron beam life time. Luminosity operation is going to resume only in August 1998, with electron acceleration as well as higher proton beam energies (up to 920 GeV) are foreseen.

With a total luminosity of 45 pb^{-1} now accumulated, the H1- as well as its rival ZEUS-collaboration have continued to explore the structure of the proton and scrutinize quantum chromodynamics predictions. The principal areas covered by recent and ongoing analyses are

- neutral and charged electroweak current cross sections [1],
- proton structure functions and parton densities in new domains of Bjorken x and momentum transfer Q^2 [1, 2, 3, 4],
- search for states outside the standard model [5],
- photoproduction at high invariant masses of the photon proton system and parton densities in the photon [6, 7, 8, 9],
- diffractive processes and the structure of the pomeron [10, 11, 12],
- testing perturbative and non-perturbative quantum chromodynamics predictions with the evolution of structure functions [2, 4],
- parton-fragmentation into exclusive and multijet final states [13, 14, 15, 16], and
- production of heavy quark-antiquark states [17, 18, 19, 20].

Though the luminosity is still insufficient to accumulate yet large event samples for the most important electroweak processes at high momentum transfer ($Q^2 \approx M_W^2$), our first paper

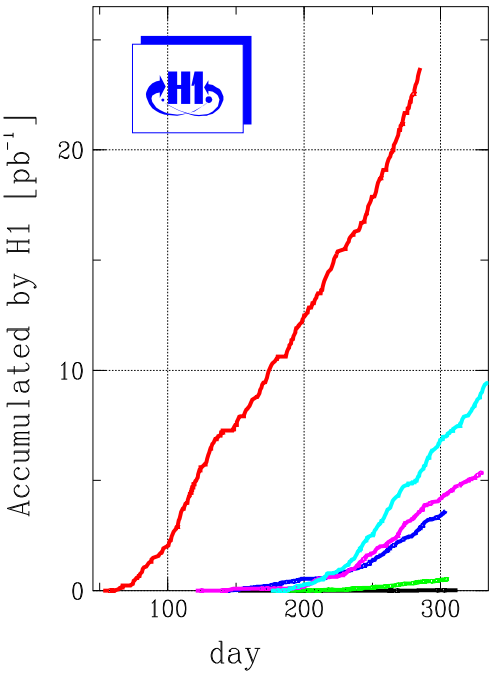

Figure 5.1: Integrated luminosity during the first six years of HERA operation, as seen by the H1-detector (lowest curve: 1992, highest curve: 1997).

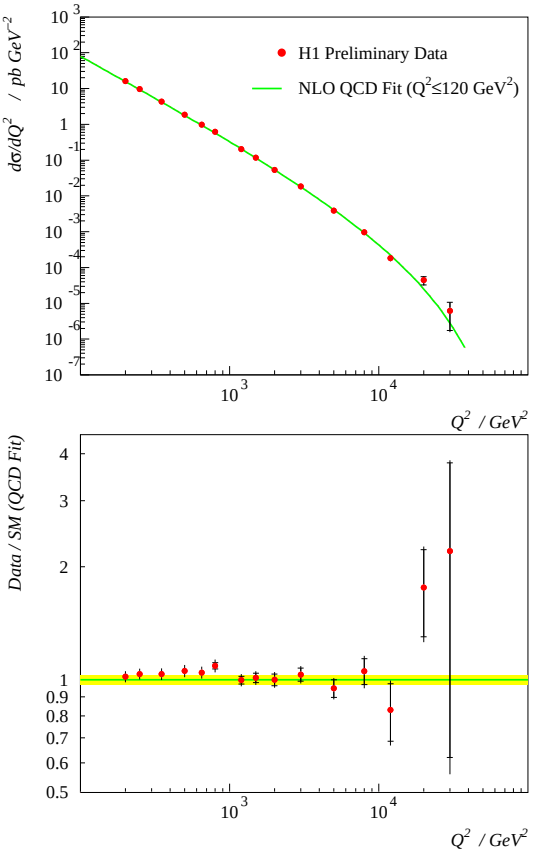

Figure 5.2: High-momentum transfer inclusive single differential cross section $d\sigma/dQ^2$ for deep inelastic positron proton scattering (top), and deviations of the data from the next-to-leading order QCD fit (bottom)

[1], which dealt with this region ($Q^2 > 15000$ GeV^2) led to a great deal of excitement, since the number of observed events exceeded that expected within the standard model description of deep inelastic lepton scattering. The data collected since then in 1997 do not show such an excess [3, 4], but at the highest accessible momentum transfers small differences still exist (see Figure 5.2 and Section 5.4.1).

To fully exploit the discovery potential of the HERA machine in the largely unexplored mass region near 200 GeV a luminosity upgrade is planned for the year 2000. Through a change of the beam focussing near the interaction region the luminosity will be increased by a factor of five. This is achieved by introducing new magnets within the H1 detector and requires modifications of its inner parts.

The activities of the University of Zürich group concern the maintenance, monitoring and continuous improving of the detector components built at Zürich for the central tracker and the first level trigger of H1, and participation in the physics analysis, in particular in the areas of photoproduction, charmed quark containing final states and deep inelastic scattering. As in the past we continued to be strongly involved in adapting the first level triggers to the increased beam currents and backgrounds at H1.

The construction of a new five-layer, central inner multiwire proportional chamber with finer granularity and increased redundancy will be a major contribution by the Zürich groups

Parameter	1992	1993	1994		1995	1996	1997
	e^-p	e^-p	e^-p	e^+p	e^+p	e^+p	e^+p
Integrated luminosity $\mathcal{L}$							
HERA produced [nb^{-1}]	–	999	938	5063	11437	14366	37574
HERA physics [nb^{-1}]	55	880	846	4743	10403	13299	35755
H1 taken [nb^{-1}]	30	568	532	3576	6414	8919	30434
H1 physics [nb^{-1}]	25	528	494	3489	5745	8648	26392
HERA efficiency [%]	–	88	90	94	91	92	95
H1 efficiency [%]	46	60	58	73	55	65	74
Average luminosity [(μb s)$^{-1}$]	0.03	0.27	0.62	1.29	2.13	2.64	4.38
Peak luminosity [(μb s)$^{-1}$]	0.22	1.3	2.6	4.3	5.9	8.4	10.1
Average p current [mA]	0.94	10.8	28.6	41.0	54.0	60.3	74.5
Average $e^{\pm}$ current [mA]	1.33	7.7	10.5	17.0	18.4	20.6	28.0
Colliding bunches	9	84	153	153	174	175	175
Pilot (e,p) bunches	1,1	10,6	15,17	15,17	15,6	14,6	14,6
HERA luminosity runs	132	218	116	176	304	241	411
Permanent H1 runs	1409	3190	1141	1816	4208	3582	5369
Average duration [s]	973	817	1115	1620	884	1159	1431

Table 5.1: Summary of HERA and H1 operation during the first six years.

to the upgrade of the H1-detector needed concurrent with the change of the interaction region.

5.2 Summary of activities related to the Zürich H1-components

During the shutdown 1997/8 the complete central and forward tracker was extracted from the H1 detector in order to rewire the central jet chamber, which showed degradation in the lower sectors. This gave us the opportunity to open both our central inner proportional chambers (CIP), measure the wire tensions (found unchanged) and search for radiation damage. Only in a small sector of one chamber, where full high voltage could no longer be reached, deposits were found. Five wires in this area were replaced and the chamber cleaned. Otherwise no radiation damage was apparent. The continuous monitoring of the chamber performance for the $z-$vertex trigger showed no degradation of the efficiency either. The central inner $z-$drift chamber (CIZ) was completely rewired, since radiation damage was observed in some of the fifteen rings, most prominently in those for which the wires were not replaced by new and especially cleaned ones previously. During 1997 the central silicon detector (CST) was fully operational. The fine tuning of the alignment parameters and the development of the reconstruction codes is nearly completed, with impact on the secondary vertex selection for the heavy quark analysis expected soon. During the shutdown 1997/8 a few ladders were exchanged and the adapter tube, a lightweight sandwich construction containing the CST power cables and cooling pipes and surrounding the backward silicon detector, was completely rebuilt.

While the vertex detector is important for the reconstruction of events containing charm quarks, the $z-$vertex and drift chamber track triggers built and serviced by us and our ETH-colleagues are essential for triggering these events, which are characterized by low transverse energy. Since both Zürich groups also participate strongly in the analysis of these events, they also played a central role in their collection, i. e. in the careful reoptimisation of the trigger set-up for the 97 data taking, using feedback from our own ongoing analyses. These

tasks include the responsibility for the verification of the whole on- and off-line selection chain for open charm.

In this respect we have also investigated [21] trigger possibilities with signals from the central inner MWPC (CIP) alone. The study was motivated, on one hand, by the ever increasing demands on background rejection, which relies heavily on the existing $z-$vertex trigger and will continue to do so until the full commissioning of the system envisaged for the HERA luminosity upgrade. On the other hand, using real data samples – beam gas background events, charm and jet photoproduction physics events –, allowed us to study, without having to make assumptions on simulated background, the performance of a thin MWPC system, i. e. one without the lever arm provided by the combination with the outer MWPC. In this respect we considered a trigger logic similar to that of the proposed upgrade. The results support the proposal for the CIP and vertex trigger envisaged with the HERA high luminosity upgrade (see Section 5.3 below). We found that already with the present chamber, a careful analysis of the backward part allows to recognize upstream tracks and to achieve a substantially improved background rejection while keeping physics inefficiencies at the percent level. With a relatively simple hardware modification such a logic can be implemented. For the proposed CIP upgrade, with a finer $z-$segmentation and five radial layers, a much better track angle resolution and thus much more powerful background discrimination can be expected.

In the analysis we concentrated on the following aspects: calibration and efficiency monitoring of CIZ and CIP, monitoring the performance of the $z-$vertex and big ray trigger elements, optimization of the trigger settings for charm events, optimizing D^*-tagging codes and determining the charm photoproduction and deep inelastic electroproduction cross section, deriving the gluon distribution in the proton from these data (see Section 5.4.2 below), and investigating high p_T charged particle photoproduction and its relation to the photon structure functions.

5.3 Upgrade plans

In order to achieve higher luminosities and higher event rates for the rare processes at the limits of the kinematically accessible range it is planned to upgrade the HERA machine complex [22]. The most important aspect of this program is the improvement of the focussing properties near the interaction region, which calls for a new lattice with machine magnets inside the detectors and new types of septum magnets. The consequent beam squeeze will allow for a luminosity $\mathcal{L} = 7.4 \times 10^{31}$ cm^{-2}s^{-1}, a factor of seven compared to what is presently achieved (see Table 5.1).

Unfortunately this scheme will generate synchrotron radiation inside H1, it can no longer be stopped before the experiment as in the present setup. This has a big impact on the beam pipe and absorber design, and will also require rearranging the central (CST) and backward (BST) silicon trackers. For the CST the same silicon ladders will be used, but new end flanges and support are needed.

As part of the upgrade project we proposed to replace the CIZ and the CIP with a five plane cylindrical proportional chamber [23]. This proposal was primarily motivated by the demand for higher redundancy and safer operation in a higher level of synchrotron radiation background, the need to resolve CST ambiguities and the desire to have a robust determination of the interaction vertex with a tracker element at high initial rates. The new CIP can make a sufficiently accurate determination of the vertex position and the event timing and help us keeping, in combination with the calorimeter, the high Q^2 events at initial top luminosities of a new fill, when other trackers can not be turned on yet. The new chamber

will also be used for an improvement of the z-vertex trigger. A drawing of the new five layer proportional chamber with a pad width of 9 mm in sixteen $\phi-$sectors is shown in Figure 5.3.

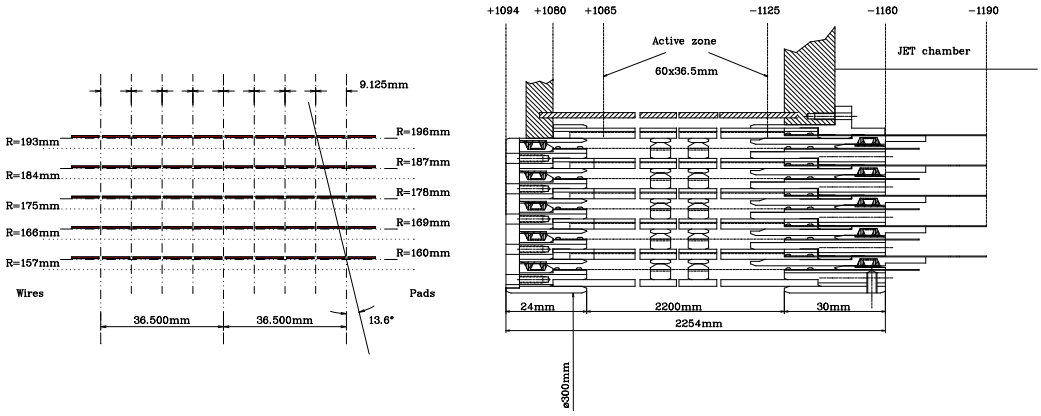

Figure 5.3: Cross section of the planned new central inner proportional chamber (right). Left: cathode pad structure (36.5 mm width in the present CIP).

5.4 Results from recent analyses

5.4.1 Deep inelastic scattering at highest momentum transfer and the standard model

The differential cross section for deep inelastic positron proton scattering may be written in terms of the two independent kinematical variables x and Q^2 as

$$\frac{d^2\sigma}{dx\,dQ^2} = \frac{2\pi\alpha^2}{xQ^4}\left[Y_+F_2(x,Q^2) - y^2F_L(x,Q^2) - Y_-xF_3(x,Q^2)\right] \ .$$

$Q^2(\equiv -t)$ is the squared four-momentum transfer of the scattered positron and x the fraction of the proton momentum carried by the struck quark. The variable y is defined as $y = Q^2/xs$, with s being the total positron-proton center of mass energy (300 GeV), and $Y_\pm(y)$ is defined as $Y_\pm = 1 \pm (1-y)^2$. F_2 and F_L are the generalized and the longitudinal structure function, respectively, F_3 is the parity violating term arising from Z_0 exchange. F_2 may be decomposed into three terms

$$F_2 = F_2^{em} + \frac{Q^2}{Q^2+M_Z^2}F_2^{int} + \frac{Q^4}{(Q^2+M_Z^2)^2}F_2^{weak} \equiv F_2^{em}(1+\delta_Z)$$

F_2^{em} contains only photon exchange, F_2^{weak} only Z_0 exchange, and F_2^{int} the interference of both contributions. For convenience often the reduced cross section is used

$$\sigma(e^+p) \equiv \frac{xQ^4}{2\pi\alpha^2}\frac{1}{Y_+}\frac{d^2\sigma}{dx\,dQ^2} = F_2^{em}(1+\delta_Z-\delta_3-\delta_L) \ .$$

For the correction terms one finds $\delta_Z - \delta_3 < 1\%$ at $Q^2 < 1500$ GeV^2 and $\delta_Z - \delta_3 \approx 10\%$ at $Q^2 = 5000$ GeV^2 and $x = 0.08$, while δ_L is negligible at $y < 0.5$ and $\approx 5\%$ at $y = 0.9$. F_2 in turn is given by the sum of quark, antiquark and gluon densities.

Since both the positron and the final state hadrons marking the path of the struck quark are observed in the detector the kinematical variables can be reconstructed from angle and

energy of either positron or hadronic jet or a combination of both. For example in terms of positron quantities one finds

$$y_e = 1 - \frac{E_e(1-\cos\theta_e)}{2E_e^0} \ , \quad Q_e^2 = \frac{E_{T,e}^2}{1-y_e} \ , \quad M_e = \sqrt{sx_e} = \sqrt{\frac{Q_e^2}{y_e}} \ .$$

M_e is the mass of the positron-quark system, $E_{T,e}$ the transverse energy of the positron, $E_e^0 = 27.5$ GeV and θ_e, the polar scattering angle measured from the proton direction. The H1-detector has good positron energy resolution, as evidenced by the calibration data displayed in Figure 5.4, which favors use of positron variables in particular at high momentum transfers, but important and quite accurate cross checks using the jet quantities are possible. These are important for charged current processes mediated by W exchange, where the kinematical quantities can only be deduced from the final state hadrons.

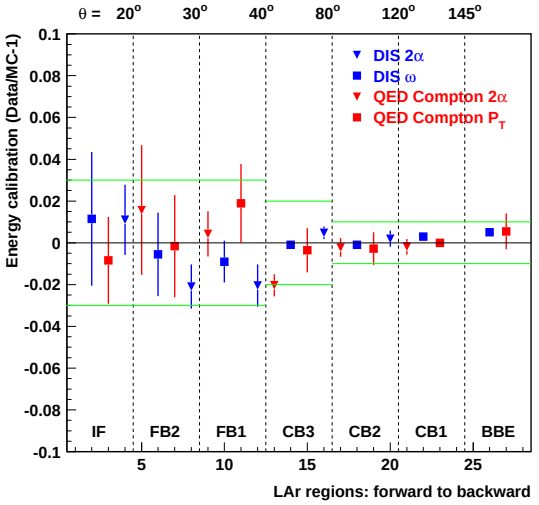

Figure 5.4: Present status of the liquid Argon electromagnetic calorimeter calibration. The data points are from reactions, where the electron or positron energy can be calculated from other kinematical quantities.

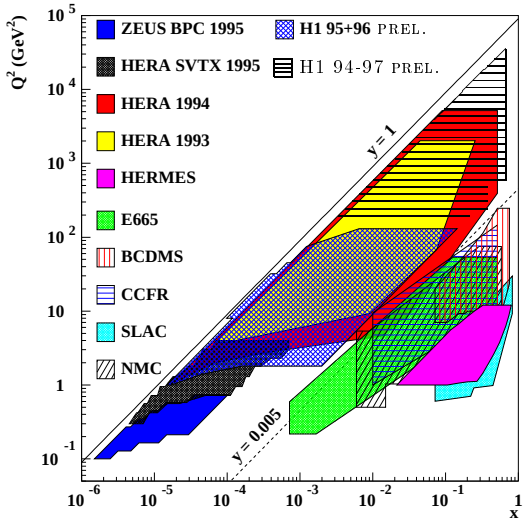

Figure 5.5: Regions covered by different experiments in the $(x, Q^2)-$plane. Entries with labels other than HERA, H1, or ZEUS are from fixed target experiments.

The high ep center of mass energy has meant that proton structure has been probed for the first time not only at high Q^2 but also at very low Bjorken x. In this kinematic region of low parton momenta the gluon density was found to be rising steeply (see e. g. [2]). Better understanding of all detector components, including the new components from the first upgrade in the analysis, has allowed to considerably extend the kinematical range (see Figure 5.5), also in the direction of high x where the gap to the lower Q^2 fixed target experiments could be bridged.

Displaying the integrated cross section $d\sigma/dQ^2$ as a function of Q^2, as done in Figure 5.2, is the most direct way to expose possible fermion substructure. Standard model predictions describe the data very well over seven orders of magnitude in cross section, nearly independent of how the parton densities are extrapolated from the low Q^2 data. Limits on fermion substructure can be set e. g. assuming a classical charge form factor

$$\frac{d\sigma}{dQ^2} = \left(\frac{d\sigma}{dQ^2}\right)_{SM} f_e(Q^2) f_q(Q^2) \quad \text{with} \quad f_{e/q} = 1 - \frac{1}{6} R_{e/q}^2 Q^2 \ .$$

Since $(g-2)$ and (e^+, e^-) experiments already put stringent limits on the electron radius R_e the HERA data are sensitive to quark radii $R_q < 10^{-18}$ m.

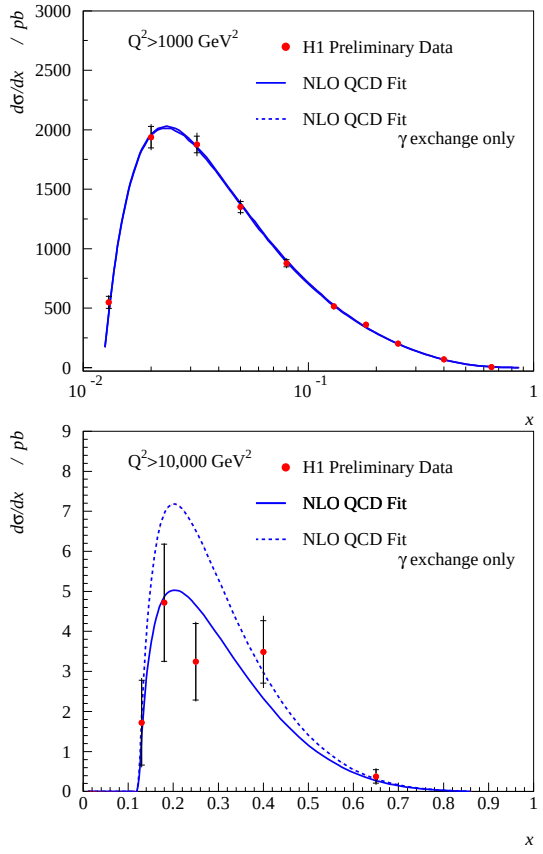

Figure 5.6: Differential cross section as function of x for $Q^2 > 1000$ GeV^2 and $Q^2 > 10000$ GeV^2 indicating the influence of the electroweak neutral current mediated by Z_0 exchange.

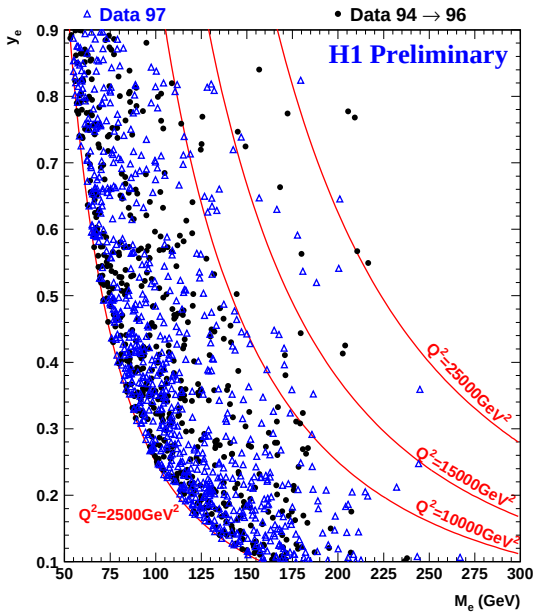

Figure 5.7: Distribution of events in the $(x, Q^2)-$plane. Filled circles: up to 1996 data (14.2 pb^{-1}), triangles: 1997 data (22.8 pb^{-1}). For $Q^2 > 5000$ GeV^2 322 events are observed, whereas 336±30 are expected, while for$Q^2 > 15000$ GeV^2 22 are found and 15±2 are expected.

Integrating the cross section over Q^2 above a certain high Q^2_{min} (see Figure 5.6) exhibits that one has to go to $Q^2_{min} = 10000$ GeV^2 to observe the influence of the valence quarks and of the Z_0 contributions, for $Q^2_{min} = 1000$ GeV^2 the cross section is still dominated by low x partons.

The small excess of events observed at the highest Q^2 (see Figure 5.2) was already present in the pre-1997 data sample comprising an integrated luminosity of 14.2 pb^{-1} [1]. Above $Q^2 = 5000$ GeV^2 144 events where found, while the the expectation from the standard neutral current deep inelatic scattering model was 136 ± 12, while above $Q^2 = 15000$ GeV^2 12 where found and 4.7 ± 0.8 expected, with a preference for a mass window of total width 25 GeV centered at an invariant mass $M_e \simeq 200$ GeV of the positron-parton system. Figure 5.7 shows the kinematical distribution of high Q^2 events in the (y, M_e) plane including the new events found in 1997 [3, 4]. The accumulated luminosity now is 37.0 pb^{-1}. The concentration of events in a given mass region is no longer observed, and the event count now yields for $Q^2 \geq 5000$ GeV^2 322 events (336 ± 30 expected) and for $Q^2 \geq 15000$ GeV^2 22 (15 ± 2). Thus the significance for the anomaly decreased last year. The corresponding charged current data ($ep \to \bar{\nu_e} X$) shown in Figure 5.9 lead to similar albeit statistically less significant conclusions.

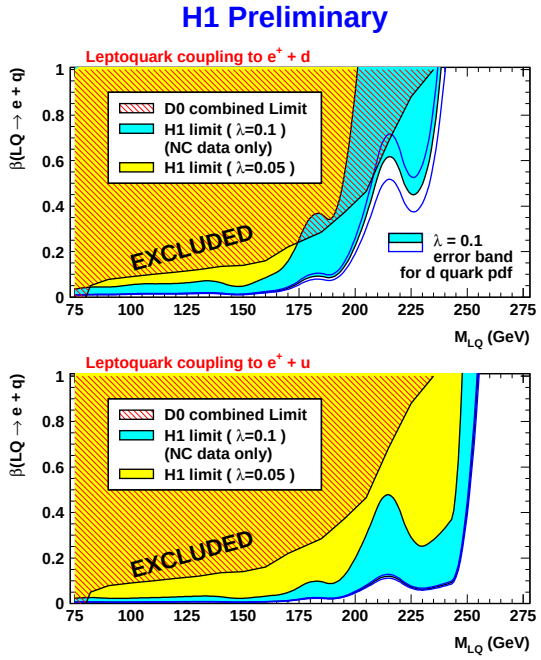

Figure 5.8: Limits for the branching ratio of a leptoquark decaying into a positron and a quark, assuming fixed values of the coupling constant λ versus the leptoquark mass (see [4]).

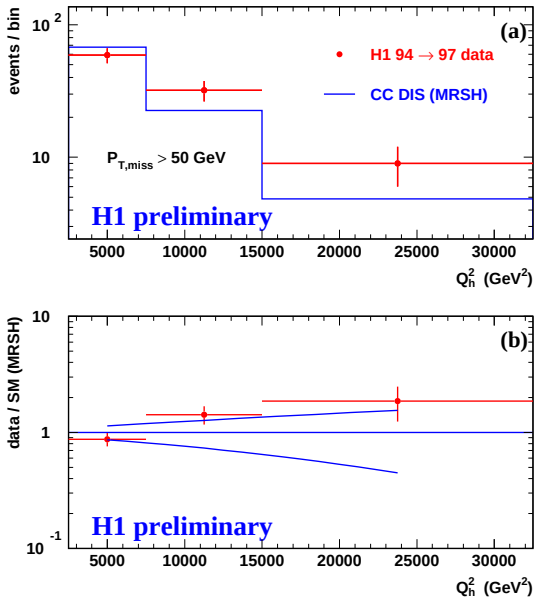

Figure 5.9: High Q^2 charged current data. The expected number of events (histogram) is compared to the number of events found. For $Q^2 > 2500$ (7500) [15000] 100 (41) [9] events are found, while 95 ± 17 (28 ± 8) [5 ± 3] are expected (see [3] for details).

The data have also been analysed in order to limit the couplings and masses of hypothetical leptoquarks, postulated to exist in some extensions of the standard model. Competition in this area comes mainly from Fermilab-Tevatron experiments (e. g. $D0$).

Already in 1994 an event with unusual characteristics ($e^+p \rightarrow \mu^+X$) was observed in our detector. This event was found in the standard charged current analysis, showed an isolated high momentum muon recoiling against a system of hadrons and was unbalanced in momentum suggesting the presence of an undetected final state particle. This observation initiated a search for high energy isolated leptons in events which are unbalanced in transverse momentum in all the available data until now [5]. Five such events, four of them with isolated muons, one with an electron, were found within the about 500 charged current candidates with a missing transverse momentum exceeding 25 GeV. Only two of these events fit into a region of phase space, which is likely to be populated by W production followed by a leptonic decay of the W:

$$e^+p \rightarrow e^+W^\pm X, \;\; W^\pm \rightarrow e^\pm\nu_e(\overline{\nu}_e), \;\; W^\pm \rightarrow \mu^\pm\nu_\mu(\overline{\nu}_\mu)$$

In only one of these events (shown in Figure 5.10) also the scattered positron is observed, which allows to calculate the invariant mass of the (μ, ν) pair to $M_{\mu\nu} = 83^{+15}_{-10}$ GeV, i. e. consistent with M_W. Since W's are mainly photoproduced with a radiation of a W from the quark line and a total cross section of 70 fb per channel and charge, the other three events all lie at the edge of the phase space, are very unlikely to result from this process, and hence yet unexplained.

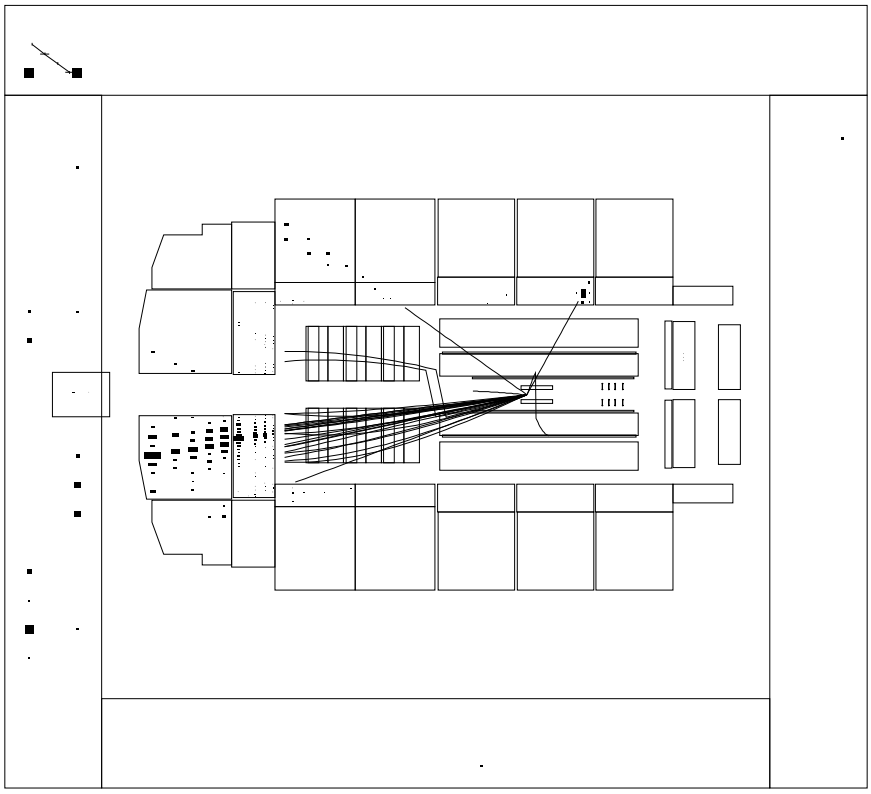

Figure 5.10: One of the six events observed with an isolated e^- oder $\mu^\pm$ of high transverse momentum in the e^+p sample with an imbalance in transverse momentum. This event is consistent with the hypothesis $e^+p \to e^+W^-X$; $W^- \to \mu^-\bar{\nu}$. Upper left track: μ^-, upper right track: e^+, lower left tracks: hadronic jet [5].

5.4.2 Photo- and electroproduction of charm quarks

Heavy flavours in the hadronic final state, like jets, carry a lot of information about the dynamics of the unobservable quarks and gluons. They thus provide access to the underlying hard partonic processes of high energy ep interactions. The aim is to test the description of the production processes by perturbative QCD, and to extract information on the parton distributions of the initial state hadron. In the conventional picture of ep scattering, charm is produced almost exclusively via boson gluon fusion and thus directly probes the gluon content of the proton.

Open charm at HERA has mainly been reconstructed in the fragmentation and decay chain $c \to D^{*+} \to D^0\pi^+ \to (K^-\pi^+)\pi^+$ exploiting the clean experimental signal in the mass difference distribution of $\Delta m = m(K^-\pi^+\pi^+) - m(K^-\pi^+)$ (and similar for the charge conjugate).

It is possible to make use of the kinematic information from the reconstructed charm tag, in order to reconstruct the momentum fraction x_g of the incoming gluon and thus arrive at a direct measurement of the density function $g(x_g)$. We have shown a first measurement [20] of the differential charm cross section as a function of x_g^{OBS}, which was reconstructed from the D^* meson and the scattered positron (Figure 5.11). The analysis of the three times larger 1996 sample is underway. QCD predictions in next-to-leading order (NLO) for such

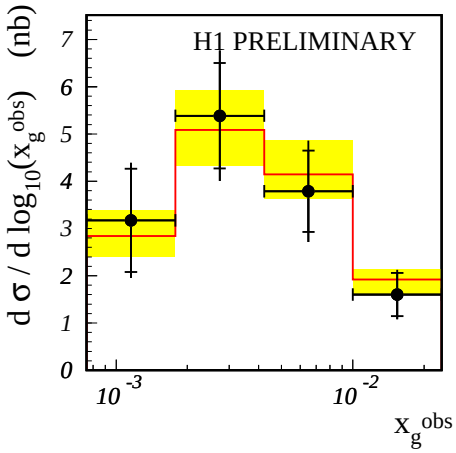

Figure 5.11: Differential charm cross section $\sigma(ep \to eD^*X)$, for $Q^2 > 2$ (GeV/c)^2. as function of the parton momentum fraction x_g^{OBS}, reconstructed from the D^* meson and the scattered electron. The H1 data are shown as points with error bars, the QCD calculations in NLO using the GRV94 HO parton distribution set is shown as solid histogram. The shaded band represents the variation of the cross section due to the variation of the mass of the charm quark between 1.3 and 1.7 GeV/c^2.

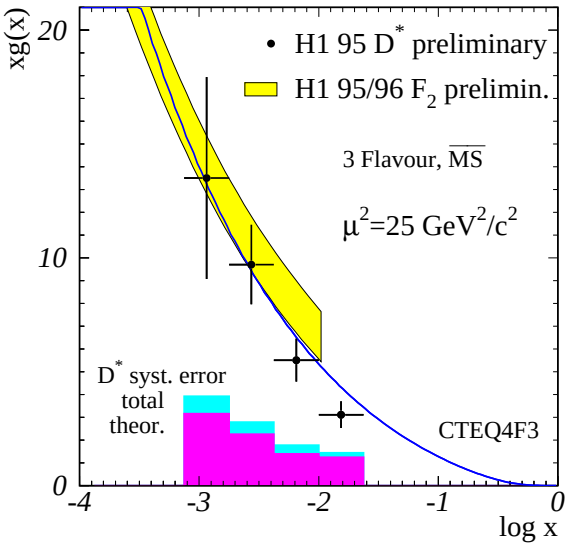

Figure 5.12: Gluon density $x_g g(x_g)$ as function of x_g extracted from the charm production cross section (data points with statistical errors) compared to the result of the H1 QCD analysis of the inclusive F_2 measurement at $\mu^2 = 4m_c^2 + \overline{Q^2} = 24$ GeV^2 (light shaded band). The solid line is the theoretical prediction from the CTEQ4F3 parameterization at this scale (μ^2).

distributions at the level of observable hadrons have recently become available [25]

The programs have been adapted to the H1 analysis, results are also shown in Figure 5.11 (Thesis D. Müller). The QCD program also yields the correlations with the 'true' x_g which can be used to unfold the gluon density from the measured spectrum. The result of such an unfolding procedure is shown in Figure 5.12. There is good agreement with the standard method to extract gluon densities, the QCD analysis of the inclusive structure function F_2, with our method for those data points where the kinematics overlap. This represents a non-trivial confirmation of the applied QCD concepts and of the universality of the parton distributions.

Measurements of differential charm production cross sections are being pursued also in the photoproduction regime (Thesis M. zur Nedden), using a data sample four times as large as the 1994 set that provided the basis of our first publication in this area [24]. There exist several theoretical approaches within perturbative QCD to describe the process, where charm quarks may or may not play a role as active partons in the initial state proton and photon (which can fluctuate into a hadronic state as well). With the increased statistics, it should become possible to identify the kinematic range where these concepts are appropriate and may be used to extract information about parton densities.

Particular interest at HERA has been created by a fraction of about 10% of the DIS events which exhibit the characteristics of a diffractive interaction: the hadronic system recoiling against the scattered electron is separated from the beam axis by a region void of any particle

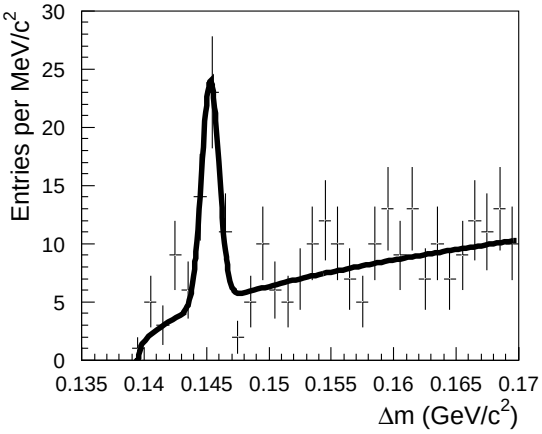

Figure 5.13: The mass difference distribution for $D^{*\pm}$ candidates in diffractive DIS events with no energy deposition in the calorimeter more forward than at pseudo-rapidity $\eta_{max} = 3.2$. The solid line is a Gaussian plus polynomial fit used to extract the signal.

flow. These processes are interpreted as exchange of a color-less object. Charm production holds the promise of providing important keys to the theoretical understanding of diffraction; some kinematic distributions are remarkably sensitive to the dynamics of the underlying exchange [26]. D^* signals in diffractive ep interactions have been reported [19, 24], albeit with very poor statistics. With the integrated luminosity collected in 1997, it will become possible to investigate the phenomenon in detail. The signal obtained from the 1995, 1996 and part of the 1997 data, requiring the most forward energy deposition in the calorimeter and forward detectors to have pseudo-rapidity $\eta_{max} < 3.2$ is shown in Figure 5.13 (Thesis S. Hengstmann). Here the kinematic region is $Q^2 > 2$ GeV/c^2, $p_\perp(D^*) > 1.5$ GeV/c and $x_{I\!P} < 0.005$, where $x_{I\!P}$ denotes the momentum fraction of the exchanged object – generically termed 'Pomeron' – in the proton.

References

[1] Observation of Events at very High Q^2 in ep collisions at HERA, C. Adloff et al., Z. Phys. **C74** (1997), 191 - 205.

[2] A Measurement of the Proton Structure Function $F_2(x, Q^2)$ at Low x and Low Q^2 at HERA, C. Adloff et al., Nucl. Phys. **B497** (1997), 3 - 30.

[3] P. Bruel, High Q^2 DIS results and search for leptoquarks at HERA, XXIII. Rencontres de Moriond, on Electroweak Interactions and Unified Theories, Les Arcs, France, March 1998; available at *http://www-h1.desy.de/h1/www/publications/hiq2/hiq2.html.*

[4] G. Bernardi, New H1 results at high Q^2, talk given at DESY, Hamburg (March 1998); available at *http://www-h1.desy.de/h1/www/publications/hiq2/hiq2.html.*

[5] Observation of Events with an Isolated High Energy Lepton and Missing Transverse Momentum at HERA, C. Adloff et al., to be submitted to Phys. Lett.

[6] Photoproduction of K^0 and Λ at HERA and a Comparison to Deep Inelastic Scattering, C. Adloff et al., Z. Phys. **C76** (1997), 213 - 221.

[7] Low Q^2 Jet Production at HERA and Virtual Photon Structure, C. Adloff et al., Phys. Lett. **B415** (1997), 418 - 434.

[8] Measurement of the Inclusive Di-Jet Cross Section in Photoproduction and Determination of an Effective Parton Distribution in the Photon, C. Adloff et al., Eur. Phys. J. **C1** (1998), 97 -107.

[9] Photoproduction of $\Psi(2s)$ Mesons at HERA, C. Adloff et al., Phys. Lett. **B** (1997), in print.

[10] Inclusive Measurement of Diffractive Deep-Inelastic *ep* Scattering, C. Adloff et al., Z. Phys. **C76** (1997), 613 - 629.

[11] Thrust Jet Analysis in Deep-Inelastic Large-Rapidity-Gap Events, C. Adloff et al., Eur. Phys. J. **C1** (1998), 495 - 507.

[12] Diffraction Dissociation in Photoproduction at HERA, C. Adloff et al., Z. Phys. **C74** (1997), 221 - 235.

[13] Bose-Einstein Correlations in Deep Inelastic *ep* Scattering at HERA, C. Adloff et al., Z. Phys. **C75** (1997), 437 - 451.

[14] Proton Dissociative ρ and Elastic Φ Electroproduction at HERA, C. Adloff et al., Z. Phys. **C75** (1997), 607 - 618.

[15] Measurement of Event Shape Variables in Deep Inelastic *ep* Scattering, C. Adloff et al., Phys. Lett. **B406** (1997), 256 - 270.

[16] Evolution of *ep* Fragmentation and Multiplicity Distributions in the Breit Frame, C. Adloff et al., Nucl. Phys. **B504** (1997), 3 - 23.

[17] Measurement of the Gluon Density in the Proton, Thesis D. Müller (1998).

[18] Heavy quark and jet production by real and virtual photons, F. Sefkow, Proc. 17. Int. Conf. on Physics in Collision, Bristol, England (1997), in print.

[19] A Measurement of the Production of $D^{*\pm}$ Mesons in Deep–Inelastic Diffractive Interactions at HERA, H1 Collaboration, contr. No.pa02-060, Int. Conf. on High Energy Physics, July 1996, Warsaw, Poland.

[20] Determination of the gluon density in the proton from deep inelastic *ep* charm production using NLO QCD, H1 Collaboration, contr. No.275 at Int. Europhysics Conf. on High Energy Physics, August 1997, Jerusalem, Israel.

[21] Improving the z-Vertex Trigger, D. Müller und F.Sefkow, H1 note H1-04/98-539, April 1998.

[22] *ep* physics beyond 1999, H1-collaboration, H1 note H1-10/97-531, November 1997.

[23] H1 high luminosity upgrade 2000, CIP and level 1 vertex trigger, M. Cuje et al., H1 note H1-01/98-535, January 1998.

[24] Photoproduction of $D^{*\pm}$ Mesons in Electron - Proton Collisions at HERA, S. Aid et al., Nucl. Phys. **B472** (1996), 32.

[25] B. W. Harris and J. Smith, Nucl. Phys. **B452** (1995), 109; Phys. Lett. **B353** (1995), 535.

[26] W. Buchmüller, M.F. McDermott and A. Hebecker, Phys. Lett. **B404** (1997), 353.

6 Rare Kaon Decays

S. Pislak, P. Robmann and P. Truöl,
in collaboration with
J. Egger, W. D. Herold, H. Kaspar, and H. Weyer,
Paul–Scherrer–Institut, CH-5234 Villigen
Brookhaven National Laboratory, Upton, NY-11973, USA
University of New Mexico, Albuquerque, NM-87131, USA
University of Pittsburgh, Pittsburgh, PA-15260, USA
Yale University, Newhaven, CT-06511, USA
Institute for Nuclear Research, Academy of Sciences, 117 312 Moscow, Russia
Experiment E-865 at Brookhaven AGS

In Table 6.1 those rare K^+ decay modes are listed, for which we have accumulated a significant amount of data. For the lepton flavor conservation violating decay mode, which our experiment was primarily designed for, we have taken data mainly in 1995 and 1996, and will continue to do so during a final 24 week run from June 1998 to December 1998. The analysis of the 1995 data has been concluded [1, 2] and led to a lower limit for the branching ratio of 2×10^{-10}, similar to what was obtained previously [3]. The 1996 data, which are projected to give a factor of five improvement of this limit are still being analysed. The foreseen run could reach a single event sensitivity of 4×10^{-12} for the forbidden decay.

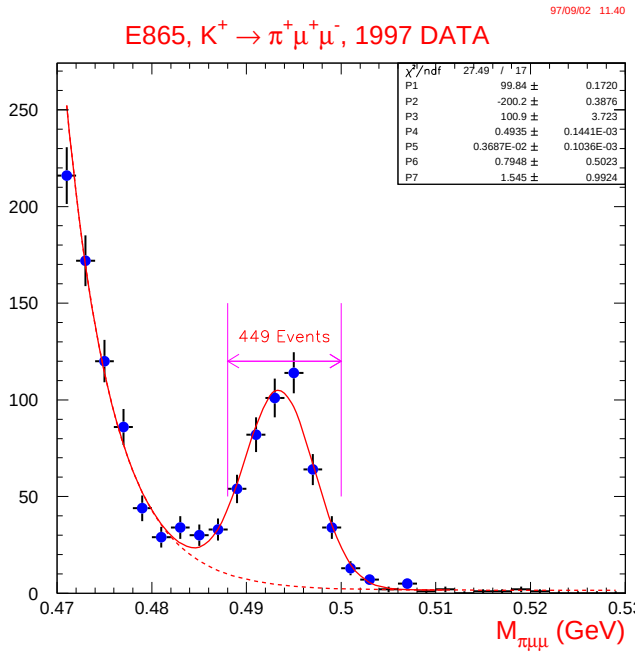

Figure 6.1: The $\pi^+\mu^+\mu^-$ invariant mass spectrum showing a peak at the K^+ mass containing approximately 400 events of the $K^+ \to \pi^+\mu^+\mu^-$ decay.

The data on the other rare decay modes were taken with our broad band K^+ spectrometer during last years run. A new scintillator pixel detector (15×25 pixels of 7×7 mm^2 area and 2 mm thickness viewed by phototubes through air light guides) was installed in the primary beam. This permitted to also look at decays with missing neutrinos or photons. As an example of the quality of this data, we show in Figure 6.1 a mass spectrum indicating a clear peak from about 400 $K^+ \to \pi^+\mu^+\mu^-$ events. As discussed in [4] this sample will provide an accurate test of predictions using chiral QCD Lagrangians. Measuring the branching ratio for the K_{e3} ($K^+ \to \pi^0 e^+ \nu_e$) channel is one of the means of improving our knowledge of the element V_{us} of the CKM-mixing matrix which connects the first and second generation of

quarks. A factor of two in accuracy could be gained by comparing K_{e3} to $K_{\pi 2}$ ($K^+ \to \pi^+\pi^0$) decay. The statistical sample is large. Lastly the radiative decays $K^+ \to \mu^+\nu_\mu e^+e^-$ and $K^+ \to e^+\nu_e e^+e^-$ for which only a handful of events has been observed previously furnish information on the electromagnetic structure of the K^+.

Decay mode	**Branching ratio**	**Number of events**		**Comments**
		World data	**E865**	
$\pi^0 \to e^+e^-e^+e^-$	3.18×10^{-5}	146	2000	π^0 electromagnetic form factor
$\pi^0 \to e^+e^-$	7.5×10^{-8}	29	350	π^0 electromagnetic structure
$K^+_{e3}/K^+_{\pi 2}$	0.221 ± 0.012	3500	≈ 50000	V_{us}, needs $< 2\%$ accuracy
$K^+ \to \pi^+\pi^-e^+\nu_e$	3.7×10^{-5}	30000	≈ 300000	$\pi\pi$ scattering length, chiral QCD
$K^+ \to \mu^+\nu_\mu e^+e^-$	9.5×10^{-7}	27 ± 8	1600	K^+ electromagnetic structure
$K^+ \to e^+\nu_e e^+e^-$	2×10^{-8}	4	200	K^+ electromagnetic structure
$K^+ \to \pi^+e^+e^-$	2.7×10^{-7}	500	7000	branching ratio, chiral pert. theory
$K^+ \to \pi^+\mu^+\mu^-$	$< 2.3 \times 10^{-7}$	0	400	branching ratio, chiral pert. theory
$K^+ \to \pi^+\mu^+e^-$	$< 2 \times 10^{-10}$	0	$< 2 \times 10^{-10}$ (1995) $< 4 \times 10^{-11}$ (1996)	

Table 6.1: Results obtained by experiment E865, for which analysis is in progress.

K_{e4} ($K^+ \to \pi^+\pi^-e^+\nu_e$) decay is the only available source of clean information on $\pi\pi$ $S-$wave scattering near threshold and has for this and other reasons some special significance in the theory of chiral symmetry. The latter theory allows the description of the couplings of pions and kaons using a set of nonlinear Lagrangians, with coefficients, which are to be determined phenomenologically. K_{e4} decay is the simplest process in which predictions can be tested which follow in the limit of large number of colors (N_c) of quantum chromodynamics (QCD) (see Figure 6.2). The tools for a complete analysis of K_{e4} within the spirit of these models exist [5, 6]. The only previous experiment [7] is statistically limited, as e. g. evidenced by the value for the scattering length obtained $a_0^0 = 0.26 \pm 0.05$ (exp.), compared to $a_0^0 = 0.20 \pm 0.01$ (theor.). We have been able to take 3×10^5 events, ten times the present world data, with good phase space coverage. We demonstrate this e. g. with the di-pion mass and angular distributions in Figure 6.3, which show how the shape of the theoretical predictions [6] is hardly modified when the matrix elements are used as input to the Monte Carlo simulation of the experiment [1]. The kinematical variables are indicated in Figure 6.2.

In standard weak interaction theory, the data can be described by a set of model independent form factors, which are functions of the di-pion mass and angle, and the di-lepton mass. The di-lepton angle, and the angle between the lepton and the hadron plane do not enter. The di-pion mass spectrum (from only 4 % of the data) is shown in Figure 6.3, as well as the reconstructed mass of the missing neutrino. The data has undergone various cuts against background sources. The present sample contains less 2 % background events mainly from $K^+ \to \pi^+\pi^-\pi^+$ decay with a pion misidentified as a positron. The di-pion

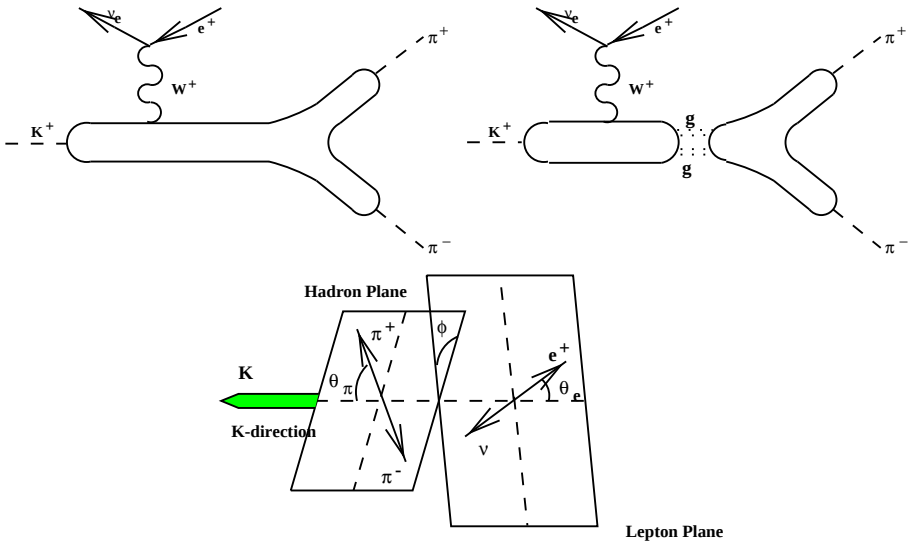

Figure 6.2: Top: two diagrams are shown, which are considered in theoretical treatment of K_{e4} decays using chiral perturbation theory in the limit of large number of colors; the right diagram with the two gluon exchange is of higher order and therefore of reduced importance. Bottom: the kinematical variables which are used in the description of $K^+ \to \pi^+\pi^-e^+\nu_e$ (K_{e4}) decay. θ_π is the angle in $\pi\pi$ center of mass between the π^+ and the $\pi\pi$ recoil direction, θ_e similarly the angle in the $e\nu$ center of mass system between the e^+ and $e\nu$ recoil direction and lastly ϕ is the angle between the dipion and the dilepton decay planes.

spectrum peaks near the low mass kinematical limit of $2m_\pi$, which explains why this data is sensitive to threshold $\pi\pi$ scattering. Some fine tuning of the data analysis is still required, before preliminary values for the scattering length and other form factor parameters can be extracted.

References

[1] S. Pislak, Experiment E865 at BNL: a search for the decay $K^+ \to \pi^+\mu^+e^-$, Thesis, University of Zürich (1997).

[2] D. Bergman, A search for the decay $K^+ \to \pi^+\mu^+e^-$, Thesis, Yale University, Newhaven (1997).

[3] A. M. Lee et al., Phys. Rev. Let. **64** (1990), 165.

[4] R. Appel et al., Experimental studies of rare K^+ decays, Proc. 28-th Int. Conf. on High-Energy Physics, Warsaw, Poland (1996), (World Scientific, Singapore 1997) p. 1188.

[5] C. Riggenbach, J. Gasser, J. F. Donoghue, and B. R. Holstein, Phys. Rev. **D43** (1991), 127.

[6] J. Bijnens, G. Ecker and J. Gasser, CERN-Report TH.6504/92; J. Gasser, private communication.

[7] L. Rosselet et al., Phys. Rev. **D15** (1977), 574.

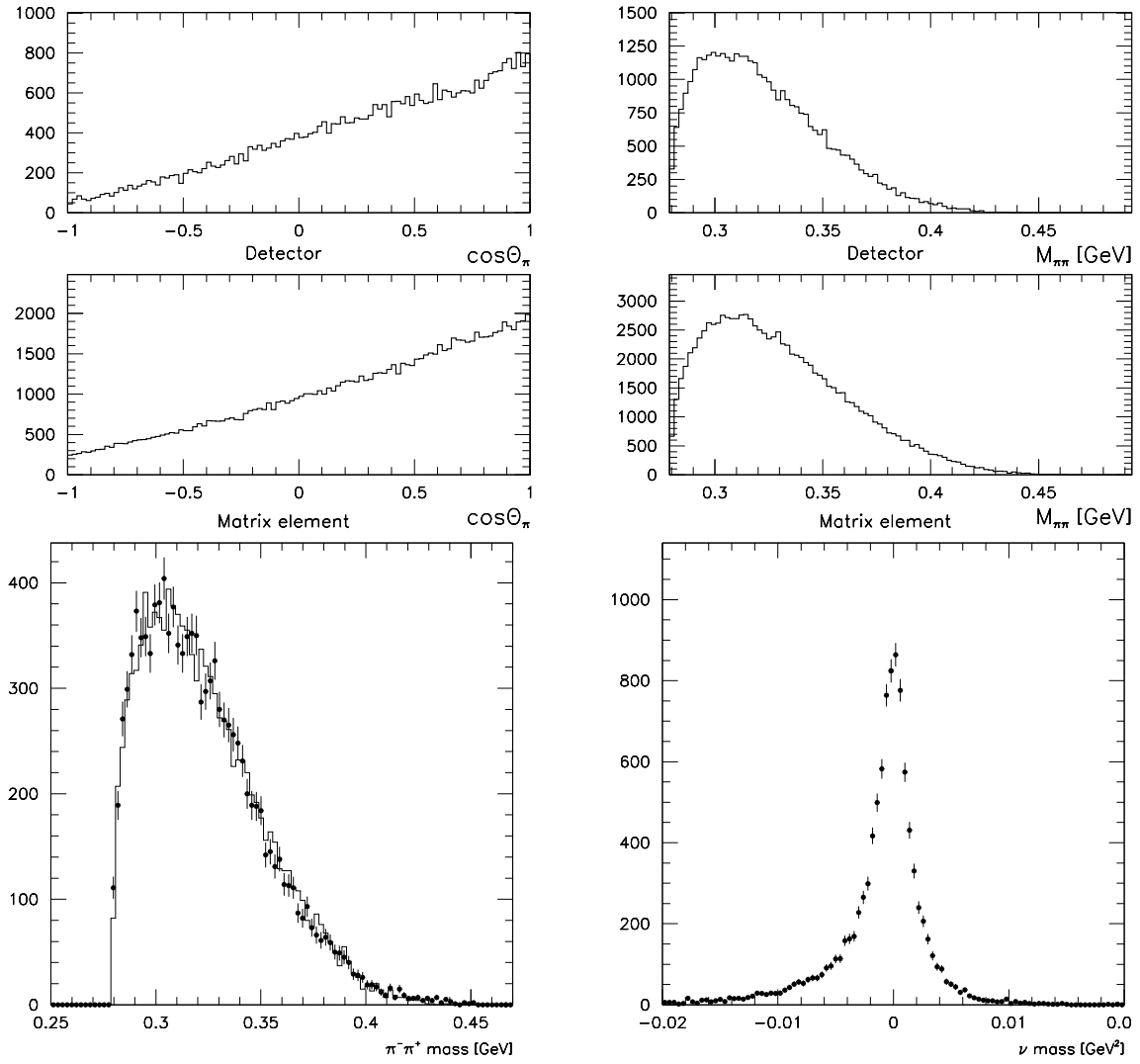

Figure 6.3: Kinematical distributions for K_{e4} decay. Top: theoretically predicted [6] di-pion decay angle and invariant mass distributions without and with detector acceptance folded in. Bottom: di-pion invariant mass and missing neutrino mass distribution for 4 % of the E865 data compared to predictions folded with the experimental acceptance and efficiencies (solid histogram).

7 Neutrino Masses and Mixing

E. Holzschuh, W. Kündig, L. Palermo, and P. Wenk

The masses of the neutrinos are known to be small when compared with the masses of their charged partners. How small is unknown, however. If the neutrino masses are nonzero, it is considered likely that there is also neutrino mixing. In our project we are using β–spectroscopy to investigate these questions. Mixing would mean in this case that the electron neutrino, emitted in β–decay, is described by a superposition of states with two or more different masses m_i. The signature would be a characteristic 'kink' in an otherwise smooth β–spectrum at an energy $E_0 - m_i$, where E_0 is the endpoint energy for zero neutrino mass.

The objective of the project is a systematic search with high sensitivity in the β–decay of the isotopes ^{63}Ni and ^{35}S for neutrino masses up to 100 keV. The spectrometer, auxiliary experiments and some of the data with ^{63}Ni have been described in previous annual reports. During this budget period we have made a ^{35}S source with a new method and have taken data with high statistical precision. Also a computer program was developed to simulate the scattering of electrons in the spectrometer. Recently, P. Wenk has completed his dissertation [1].

The measurements where completed in February 1998. Thereafter we had to disassemble our spectrometer and to remove all parts for the reason that on this location at the Paul-Scherrer-Institute the new Swiss-Light-Source will be built.

7.1 Simulation of scattering

The spectrometer was designed to minimize the probability that electrons scattered from baffles etc. can reach the detector. It could however not completely be avoided and caused a (small) distortion of the measured β–spectra. Experimentally we have investigated scattering by accelerated photo-electrons with energies up to 50 keV. As the scattering distribution is a function of two variables, the initial energy of an electron and the energy with which it is detected, a complete measurement was not feasible. We have developed a Monte-Carlo program to simulate scattering. Figure 7.1 shows a comparison of the simulation with measured data. We find good agreement, but only if the most elaborate cross sections are used. The simulation gives us a good understanding of the scattering and we can use computed scattering distributions to correct the measured β–spectra.

7.2 Results for ^{63}Ni

A β–spectrum of ^{63}Ni was measured with a total of approximately 10^{10} counts. To analyse these high precision data we had to consider a variety of mostly small effects. Experimentally the most important effect is the increase of the accepted solid angle at the source due to acceleration. It was investigated by simulation. Relatively small effects are energy loss in the source layer, scattering in the spectrometer and dead time of the detector. Theoretically the β–decay of ^{63}Ni, assuming a (statically) screened nucleus, is well understood. However, the dynamical response of the atomic electrons to the decay causes quite significant effects. The probabilities for atomic excitation was computed [2] within the sudden approximation. The effect of electron exchange [3] in β–decay was for the first time only recently observed [4]. It is quite significant for our data.

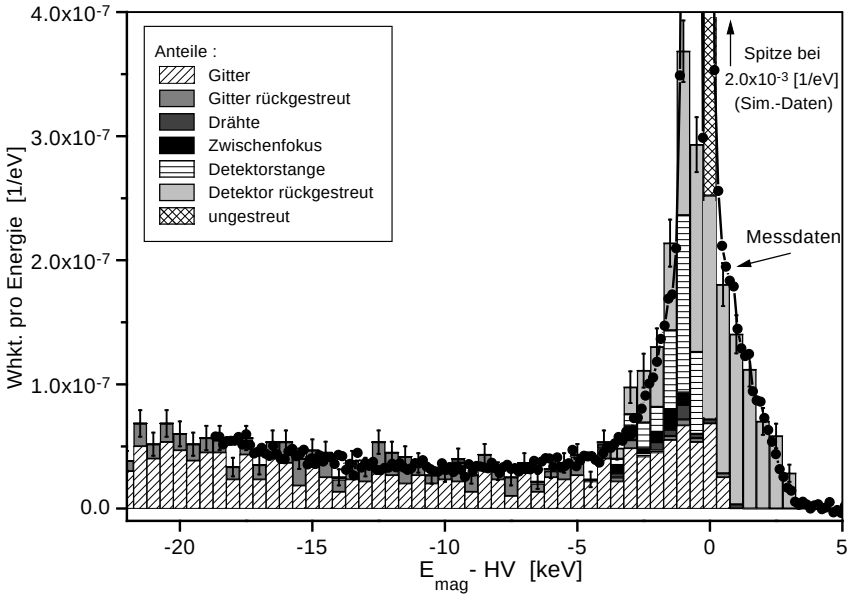

Figure 7.1: *Measured energy distribution (points) of accelerated photo-electrons, scattered in the spectrometer. The central line of unscattered electrons at zero energy (effectively at 40 keV) is a delta–like spike containing* 2×10^8 *counts. It has been suppressed by a factor* 10^4*. The result of the Monte-Carlo simulation is shown as a staircase function, with contributions from various parts of the spectrometer indicated.*

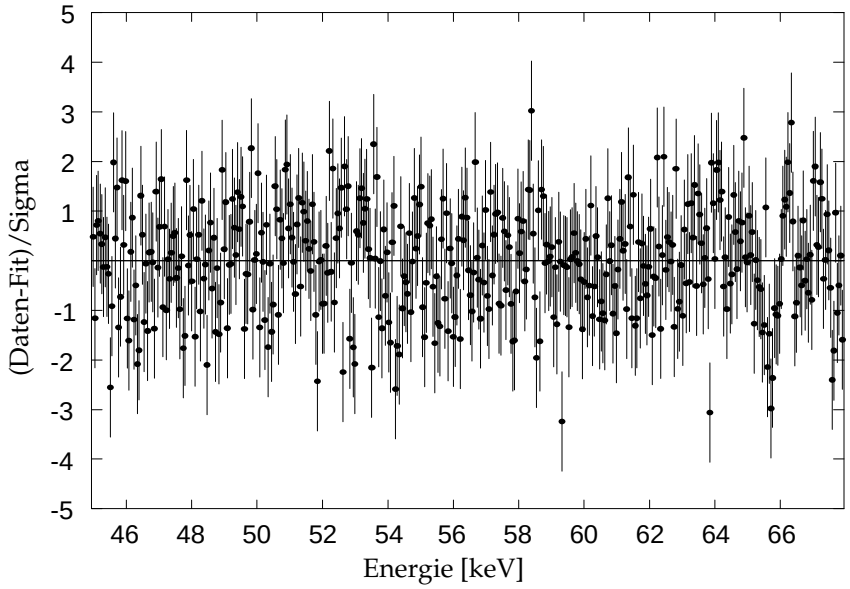

Figure 7.2: *Comparison of the* ^{63}*Ni data and best fit (preliminary) assuming no neutrino mixing.*

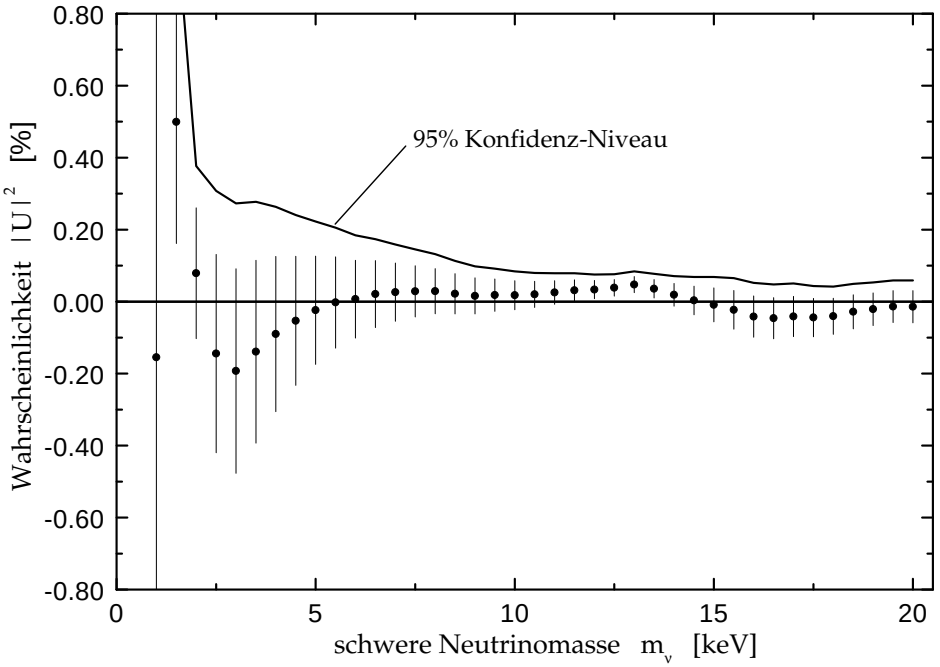

Figure 7.3: *Upper limits for the mixing probability of a heavy neutrino with assumed mass m_ν from the ^{63}Ni data (preliminary). Error bars correspond to the combined statistical and systematical errors.*

Figure 7.2 shows the difference between the data and a best fit, normalized with the standard deviation. The fit is good in general but significant deviations can be recognized close to and below the endpoint ($E_0 = 67\,\mathrm{keV}$). It is caused by a not quite adequate description of the excitation probabilities, mainly for L–shell electrons. An indication for the admixture of a heavy neutrino was not found in the ^{63}Ni data. The fitted mixing probability is plotted in Figure 7.3 for assumed neutrino masses up to 20 keV. The error bars correspond to the combined statistical and systematical errors and the solid line represents an upper limit with 95 % confidence. For small masses the theoretical uncertainty for the excitation probabilities contributes significantly to the total error. We are confident that we can improve on this. Therefore the results above should be considered preliminary.

7.3 The ^{35}S source

A thin and well characterized source is an essential prerequisite for a high precision measurement of a β–spectrum. Historically the isotope ^{35}S was used in many important investigations of the β–decay (see e.g. [5]). Nevertheless there does not seem to be a method in the literature for making good sources. First, we tried vacuum-evaporation of ^{35}S labeled methionine (an amino-acid) [6]. The method worked with non-active methionine. However, the active material decomposed during heating, probably due to radio-chemical effects.

We have found a new method which worked very well and which is also amazingly simple. As source substrate we used a thin foil (2000 Å) of a polyimid (Kapton) with $1.8 \times 3.6\,\mathrm{cm}^2$ area. A thin layer of copper (50 Å) was deposited by vacuum-evaporation on the foil. The foil was exposed to active H_2S in an inert gas. The H_2S gas was made by decomposing commercially available Na_2S with an acid. The copper reacted with the H_2S forming copper

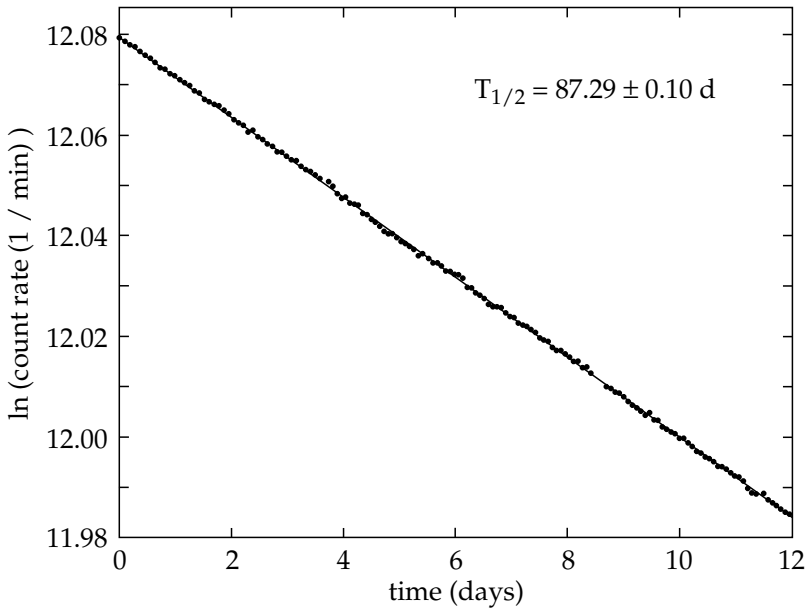

Figure 7.4: *Logarithm of the counting rate for the ^{35}S source as a function of measuring time and fit to an exponential decay curve.*

sulfide. We found that this method has nearly 100% efficiency. The source made had an initial activity of 5.5 mCi. It turned out to be chemically quite stable, also in vacuum. Initially a minor contamination of the spectrometer was observed, probably due to outgassing of H_2S from the foil or the support frame of the source. The counting rate with the ^{35}S source in the spectrometer is plotted in Figure 7.4 for 12 days of measuring time. A fit to a exponential decay curve gives a half-life which is compatible with literature values [7] for ^{35}S, demonstrating the chemical and thermal stability of the source.

7.4 Measurements with ^{35}S

The measurements with the ^{35}S source were started in July 1998 and completed in January 1998. The energy range of the measurements extended from 45 keV up to 170 keV (endpoint of ^{35}S is $E_0 = 167$ keV). This range was divided in five overlapping regions which were measured separately. There were several reasons for doing so. The measurements were performed by stepping a negative high voltage applied to the source. It turned out that this voltage had the required high stability only up to about 40 kV. The solid angle accepted by the spectrometer at the source increases with increasing voltage. For small acceleration it is relatively simple to correct a measured spectrum for this effect. At higher acceleration however, the correction becomes increasingly more complicated and may lead to systematic errors. With the newly made source, the count rate at low energies would have been simply too large. So we started the measurements with the high energy range and moved down as the source decayed. The highest counting rate encountered during the measurements was about 25 000 s^{-1}.

The set of the five measured ^{35}S spectra are shown in figure 7.5. The total number of data points is 1850 containing about 2×10^{10} counts. With such graphs it is thus not possible to show the individual data points let alone the size of the error bars. The upper right graph shows a small part of the data from run A near the endpoint, with error bars still smaller than the size of the data points.

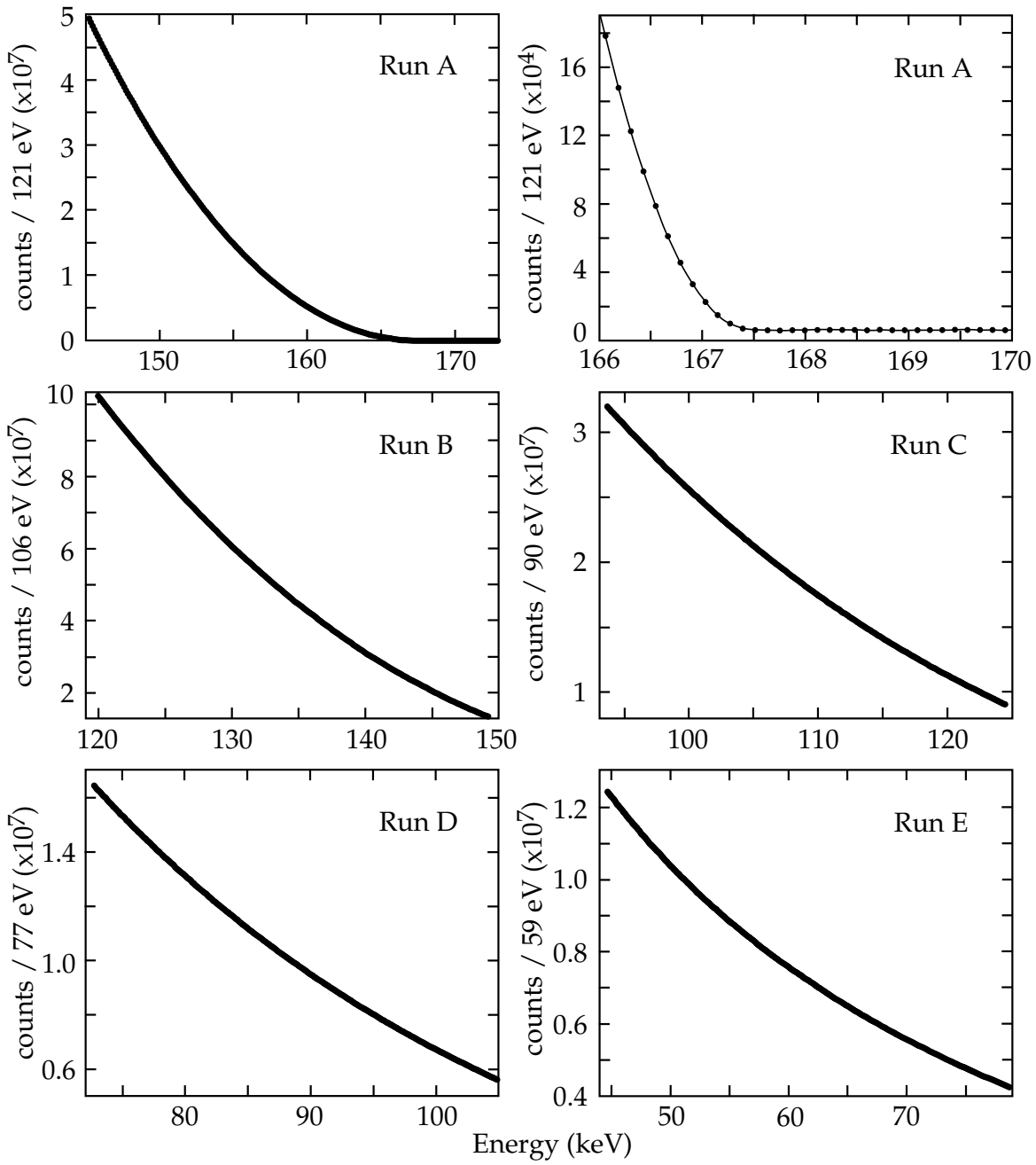

Figure 7.5: *Set of the measured β–spectra of ^{35}S. Part A (right) shows the data near the endpoint.*

The ^{35}S data will be the basis of L. Palermo's dissertation. The analysis of the data is presently in progress. As for the case of ^{63}Ni we have so far not seen an indication for the admixture of a heavy neutrino.

7.5 Conclusion

The measurements have been successfully completed. The acquired data represent by far the most precise β–spectra ever measured with this quality. Besides for the primary purpose of

the project, the search for heavy neutrinos, the data are also useful for testing β–decay theory. Of particular importance in this respect are the various atomic effects, caused by the final state interactions. The theory for these effects is difficult and involves many approximations which cannot rigorously be justified. This is especially true for low energies and a comparison with our data should therefore be useful.

References

[1] . Wenk, Dissertation, Uni. Zürich 1997.

[2] . Schafroth, private communication.

[3] .R. Harston and N.C. Pyper, Phys. Rev. A 45, 6282 (1992).

[4] .C. Angrave *et al*, Phys. Rev. Let. 80, 1610 (1998).

[5] .D. Albert and C.S. Wu, Phys. Rev. 74, 847 (1948).

[6] .M. Apalikov *et al*, JEPT Lett. 42, 289, (1985).

[7] .M. Lederer *et al*, Table of Isotopes, John Wiley, New York, 1978, p. 74–75.

8 Measurement of the Gravitational Constant G

F. Nolting, J. Schurr, E. Holzschuh, and W. Kündig

The most precise published results for the gravitational constant G have claimed uncertainties of about 100 ppm. Such measurements are usually done by some variant of the Cavendish torsion balance [1], but other methods have also been tried. During the last thirty years quite a few experiments have been performed, however without significant progress. What makes things worse, the results show large and unexplained discrepancies indicating that there are not well understood systematic effects.

To overcome these difficulties, we have developed a new method for measuring G. The idea arose from our previous experiment at the Gigerwald storage lake [2,3]. The method has become feasible due to recent progress in the construction of beam balances with extremely high sensitivity. The principle of the experiment will be explained in the following section.

The experiment is set up and running. A first result for G with an uncertainty of 230 ppm was published recently [4] and will briefly be described in this report. Presently, preparations are made for measurements with higher accuracy.

8.1 The principle of the experiment

A schematic view of the experiment is shown in Fig. 8.1. The essential components of the set-up are a single-pan beam balance, two test masses and two large field masses. The test masses (1 kg each) are suspended with thin tungsten wires and alternately connected to the balance. The difference of their weights is measured with high precision and taken as the signal. The balance and the test masses are inside a vacuum system. The field masses are cylindrical in shape and have a central bore such that the test masses can pass through. By moving the field masses between the two positions shown, their gravitational force on the test masses changes the signal. From the difference of the signal for the two states and from

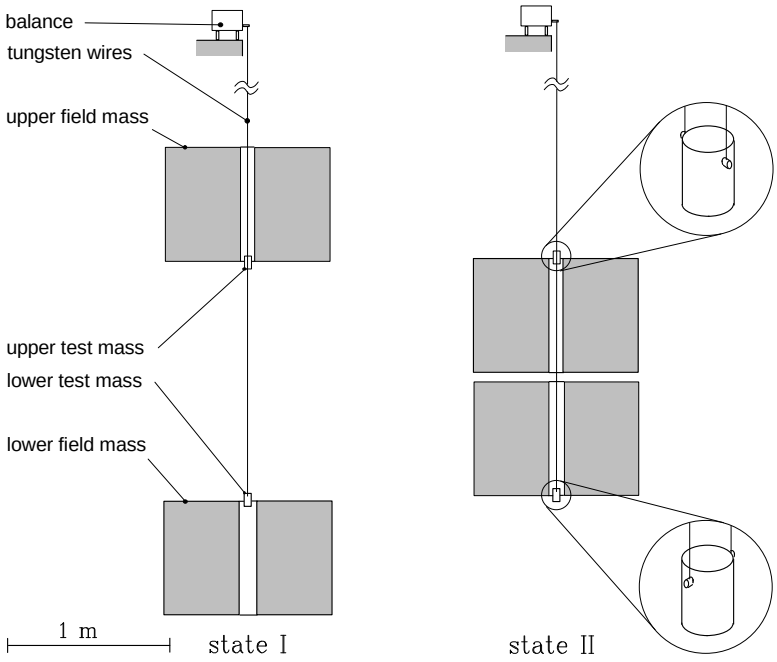

Figure 8.1: *Schematic view of the experiment to measure the gravitational constant. See main text for explanation.*

known values for the masses, densities, and distances, the gravitational constant G can be computed.

There are several features which make this principle of measurement very promising. The test masses are placed at positions where the gravitational force of the field masses has a local extremum. Therefore the relative position of the masses is quite uncritical. The value of G is computed from a double difference and many disturbing forces and drift effects cancel in the result. The field masses are vessels made of stainless steel with a volume of 500 l each. They can be filled with a liquid, either water or mercury. Compared with solids, a liquid is much to be preferred. This is because the density of a liquid is homogeneous, provided its temperature is homogeneous and this can be measured. The effect of compressibility is nearly negligible and can accurately be taken into account. The effect of the vessel walls can be measured with empty vessels and subtracted if necessary. Finally, the balance can be accurately calibrated with the weight of a standard mass.

8.2 First results

The experiment has been set up in a 4.8 m deep pit at the Paul-Scherrer-Institute. This place turned out to be well suited with good mechanical and thermal stability. The beam balance has been provided by Mettler-Toledo. It is the most precise balance, commercially available for comparing 1-kg masses. Since we need to measure only small weight differences, the sensitivity of the balance could be further improved. Detailed descriptions of the experiment have been given in previous annual reports.

The dimensions of the two vessels were measured on a Zeiss precision measuring table. The masses of the vessels were determined with an accuracy of 8 ppm using a precision balance with a measuring range of 500 kg. Hence G could be measured also with the empty vessels, which provided a valuable consistency check (see below).

First measurements of G with water-filled vessels were performed during last year. The procedure for filling in the water was as follows. First, water of high purity was put into containers with a volume of 20 l each and the containers were weighed. Then the water was pumped through a closed system from the containers into the vessels. To prevent air bubbles from being locked in the vessels, the vessels were first evacuated and again just before the last container was filled in. To determine the mass of the water in the vessels, the empty containers were weighed again. The amount of water remaining in the filling system was found similarly. In that way the mass of the water in the vessels could be determined with an uncertainty of 24 ppm.

As a consistency check, the volume of the filled in water was determined using the known density of pure water and compared with the independently measured volume of the vessels. The latter is presently known with 30 ppm uncertainty. Good agreement was found.

The gravitational signal was measured in the following way. The weight of one test mass was integrated for 150 s. Then the other test mass was connected to the balance and its weight measured over the same time interval. The difference of two such measurements is the signal, as defined before. These measurements were repeated for 270 min. Then the field masses were moved from one state to the other (see Fig. 8.1). Before that, the calibration of the balance was checked with a 1 g standard weight (in addition to a test mass). It turned out that the stability of the calibration was good enough and corrections for calibration drift were negligible. The sequence of events above was repeated many times. During the measurements, the temperature was monitored at 10 test points (vessels and vacuum enclosure) and kept constant to within 50 mK in space and time.

The total measuring time with water-filled vessels was three weeks. Two measurements

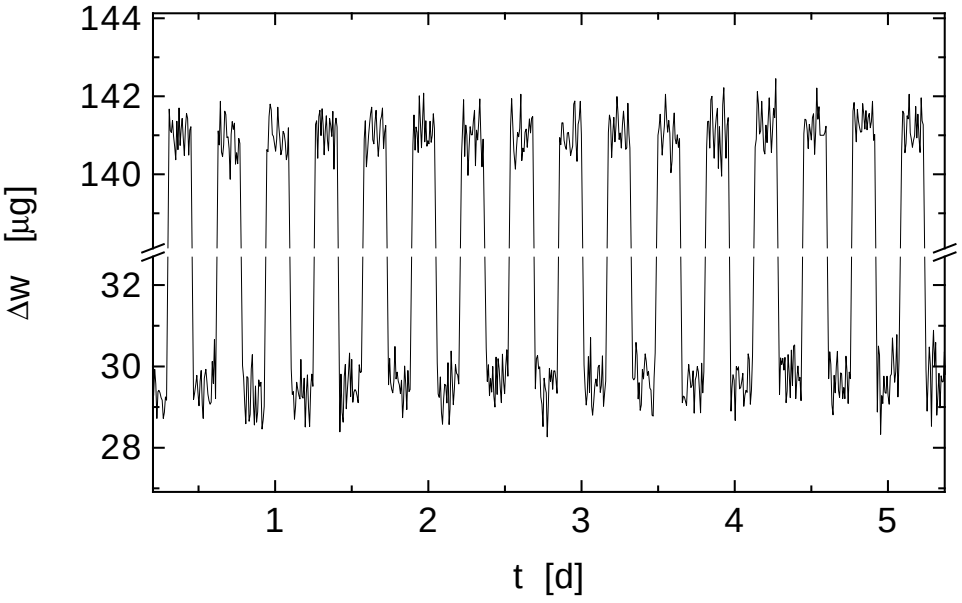

Figure 8.2: *A time series of the weight difference of the test masses, modulated by the gravitational force of the water-filled vessels. The vertical axis has been broken to show the noise.*

with empty vessels, each taking a similar amount of time, were performed before and after the measurements with water. Part of the data with water-filled vessels is shown in Fig. 8.2. The signal amplitude was approximately 111 μg as expected and could be determined with an statistical uncertainty of 8.3 ng or 75 ppm.

To determine G, the gravitational force on the test masses was computed by numerical integration of all movable parts of the field masses. The results from the three measurements

Uncertainties of G	ppm
Systematic effects of the balance	$\leq$ 130
Sorption effects	$\leq$ 45
Integration of mass distribution	$\leq$ 180
Mass of test mass	0.27
Test mass dimension	3
Test mass position	3
Weight of each vessel	8
Density of stainless steel vessels	10
Weight of water	8
Density of water	29
Mass calibration (1 g)	5
Local gravity (g)	0.06
Total	230

Table 8.1: *The systematic uncertainties of G as estimated for the measurement with water. The first group pertains to upper limits of systematic effects whose investigations are not yet completed.*

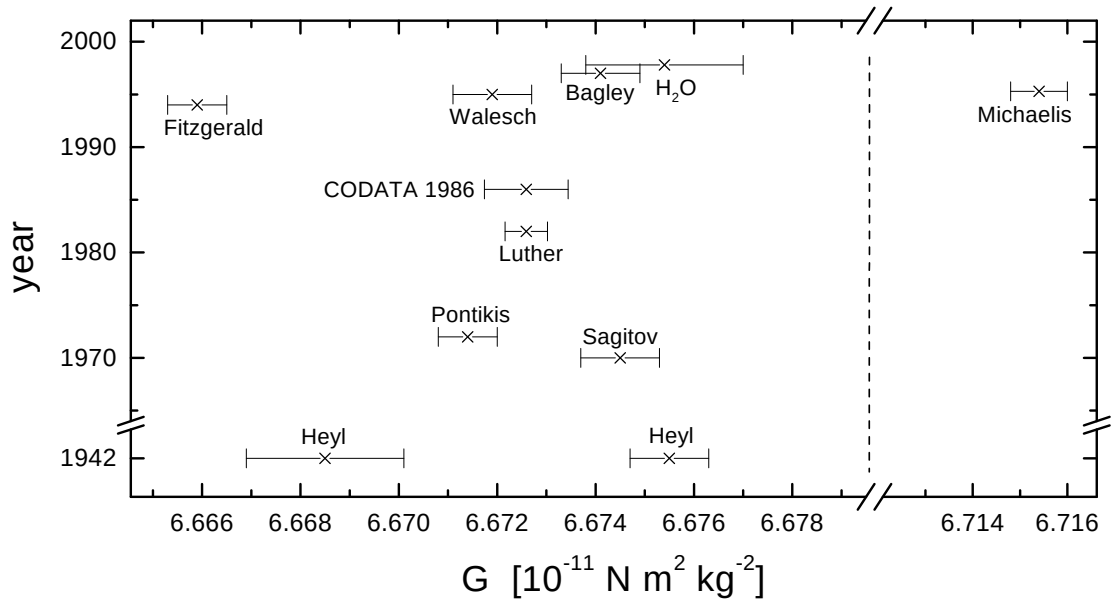

Figure 8.3: *Published results for G with a claimed uncertainty of less than* 300 *ppm [5,...,13]. The present standard value, recommended in 1986 by CODATA, is the value measured by Luther and Towler, but with doubled uncertainty. Our result is labeled 'H_2O'.*

were compatible within their statistical errors. The weighted average is

$$G = (6.6754 \pm 0.0005_{stat} \pm 0.0015_{sys}) \times 10^{-11} m^3 kg^{-1} s^{-2} .$$

The systematical uncertainties are given in Tab. 8.1. These values represent our present knowledge and we expect that the uncertainties can significantly be lowered in the future.

Our first result is compared in Fig. 8.3 with previous measurements. We have included the result of Michaelis *et al.* although likely to be wrong. This is of course well known by these authors. The amazing fact however is that despite much effort no cause could be found. Compared with the other results our value is quite high. In particular, it differs from the present standard value by 420 ppm (about 2σ). At present, we see no reason in our experiment which could explain this discrepancy.

8.3 Preparation for measurements with mercury

The mercury was purchased in 400 flasks, each with a volume of 2.5 l. The total mercury mass is thus 13.6 tons. The specified purity is 99.99 %. Samples were taken from each flask so that later the density can be measured accurately. The mercury was filled into the vessels during last winter with basically the same procedure as previously with water. Each flask was weighed full and empty using a precision balance with a measuring range of 40 kg and a resolution of 10 mg. To minimize uncertainties due to a possible non-linearity of the balance, special calibration weights where used with approximately the same masses as a full or empty flask. About 3000 weighings were necessary, because the weight of each flask, full and empty, was determined from an average of three measurements and the calibration was checked after typically four flasks. In that way the mass of the filled in mercury could be determined with an uncertainty of 2 ppm.

A first measurement with mercury-filled vessels has been started recently. Some preliminary data are shown in Fig. 8.4. The signal amplitude is approximately 785 μg, about 7 times

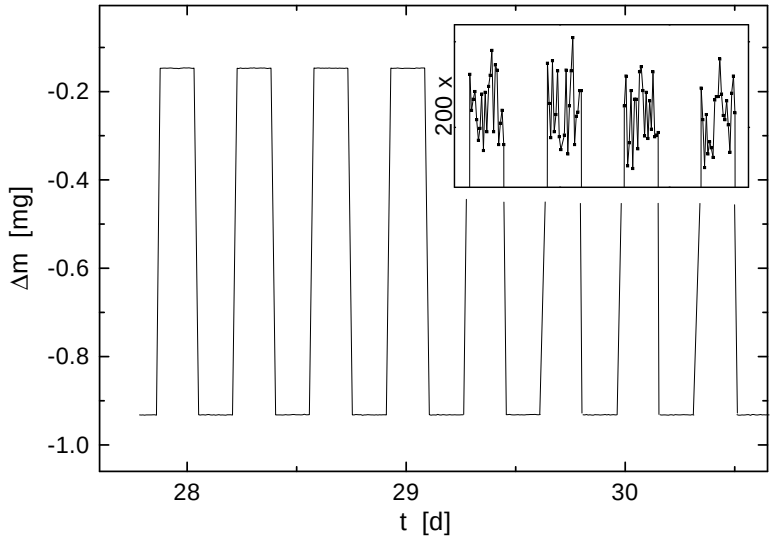

Figure 8.4: *A time series of the weight difference of the test masses modulated by the gravitational force of the mercury-filled vessels. The inset shows the signal with a vertical scale expanded by a factor 200.*

more than with water, and the signal is seen to be very clean. This makes us optimistic that we can achieve significant progress in the near future.

Acknowledgement

We thank the PSI for its hospitality, Mettler Toledo, especially M. Baumeler, for the high precision balance and the calibration of various standard weights. We thank R. S. David from the BIPM for susceptibility measurements as well as J. G. Ulrich and Ph. Richard from the Swiss Federal Office for Metrology for weighing the empty vessels and various calibrations. We thank E. Klingele from the Geodetic Institute of the ETHZ for the measurement of g. We are grateful to B. Schmid and his crew from our machine shop. The experiment was supported by the Swiss National Science Foundation, the Dr. Tomalla Foundation, and the Scientific Research Foundation of the University of Zürich.

References

[1] H. Cavendish, Phil. Trans. R. Soc. London 88, 459 (1798).

[2] A. Cornaz, B. Hubler, and W. Kündig, Phy. Rev. Lett. 72, 1152 (1994).

[3] B. Hubler, A. Cornaz, and W. Kündig, Phy. Rev. D 51, 4005 (1995).

[4] J. Schurr, F. Nolting, and W. Kündig, Phy. Rev. Lett. 80, 1142 (1998).

[5] P.R. Heyl and P. Chrzanowski, NBS J. Res. 29, 1 (1942).

[6] M.U. Sagitov *et al.*, Sov. Astron. 13, 712 (1970).

[7] C. Pontikis, C. R. Hebd. Acad. Sci. B 274, 437 (1972).

[8] G.G. Luther and W.R. Towler, Phys. Rev. Lett. 48, 121 (1982).

[9] E.R. Cohen and B.N. Taylor, Rev. of Mod. Phys. 59, 1121 (1987).

[10] H. Walesch *et al.*, IEEE Trans. on Instr. Meas. 44, 491 (1995).

[11] M.P. Fitzgerald and T.R. Armstrong, Metrologia 31, 301 (1994).

[12] Ch.H. Bagley and G.G. Luther, Phys. Rev. Lett. 78, 3047 (1997).

[13] W. Michaelis, H. Haars, and R. Augustin, Metrologia 32, 267 (1995/96).

Part II
Condensed Matter Physics

There are three solid state physics groups in the department. The main research topics include high-temperature superconductivity, fast ion conductivity, diffusion phenomena and NMR tomography, as well as surface physics and the nanosciences. The research groups profit from a variety of first class equipment for some of the major experimental methods in these fields: nuclear magnetic and quadrupole resonance (NMR/NQR), electron spin resonance (ESR), superconducting quantum interference device (SQUID) and torque magnetometry, angle-resolved X-ray and UV photoelectron spectroscopy (XPS/UPS), laser spectroscopy, scanning tunneling and atomic force microscopy (STM/AFM), as well as muon spin rotation at the Paul Scherrer Institute (PSI) and neuton scattering at the Institute Max von Laue-Paul Langevin in Grenoble (ILL, France). The research activities will also make use of the recently commissioned spallation neutron source (SINQ) at PSI, and of the synchrotron radiation source (SLS, commissioning 2001), where our department is actively involved in the planning of a UV surface science beamline.

A group of theoreticians in computational physics supports the above mentioned experimental groups. The mainly numerical work on high-speed computers comprises investigations such as the microscopic electronic structure of impurities in solids, quantum Monte Carlo simulations and molecular dynamics studies of high-temperature superconductors. In addition the group collaborated with the Institute of Physical Chemistry, the University Hospital and the Department of Neurology.

All research groups enjoy the benefits of national and international collaborations, the most important of which are with ETH Zürich, University of Fribourg, IBM Rüeschlikon, PSI at Villigen and the Synchrotrone Trieste (Italy).

Part II of this Annual Report presents motivations and results on the following projects:

- NMR/NQR Spectroscopy
- Magnetic and Thermal Properties of Superconducting and Related Materials
- Surface Physics
- Laser Dynamics
- Computer Assisted Physics.

9 NMR/NQR Spectroscopy

D. Brinkmann, S. Berger, M. Mali, R. Pozzi, F. Raffa, J. Roos, A. Suter, and A. Zavidonov .
Diploma students: M. Foglia, U. Lehmann, J. Plaz.
Guests: Prof. T. Ohno, Tokushima University, Tokushima (Japan), August till November 1997; Dr. Evgueni Krioukov, Kazan State University (Russia), January/February 1998; Dr. M. Igarashi, Gunma College of Technology, Gunma (Japan), since October 1997.

The NMR/NQR group has continued its general research plan of studying current problems of condensed matter physics by employing NMR (nuclear magnetic resonance) and NQR (nuclear quadrupole resonance) methods. These spectroscopies allow one to investigate electronic properties in solids at a *microscopic* level and thus provide an essential contribution for a better understanding of the materials studied. Our main interest is still devoted to (i) high–temperature superconductors, (ii) their antiferromagnetic parent compounds, (iii) superionic glasses, and (iv) high-pressure NMR/NQR using either the diamond-anvil cell or helium as the pressure medium.

9.1 High-temperature superconductors

Our research interest during the last year was mainly concerned with the following topics: (i) the nature of the pseudo gap in the normal state of high–temperature superconductors and its relation to other normal state electronic effects; (ii) calculation of the dynamic spin susceptibility under various circumstances; (iii) further experimental data for the coupling in the CuO_2 bilayers; (iv) electronic phase separation, and (v) the anomaly in the irreversible magnetization hysteresis curve.

9.1.1 Isotope effect of the spin gap

Recently, we have discovered an electronic crossover occurring in $YBa_2Cu_4O_8$ (1–2–4) around $T^\dagger = 180$ K [1]. The crossover, which is *not* a structural phase transition, involves enhanced charge fluctuations in planes and chains accompanied by a charge (hole) transfer from chain to plane. $T^\dagger$ is relatively close to another temperature, T^*, which is characteristic for underdoped high–temperature superconductors and which refers to the opening of a spin gap (as seen by NMR) in the electron spin excitation spectrum. In 1–2–4, $T^* \approx 150$ K which lies above $T_c = 82$ K. This spin gap effect explains the strong temperature dependence of the normal state susceptibility in 1–2–4. In collaboration with M. Eremin *et al.* from the Kazan State University, we have argued that the spin gap effect in 1–2–4 is caused by a transition due to a charge density wave (CDW) instability [2]. The proximity of $T^\dagger$ and T^* has been a trigger for these theoretical investigations.

The most crucial experimental verification whether the spin gap is related to or triggered by a CDW or spin density wave (SDW) instability, is probably the measurement of the isotope effect, *i.e.* the change, ΔT^*, of the temperature T^* resulting from a change, Δm, of the isotope composition and its dependence on doping level. We have calculated ΔT^* for the case that ^{16}O is replaced by ^{18}O [2]. The result may be expressed in the form of the isotope coefficient $\alpha = (-\Delta T^*/T^*)\,(m/\Delta m)$.

We have performed, together with susceptibility measurements, a high–accuracy NQR determination of the temperature dependence of the planar ^{63}Cu spin–lattice relaxation rate per temperature unit, $1/T_1T$, in several polycrystalline 1–2–4 samples, either enriched with

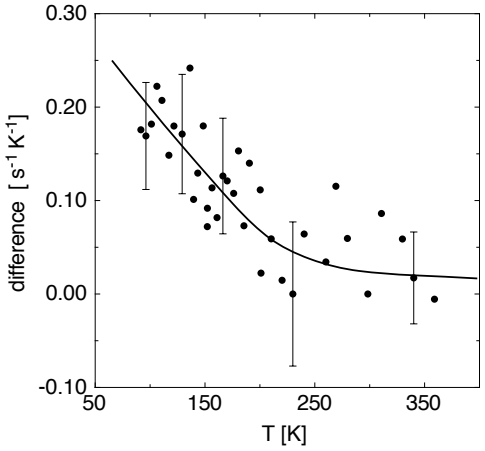

Figure 9.1: *Temperature dependence of the difference of the* ^{63}Cu $1/T_1T$ *values for either* ^{16}O *or* ^{18}O *enriched* $YBa_2Cu_4O_8$ *samples.*

^{16}O or ^{18}O. Figure 9.1 shows that a difference in $1/T_1T$ develops at lower temperatures. The analysis of the measurements reveals that the exponent α is finite and, within the experimental error, is the same for T^* and T_c. This important result implies that the lattice is also involved in the opening of the spin gap, and suggests that the superconducting and the spin gap have a common origin. Recently, it has been concluded [3], based on yttrium NMR Knight shift measurements, that no isotope effect exists. The fact that our relaxation data show a finite isotope effect on the spin gap, points to the necessity to distinguish between the behavior of the dynamic spin susceptibility at zero wavevector (as probed by the Knight shift) and at the antiferromagnetic wavevector (probed by spin–lattice relaxation).

9.1.2 Magnetic properties of Cu–O chains in $YBa_2Cu_3O_7$ and $YBa_2Cu_4O_8$

It is well known that the CDW and SDW transitions become more pronounced in quasi-one dimensional (1D) systems. Therefore, the chains in the $YBa_2Cu_4O_8$ (1–2–4) and $YBa_2Cu_3O_{6+x}$ (1–2–3) compounds represent a convenient system for clarifying the question whether such transitions exist or not. For many years, the analysis of the spin dynamics in cuprates was hampered by the problem how to take into account effects due to electron correlation. To overcome this problem, one may use a Hubbard–like theory extended by including superexchange, to calculate the dynamic spin susceptibility in the so–called fast fluctuation regime. This approach has been successfully used [2] when dealing with the CDW instability scenario described above.

Within the framework of the $t-J$ model, we have now derived a new expression for the dynamic spin susceptibility, which, contrary to the random–phase approximation for usual metals, takes into account effects due to electron correlation. Our results demonstrate that the main features of the magnetic properties of chains in the 1–2–3 and 1–2–4 compounds can be described on the basis of this new expression; in particular, the temperature dependence of both the NMR spin–lattice relaxation rate and the magnetic shift tensor of the chain Cu(1) nuclei in the normal state can be explained this way. The anomalies (non-Korringa behavior) in the relaxation rate can be attributed to the strong temperature dependence of the amplitude of antiferromagnetic fluctuations at the wave vector $Q = \pi$.

Taking into account experimental data, we argue that the temperature dependence of the shift tensor in 1–2–4 provides evidence for the presence, in the double chains, of incommensurate CDW fluctuations, near the wave vector $2k_F$. In this picture, lattice anomalies in the chains, occurring around $T^{\dagger} = 180$ (see above), can be understood, for decreasing temperature, as a crossover from the region with one-dimensional to the region with quasi two-dimensional CDW fluctuations.

9.1.3 Calculation of the dynamic susceptibility

In the antiferromagnetic (AF) phase of the AF parent compounds of high–temperature superconductors, the Cu spins of the CuO_2 planes exhibit long range order and this order is gradually destroyed by doping. Therefore, the understanding of the evolution of the normal state magnetic properties of CuO_2 planes with doping is believed to be a key to elucidate the unusual properties of these superconductors. The hole dynamics in an AF background is perfectly described by the dynamic spin susceptibility which provides direct information about the low energy excitation spectrum and its evolution with doping.

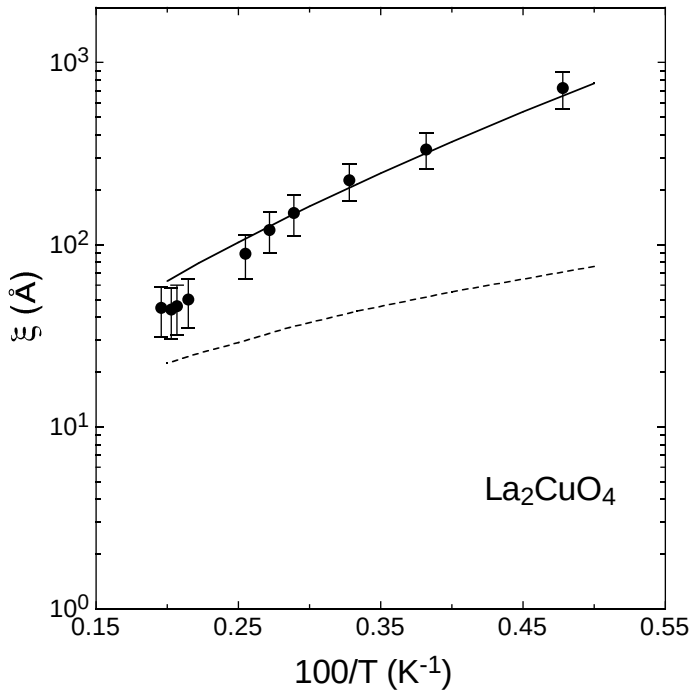

Figure 9.2: *The calculated temperature dependence (solid line) of the antiferromagnetic correlation length, ξ, compared with experimental data (closed circles) for* La_2CuO_4 *and with the result (dashed line) following from the Kondo–Yamaji procedure*

In contrast to other models and theories, we have investigated [4] the dynamic spin susceptibility within a constraint–free theory which may be based, as a natural starting point, on the presentation of the $t - J$ model in terms of Hubbard operators . This presentation obeys rotational symmetry of the spin correlation functions and automatically guarantees the exclusion of double occupancy. Moreover, such a technique allows to take into account the magnetic effects near half filling of the energy bands where the random phase approximation does not work. By taking into account both electron and AF spin correlations, we

have calculated the dynamic spin susceptibility of CuO_2 planes in high–temperature superconductors. Our model is able to reproduce the main features of the temperature and doping dependence of the AF correlation length in doped compounds (*e.g.* $La_{2-x}Sr_xCuO_4$) and in the pure Heisenberg antiferromagnet like La_2CuO_4 (see Figure 9.2) where our model is superior to the old Kondo–Yamaji procedure.

9.1.4 Inter– and intra–plane coupling

Superconductivity in Y–Ba–Cu–O compounds takes place in the CuO_2 planes which form double planes or bilayers. The coupling between individual planes of a bilayer and its influence on the spin dynamics are one of the most important topics in present research. In the past, we have performed extensive NQR/NMR studies of $Y_2Ba_4Cu_7O_{15}$ (2–4–7) by measuring various planar Cu NQR/NMR parameters such as different relaxation times and the Knight shift. We found that all these parameters, which are related to the wavevector and frequency dependent electron spin susceptibility, exhibit a common temperature dependence in the normal phase of 2–4–7; this result had been interpreted as the signature of a coupling between adjacent planes within a bilayer.

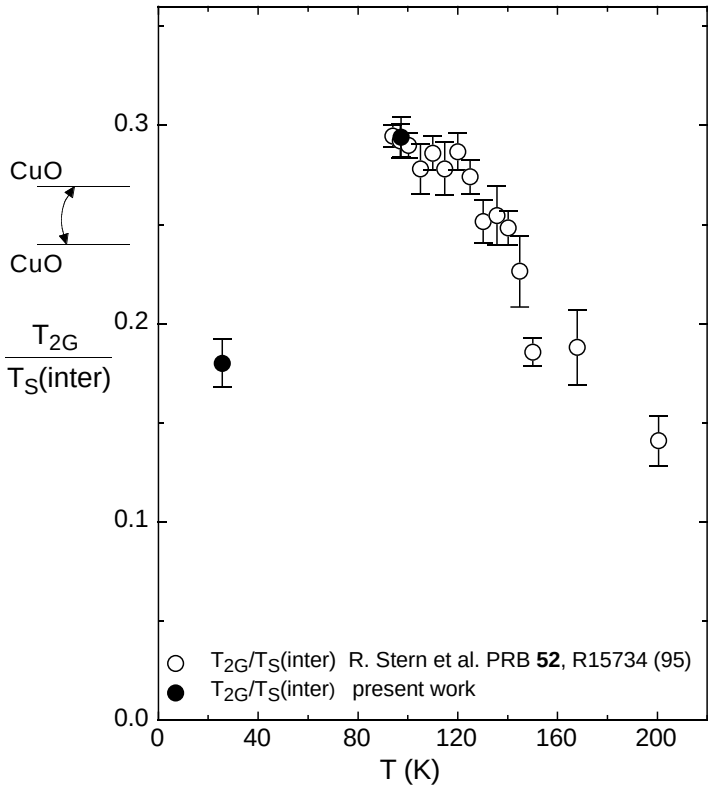

Figure 9.3: *Temperature dependence of the ratio of the relaxation rates* $1/T_{2G}$ *and* $1/T_S$ *which are measures for the intra– and inter–plane coupling, respectively.*

Then, by performing NQR spin–echo double resonance (SEDOR) experiments [5], we have confirmed independently and directly the existence of the inter–plane coupling in 2–4–7 and have determined the temperature dependence of the inter–plane component of the static electron spin susceptibility in the normal state. We have now extended those studies into the superconducting phase by again performing SEDOR NQR with the planar Cu sites in 2–4–7.

Our data (see Figure 9.3) suggest that, within a bilayer, the single planes, which are strongly coupled in the normal state, decouple in the superconducting state.

9.1.5 Electronic phase separation

Whether an electronic phase separation is present in some high–temperature superconductors is still a controversial topic. Extensive NQR studies to elucidate the problem have been performed by the group of M. Teplov of the Kazan State University. In particular, they have studied $TmBa_2Cu_4O_8$ (Tm124) which has a $YBa_2Cu_4O_8$ (Y124) structure and the same superconducting properties as Y124. Previous investigations of the Cu(2) NQR in Tm124 have revealed some specific features of the spectra which were interpreted in terms of an electronic phase separation.

To gain new insight into the inhomogeneous distribution of holes in the CuO_2 planes, we have performed, in collaboration with the Kazan group, Cu NQR studies in Zn doped $TmBa_2(Cu_{1-x}Zn_x)_4O_8$ [6]. Two samples were used, one with x=0 (Tm124) the sample already used before, the other with x=0.027. Among others, a sharp increase of the Cu linewidth in Tm124 was found when the sample became superconducting. Such an increase is also present in $YBa_2Cu_3O_7$ and $TmBa_2Cu_3O_7$.

The origin of this broadening can hardly be associated with crystal structure imperfections since, as known from literature, X-ray and neutron diffraction studies show no appreciable excess distortions of the crystal structure below T_c. On the other hand, the broadening of the Cu(2) NQR spectrum can be described fairly well by the following model. Cu(2) nuclei possess two slightly different NQR frequencies due to two different states differing by their hole concentration; the lifetimes for residing in these states are different. If one assumes a re-distribution of these lifetimes when the sample becomes superconducting, the broadening can be explained. The fit of the model to the experimental data is quite satisfying.

9.1.6 Checking the "fishtail" effect

There is an anomaly in the irreversible magnetization hysteresis curve in single crystals of 1–2–3, often referred to as "fishtail effect": the magnetization increases anomalously on increasing the magnetic field. This feature is still of particular interest since the high critical currents calculated from the maximum of the magnetization curve suggests that even at high fields large critical currents can be passed through the 1–2–3 material.

It is a striking feature of *highly pure single crystals* of $YBa_2Cu_3O_{6.9}$ (1–2–3–6.9) that the fishtail effect can be switched off and on in a reversible manner by changing the annealing temperature. Erb *et al.* [7] have proposed the following model. Annealing the crystal at 510 K (and 1 bar oxygen pressure) causes clustering of the oxygen vacancies and the clusters form pinning centers which then lead to the fishtail effect. However, annealing the same sample at 650 K (and 100 bar), produces a random distribution of the vacancies which are now too small to act as pinning centers. In $YBa_2Cu_3O_7$ (1–2–3–7), no fishtail effect could be observed due to the absence of vacancies.

Cu NMR is the appropriate method to check this hypothesis because the resonance frequency of copper nuclei depends on their oxygen coordination. In 1–2–3–7, only two very sharp lines have been found corresponding to planar Cu(2) and to four-fold coordinated chain Cu(1). This indicates filled chains and confirms the extremely low defect concentration of this state. In 1–2–3–6.9 annealed at 510 K, these two lines become much broader and the

Cu(2) signal even exhibits three distinct peaks. Furthermore, two additional lines were detected. One line has been assigned to two–fold coordinated Cu(1) which implies the presence of sections of empty chains. This clearly proves that part of the oxygen vacancies are now clustered. The assignment of the second additional line is still controversial; it could be related to the interface between filled and empty chains. These investigations and experiments with 1–2–3–6.9 annealed at 650 K are in progress.

9.1.7 Mixed magnetic and quadrupolar spin–lattice relaxation

In many of our recent relaxation time experiments in superconductors, we observed the presence of both magnetic and quadrupolar time dependent interactions, for instance in copper relaxation studies. This is a situation quite common in condensed matter NMR. The question arises whether it is possible to deduce, directly from the experiment, the admixture of a weak contribution, for instance due to quadrupolar interaction, to the overall relaxation. In other words, how sensitive is the form of the magnetization recovery law in respect to the two types of interactions?

We have now performed calculations for a static quadrupolar perturbed Zeeman Hamiltonian in the presence of mixed magnetic and quadrupolar time dependent interactions [8]. This is done for three cases differing by the initial conditions and for spins $I = 1$, $I = 3/2$, and $I = 5/2$; the spin $I = 7/2$ is treated for magnetic fluctuations only. Most results are exact; approximate solutions were found for the general case of $I = 5/2$. We analyzed the whole parameter space constructed by the probabilities for magnetic and quadrupolar induced transitions. This is a necessity when dealing with single crystals or partial oriented powders, since in these cases the different contributions of the fluctuations depend on the angle they form with the external magnetic field, so that extended parts of the parameter space are sampled. We also investigated how sensitive the form of the recovery law of the magnetization is in respect to additional fluctuations (*e.g.* additional quadrupolar fluctuations in the presence of predominantly magnetic fluctuations), in order to determine whether it is possible to extract directly from the recovery law the magnetic and quadrupolar contributions.

We found that, in a surprisingly large region of the transition probability parameter space, it is almost impossible, within experimental errors, to separate magnetic and quadrupolar contributions to the relaxation. Instead, the "dominant" contribution determines the time evolution of the recovery law, *i.e.* the system can approximately be described by a single time constant, T_1^{eff}. In other words, even if the initial assumption of the experimentalist is wrong (lets say, the assumption of pure magnetic fluctuations), the extracted T_1 is of the right order of magnitude.

Thus, to test any hypothesis about the origin of the spin–lattice relaxation in the system under consideration, additional information is necessary. This may be provided by the temperature dependence of the relaxation or by the differing results obtained from different isotopes of the respective element. If single crystals are available, the relaxation's angular dependence yields valuable information. Because of the different transformation behavior of the electric field gradient tensor and the external magnetic field, a certain relaxation channel may vanish for a given orientation.

9.2 Antiferromagnetic parent compounds

Our interest is focused on the electronic and magnetic structure of antiferromagnetic (AF) parent compounds from which many high–temperature superconductors are derived. In de-

Figure 9.4: *Comparison of the plane* Cu(2) *spin–lattice relaxation rate,* W_c*, with theoretical prediction in the RC regime for various antiferromagnetic compounds.*

9.2.2 Internal magnetic field at oxygen sites in $YBa_2Cu_3O_6$

As to the AF phase of $YBa_2Cu_3O_6$, we are interested in the temperature dependence of the internal magnetic field which is created by the sublattice magnetization. While the internal field at the Cu site has been measured by other groups, we have studied, in previous work [11], the field at the Ba site and have now extended the investigation to the oxygen site; the reason is as follows.

When calculating the field at the Ba site, we found that assuming point like magnetic moments at the Cu(2) sites yields fields which are three times larger than the experimental value. In a second approach, extended $3d_{x^2-y^2}$ electrons are assumed and their dipolar field is computed by evaluating the integrals over the spherical functions of these electrons [12]. However, the effect of finite size and anisotropy of the Cu d electrons is only in the order of a few percent. A possible explanation of the discrepancy between these values and the experimental result could be the copper–oxygen covalence. If one assumes that part of the magnetic moment is located at oxygen ions, which corresponds to an extension of the "magnetic moment distribution", the dipolar field at the Ba site would be reduced.

To test this idea, we have measured the internal field at the two oxygen sites in the CuO_2 plane using a high–quality single crystal (synthesized by A. Erb, University of Geneva) with enriched ^{17}O [13]. The components of the magnetic field vector and the electric field gradient tensor have been determined. The magnetic field at the planar oxygen sites has a value of 0.6 Tesla which cannot be explained by assuming point like magnetic moments located at the Cu(2) sites. This result supports our conclusion from the Ba experiments and calls for an elaborate quantum mechanical calculation of the internal field. This then will provide further information on the basic question about the hybridization of copper and oxygen orbitals.

9.2.3 The antiferromagnetic phase of $Ca_{0.85}Sr_{0.15}CuO_2$

The present work in $Ca_{0.85}Sr_{0.15}CuO_2$ (CASCO) is a continuation of our previous NMR and NQR studies of its AF [14] and PM [15] phase. CASCO is the undoped parent AF system of the infinite-layer superconductors with a Néel temperature of 539 K. This study is complimentary to our previous and present investigations of the antiferromagnet $YBa_2Cu_3O_6$.

In CASCO, the intra-plane Heisenberg superexchange integral is $J \approx 1500$ K, as in the more popular La_2CuO_4 (LACO), while the relatively strong inter-plane coupling ($J' \approx 10$ K with respect to $J' \approx 5 \times 10^{-2}$ K in LACO) makes it peculiar in the category of layered cuprates. In particular, the large J' is expected to affect the Cu^{2+} spin-dynamics and is considered an important ingredient for a high value of T_c.

We have now performed the first complete study of the in-plane Cu nuclear spin-lattice and transverse relaxation in the AF phase of CASCO. We studied two different samples. From their T_N values and by information extracted from spin-lattice relaxation, we determined the presence of a small amount of holes introduced by Ca and Sr vacancies into the CuO_2 plane, namely about 4.9 $\times 10^{-4}$ and 1.1 $\times 10^{-4}$, respectively.

The spin-lattice relaxation is strongly affected by the low energy excitations induced by the presence of holes. In particular, the rate maximum at 40 K is induced by the diffusive motion of the holes. The values for the distribution of activation energies characterizing the diffusive process is the same for the two samples, and it is very similar to the one obtained for CuO:Li by Caretta *et al.* [16].

The transverse relaxation rate is mainly driven by the spin-spin indirect coupling, and this is true for the whole temperature range. The most surprising result of this work is the strong dependence of the spin–spin indirect coupling on the hole concentration. The reason

for this probably is that the electronic spin susceptibility, taken at the AF wavevector, depends strongly on hole concentration, at least in the limit of very low doping.

9.3 Superionic glasses

9.3.1 Relaxation of the stationary ion

Our investigation of lithium conducting phosphate glasses of composition $x\mathrm{LiF}\cdot(1-x)\mathrm{LiPO_3}$, where the addition of the dopant salt, LiF, enhances the conductivity, have reached an important result. Our objective has been to monitor the ionic diffusion in these glasses from the point of view of both the stationary and the mobile ions. Relaxation time measurements, in particular, yield information about the correlation function of the fluctuating fields caused by ion diffusion. These advantages had been exploited when we used ^{7}Li, ^{6}Li and ^{19}F NMR to study these glasses (with $x = 0$; 0.30 and 0.35). However, all NMR studies in glasses are hampered by the intrinsic disorder of the structure. Hence, the temperature dependence of the spin-lattice relaxation is usually not described by the Bloembergen–Purcell–Pound (BPP) theory which is based on an exponentially decaying correlation function and which has been very successfully applied in liquids and some solids, including some *crystalline* superionic conductors.

We have circumvented the deviations from the BPP behavior by a modification of the BPP model which is physically obvious and results in a small number of adjustable parameters. Because of the intrinsic disorder of the glass, we have assumed a distribution of those activation energies which are associated with the ion diffusion process. We have obtained a consistent description of the relaxation rates of the stationary ^{31}P in the *undoped* glass, $\mathrm{LiPO_3}$, by covering a wide frequency range (from 34 kHz to 81 MHz) [17]. We have now applied the model to the ^{31}P relaxation in a *doped* glass, namely $0.35\mathrm{LiF}\cdot0.65\mathrm{LiPO_3}$. Choosing ^{31}P rather than ^{19}F simplifies the analysis of the data because so–called quadrupolar effects, which complicate the interpretation of ^{7}Li and ^{6}Li data, are absent. Our results agree quite well with conductivity data.

9.3.2 Magic angle spinning

We have now installed and tested our *magic angle spinning* (MAS) device. In this technique, one rotates the whole NMR sample about an axis which makes the "magic angle" α with the external magnetic field; α is determined by $3\cos^2\alpha = 1$. MAS makes the time averaged dipolar coupling to vanish, it eliminates chemical shift anisotropies and first–order quadrupole couplings. However, the signals obtained without MAS should not be too broad; therefore, in many of our superconductor studies, MAS could not be employed.

We have now obtained the first MAS spectra, namely in the superionic glass $x\mathrm{LiF}\cdot(1-x)\mathrm{LiPO_3}$. By introducing LiF, non–bridging P–F segments are created and a second ^{31}P signal appears which can be resolved from the signal obtained in the undoped glass only by MAS. Figure 9.5 shows these two signals and the dependence of their intensities on the amount of doping, *i.e.* the parameter x. Detailed experiments are in progress.

9.4 High–pressure NMR

After a long break due to a shortage of manpower, we have resumed our work with the diamond-anvil cell (DAC). We have improved the system and we intend to extend the exper-

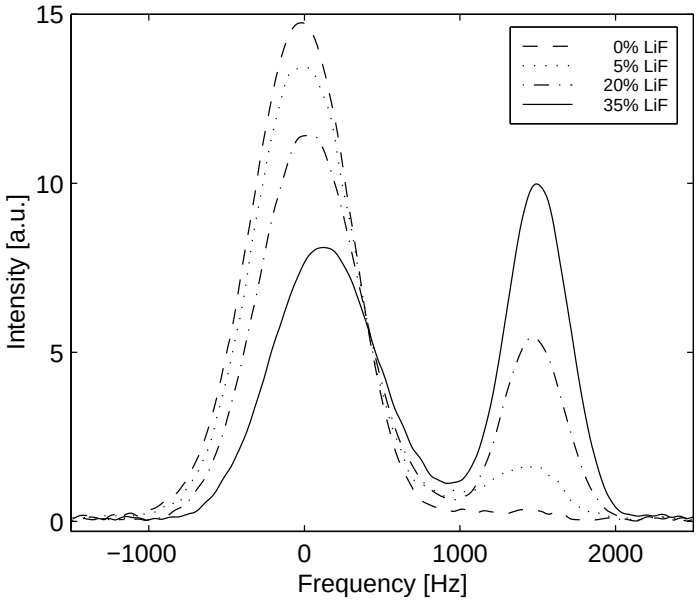

Figure 9.5: *MAS spectrum of the two* ^{31}P *signals in* xLiF$\cdot(1-x)$LiPO$_3$ *for various doping levels.*

iments with the antiferromagnet $Ca_{0.85}Sr_{0.15}CuO_2$ (CASCO) to pressures above 1 GPa.

9.4.1 Pressure induced shift of T_N in $Ca_{0.85}Sr_{0.15}CuO_2$

Using our helium-pressure device, we have measured the pressure variation of the temperature dependence of the sublattice magnetization of the antiferromagnet CASCO (see also above) by employing the internal magnetic field for doing ^{63}Cu NMR. In the temperature range 81 to 344 K, where we performed the experiment, the Cu Larmor frequency linearly increases proportional to the applied pressure, at least up to 0.6 GPa (see Figure 9.6). From the data we determined both the relative reduction of the magnetization for certain pressure and the relative reduction of the magnetization at ambient pressure. The difference between both magnetizations increases with increasing temperature. This is strong evidence that a pressure induced shift of T_N exists. By rescaling the temperature and assuming no change of the dimensionality, the relative shift of T_N has been estimated to be 0.018 $(GPa)^{-1}$. This value has the same order as that reported for La_2CuO_4. As a "by-product", we have determined the pressure dependence of the Cu quadrupole coupling.

9.4.2 Improvements of the diamond-anvil cell

A crucial part of the DAC is the gasket which houses the sample hole into which one places the substance under investigation together with the pressure transmitting mineral oil. In our earlier experiments, we used rhenium metal [18] and the beryllium–copper alloy Berylco [19]. We performed an extensive search for a better material including non-metallic substances which should not only resist high pressure but also should not suffer plastic deformation due to the applied forces. We settled on a Ni-Cr alloy and then investigated various geometrical arrangements of gasket and radio–frequency coil. We finally found a gasket with 0.7 mm hole diameter suitable to contain 300 μg of CASCO. This set–up yielded a sufficiently large signal–to–noise ratio of the ^{63}Cu NMR signal at ambient pressure. It should be noted that

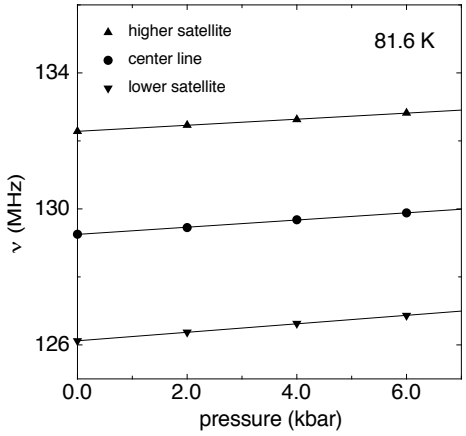

Figure 9.6: *Pressure dependence of the three lines of the quadrupole splitting of* ^{63}Cu *in* $Ca_{0.85}Sr_{0.15}CuO_2$. *The frequency of the "center" line is a measure for the sublattice magnetization.*

our previous DAC experiment were dealing with Na, Li, and Cs samples where *all* nuclei (or 92.5% in the case of Li) are NMR sensitive. In CASCO, only a fraction of nuclei contributes to the ^{63}Cu signal thus demanding a larger sample.

A second improvement concerns the optical system for pressure measurement where the old equipment has been replaced by a commercial spectrometer. The new DAC set–up is now ready for extending the above mentioned CASCO experiments into the pressure range beyond 1 GPa.

References

[1] A. Suter, M. Mali, J. Roos, D. Brinkmann, J. Karpinski, and E. Kaldis, Phys. Rev. B 56 (1997) 5542

[2] I. Eremin, M. Eremin, S. Varlamov, D. Brinkmann, M. Mali, and J. Roos, Phys. Rev. B 56 (1997) 11305

[3] G.V.M. Williams, J.L. Tallon, J.W. Quilty, H.J. Trodahl, and N.E. Flower, Phys. Rev. Lett. 80 (1998) 377

[4] A. Yu. Zavidonov and D. Brinkmann, submitted to Phys. Rev. B (1998)

[5] R. Stern, M. Mali, J. Roos, and D. Brinkmann, Phys. Rev. B 52 (1995) R15734

[6] A.V. Dooglav, A.V. Egorov, E.V. Krjukov, Yu. A. Sakhratov, M.A. Teplov, D. Brinkmann, M. Mali, J. Roos, J. Karpinski, and E. Kopnin, Z. f. Naturforsch., in press

[7] A. Erb, J.Y.Genoud, F. Marti, M. Däumling, E. Walker, and R. Flükiger, J. of Low Temp. Phys. 105 (1996) 1033

[8] A. Suter, M. Mali, J. Roos, and D. Brinkmann, submitted to J. of Physics: Condensed Matter

[9] M. Mali, I. Mangelschots, H. Zimmermann, and D. Brinkmann, Physica C 175 (1991) 581

[10] R. Pozzi, M. Mali, J. Roos, D. Brinkmann, A. Erb, and R. Flükiger, Swiss Workshop on Superconductivity and Novel Metals, Les Diablerets, Sept. 29 - Oct. 1, 1997

[11] A. Lombardi, M. Mali, J. Roos, and D. Brinkmann, Phys. Rev. B 53 (1996) 14268

[12] E.P. Stoll, Helv. Phys. Acta 66 (1993) 449

[13] Spring Meeting of the SPS (1998) and to be published

[14] A. Lombardi, M. Mali, J. Roos, D. Brinkmann, and I. Mangelschots, Phys. Rev. B 54 (1996) 93

[15] R. Pozzi, M. Mali, M. Matsumura, F. Raffa, J. Roos, and D. Brinkmann, Phys. Rev. B 56 (1997) 1

[16] P. Carretta, M. Corti, and A. Rigamonti, Phys. Rev. B 48 (1993) 3433

[17] S. Berger, J. Roos, A.Yu. Zavidonov, and D. Brinkmann, Solid State Nucl. Magn. Res. (1998) in press

[18] R. Bertani, M. Mali, J. Roos, and D. Brinkmann, Rev. Sci. Instrum 63 (1992) 3303

[19] St. Kluthe, R. Markendorf, M. Mali, J. Roos, and D. Brinkmann, Phys. Rev. B 53 (1996) 11369

10 Magnetic and Thermal Properties of Superconducting and Related Materials

H. Keller, C. Aegerter, J. Hofer, V.A. Ivanshin (visiting scientist), S. Romer (till Feb. 98), A. Schilling (since Oct. 97), A. Shengelaya, M. Willemin, G.M. Zhao, and K.A. Müller (Honorarprofessor)

10.1 Introduction

Over the past year we have continued and extended our investigations of the magnetic properties of high-temperature superconductors and related magnetic systems. In order to achieve this goal we have used a combination of muon spin rotation (μSR), neutron scattering, electron paramagnetic resonance (EPR), together with bulk SQUID and torque magnetometry measurements, and thermal expansion measurements.

In addition to our well established activities at the muon beams of PSI (Paul Scherrer Institute) and RAL (Rutherford Appleton Laboratory), we have over the past few years become increasingly involved in the investigation of vortex lattices using neutron scattering techniques. Up to now, these studies have been carried out at the ILL (Institut Laue Langevin), but with the advent of the neutron spallation source SINQ at PSI, we hope to carry out some of our future neutron work there (see Sec 10.2).

In order to complete our recent development of microscopic torquemeters (see also Annual Report 96/97), we designed a larger torque sensor for measuring with an optimized sensitivity millimeter size samples (see Sec 10.3.1).

During the last year torque magnetization measurements on $HgBa_2CuO_{4+\delta}$ single crystals with different oxygen doping δ were performed in order to reveal the doping dependence of the effective mass anisotropy $\gamma = \sqrt{m_c^*/m_{ab}^*}$, and of the in-plane penetration depth λ_{ab}. The observed monotonic increase of γ with decreasing δ is well described by a (bi)polaronic model of high-T_c superconductivity (see Sec. 10.3.2).

Electron Paramagnetic Resonance (EPR) is a powerful tool in solid state physics, which allows to study crystal electric fields, electron-phonon interactions, static and dynamic magnetic correlations on a *microscopic* level. EPR is a contactless method, thus the samples of any form (powder, pellet, single crystal, thin film) can be measured. Due to the extreme sensitivity of EPR, only a tiny amount of material is necessary. Our research interest during the last year was mainly concerned with hole-doped quasi-1D copper-oxygen chain systems (see Sec.10.4.1) and high-T_c cuprates (see Sec.10.4.2).

We have continued our studies of oxygen-isotope effects in the giant magnetoresistance manganites $La_{1-x}Me_xMnO_3$ (Me = Ca, Sr, and Ba) by means of magnetization and resistivity measurements, as well as measurements of the thermal expansion coefficient (see Annual Report 96/97). As a result of this study, we discovered a novel metal-insulator transion induced by oxygen isotope exchange in $(La_{0.5}Nd_{0.5})_{0.67}Ca_{0.33}MnO_3$ (see Sec. 10.5.1). Furthermore, we have completed our study of the oxygen-isotope effect on the in-plane penetration depth in the cuprate superconductor $La_{2-x}Sr_xCuO_4$. The observed isotope effect indicates that polaronic charge carriers exist and condense into supercarriers in this cuprate superconductor (see Sec. 10.5.2).

There have been numerous reports in the literature about possible unconventional thermodynamic phases of the vortex matter in ceramic and non-oxide superconductors. The small number of relevant degrees of freedom in vortex-related systems (due to the small number of vortices) represents an attractive challenge for small-signal calorimetry. We are currently building novel thermal probes, not only with the aim to further increase the existing sensi-

tivity for testing bulk thermal properties of such solids, but also to thermally characterize thin-film samples and surfaces (see Sec. 10.6).

This work was done in collaboration with scientists from ETH Zürich (K. Conder, J. Karpinski, H. Schwer, E.M. Kopnin, R. Molinski, and G.I. Meijer), IBM Rüschlikon Laboratory (C. Rossel, H. Rothuizen, J. Brugger, and P. Vettiger), University of Birmingham (E.M. Forgan, S.H. Lloyd, W.J. Nuttall, and P.G. Kealey), University of St. Andrews (S.L. Lee and C. Ager), Institut Max von Laue-Paul Langevin, Grenoble (R. Cubitt), University of Oxford (S.J. Blundell), RIKEN-RAL (F.L. Pratt), University of Warwick (D. McK. Paul), Oak Ridge National Laboratory (M. Yethiraj), Tohoku University (T. Sasaki), Université Paris-Sud (S.T. Johnson), and University of Zaragoza (M.R. Ibarra and J.M. De Teresa).

10.2 Investigating vortex matter at central facilities

The behaviour of magnetic flux in superconductors is of great scientific and technological interest. Pinning the notoriously flexible vortex lines in highly anisotropic superconductors, such as the cuprate high-T_c's is of fundamental importance to any technical application, as movement of flux lines dissipates energy, which presents an unwanted energy-loss. However, on more scientific grounds, the high anisotropy of the cuprate superconductors makes them very interesting systems in the realm of 'soft condensed matter'. The basic building blocks of this type of 'matter', which consist of magnetic flux, are very well understood, such that only the basic interactions between the constituent are decisive for the structures one observes. Studying prime examples of extremely anisotropic superconductors, such as the high-T_c BSCCO and the organic superconductor ET-Cu, we gain an understanding of the generic behaviour and interactions in these systems. Below we will give a small selection of our current work, the details of which can be found in the references.

Muon spin rotation (μSR) and neutron small angle scattering (SANS) present complementary ways of attacking these questions. Both present a microscopic measurement of the bulk of the material, but whereas the muon is a probe of the local fields, neutrons are susceptible to long range modulations in the field distribution. Therefore the fluctuations in the vortex lattice are readily observed with μSR [1], while its overall structure can be easily resolved by SANS [2].

In our investigation of the vortex behaviour in the extremely anisotropic superconductor BSCCO, this complementarity has helped us to clarify the interplay between the static disordering of flux lines along their length induced by point pinning sites, with the effects of thermal fluctuations. In highly anisotropic superconducors, the flux lines can viewed as being composed of two dimensional (2D) entities called 'pancake' vortices. With increasing field, a three dimensional vortex line will decompose into these pancake vortices. We have already observed this effect in BSCCO [3, 4] and also in the organic superconductor ET-Cu [5]. We have this year also studied the angular dependence of this effect [6], which together with the dependence upon doping gives valuable insight on the nature of the interlayer coupling between these pancake vortices [4, 6]. Therefore, at high fields, the vortex structure in highly anisotropic superconductors is disordered along the field direction, due to pinning of individual pancake vortices by e.g. oxygen vacancies. This leads to the loss of scattered neutron intensity above this crossover field [7], as the field contrast is strongly reduced, whereas μSR observes a change in the shape of the field distribution. In a narrow region of the phase diagram just around this crossover field, these static disordering of flux lines due to pinning and the dynamic disorder due to thermal fluctuations compete in such a way to result in increased ordering of the flux lattice along the field. At fields just above the crossover field, we have now observed the reappearence of Bragg scattering above a certain

temperature T^1, corresponding to a depinning of vortices [8]. As the thermal excitations are strong enough to depin the individual pancake vortices from their pinning sites, the remaining interlayer coupling leads to an ordering of the vortex lines along the field. This can be seen in Fig. 10.1, where we show the temperature dependence of the scattered neutron inten-

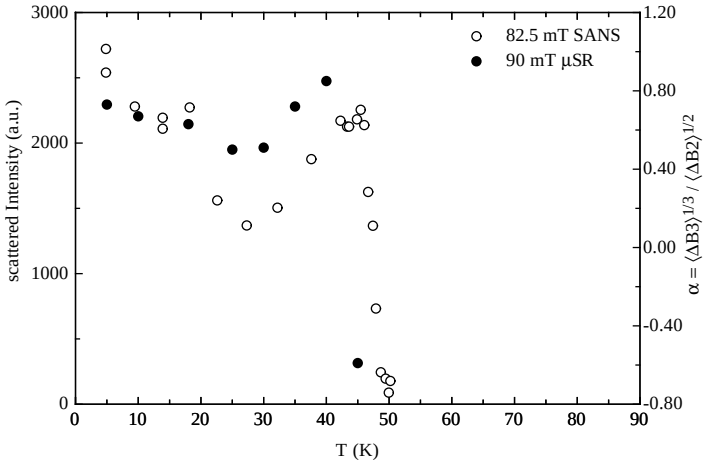

Figure 10.1: *The temperature dependence of the scattered neutron intensity at 82.5 mT showing an upturn at ∼ 25 K. This is interpreted as a depinning of pancake vortices (see text). For comparison, the temperature dependence of the lineshape asymmetry α from μSR at 90 mT, is given. The data show an upturn at similar temperatures, indicating increased c-axis correlation in both cases, before the melting transition at higher temperatures.*

sity in a Bragg peak at a field of 82.5 mT. Fig. 10.1 also shows results obtained with μSR, where we have plotted the temperature dependence of the lineshape asymmetry parameter $\alpha = \langle \Delta B^3 \rangle^{1/3} / \langle \Delta B^2 \rangle^{1/2}$. This parameter is positve for lineshapes with a tail extending to fields higher than the average. For a well ordered flux lattice of straight vortex lines, this is expected to be ~ 1.2 in our experimental setup. It can be seen that the lineshape becomes more asymmetric, corresponding to an ordered lattice, at the same point where we observe increased Bragg-scattering. At higher temperatures, the diffraction pattern disappears again, because of the melting of the vortex lattice. We are thus also able to observe the melting of the vortex lattice above the crossover field, which is in contradiction to recent magnetisation experiments [10], where a jump in the reversible magnetisation is interpreted as the melting of the lattice.

We also used the complementarity of neutrons and muons in a study of the differences between type-I and type-II superconductors. With a suitable sample geometry, a type-I superconductor enters the intermediate state, where superconducting regions in the Meissner state coexist with normal-conducting regions with an internal field corresponding to the thermodynamical critical field. This is due to demagnetising effects leading to fields higher than the applied at the sample edges. This effect can be easily seen with μSR, where the local fields are measured. However, the structure of the coexisting domains is unaccesible to the muons, as they only measure locally. SANS in contrast is insensitve to the field values in the normal regions, however the domain structures produce a field contrast, which gives rise to scattering. Thus we can map out the temperature dependence of B_c from μSR, as well as that of the radius of gyration of the domain structures from SANS. By suitably choosing the doping level in PbBi alloys, the Ginzburg-Landau parameter κ, decisive for the overall behaviour, takes on a value for a transition between type-I and type-II superconducing behaviour to be observable. Using the complementarities of SANS and μSR, it is also possible to gain a

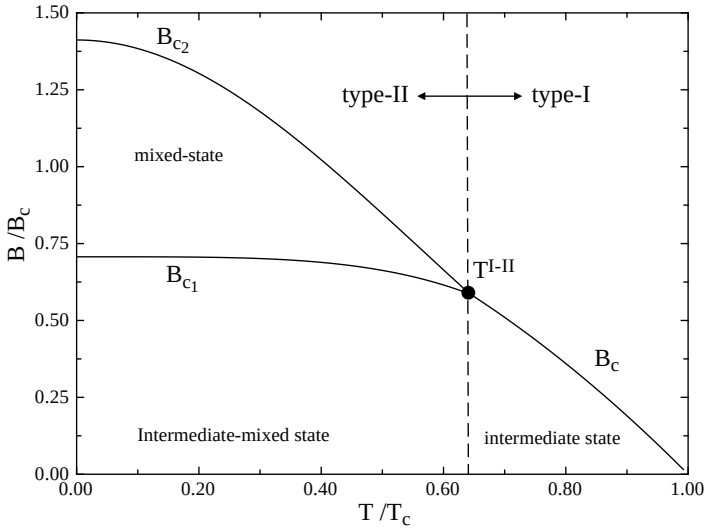

Figure 10.2: *The thermodynamic phase diagram of a superconductor with κ_0 =1. The different transition lines corresponding to type-I and type-II superconducting behaviour meet in a multicritical point at a temperature T^{I-II}, where the order of the transition changes from first to second order. The phase lines are calculated from the two-fluid model.*

full understanding of the magnetic field structures in the sample. We have even observed a coexistence of type-I and type-II superconducting behaviour for the first time, as could be expected for such a multicritical point in the B-T phase diagram. The thermodynamic phase diagram in accord with these investigations [11] can be calculated from the two-fluid model of superconductivity and is shown in Fig. 10.2.

10.3 Torque magnetization measurements on high-T_c superconductors

10.3.1 Design of a new generation of capacitance sensors for torque magnetometry

The principle of torque magnetometry is to measure magnetic moments of anisotropic magnetic or superconducting samples. The design of a sensor is optimized to detect with a high sensitivity the torque given by $\vec{\tau} = \vec{m} \times \vec{B}$, where $\vec{m}$ is the magnetic moment of the sample and $\vec{B}$ is the homogeneous external magnetic field.
We already developed ultra-sensitive torquemeters based on microscopic silicon cantilevers with piezoresistive readout and a resolution of about 10^{-14} Nm, depending on the operating mode [12] (see also Annual Report 96/97). This sensitivity is sufficient for most applications. The dimensions of these sensors are in the micrometer range in order to better avoid the effects of external mechanical perturbations and to reach a higher sensitivity. These sensors are very well suited for measuring the magnetic moment of very small samples ($< 100\mu$m). However, for larger samples other measurement techniques are required, such as capacitance levers [13, 14] or macroscopic piezoresistive levers [15]. The sensitivity of these devices is always limited by the external mechanical noise and/or by a non-negligible magnetic background of the lever itself.

In collaboration with IBM Rüschlikon we designed a novel silicon torque sensor with capacitive readout and optimal geometry [16]. The advantage of single-crystal silicon, compared to other materials, is its very low magnetic background. The capacitive readout is perfectly suited for high field applications. Furthermore, in order to reach a high mechanical stability,

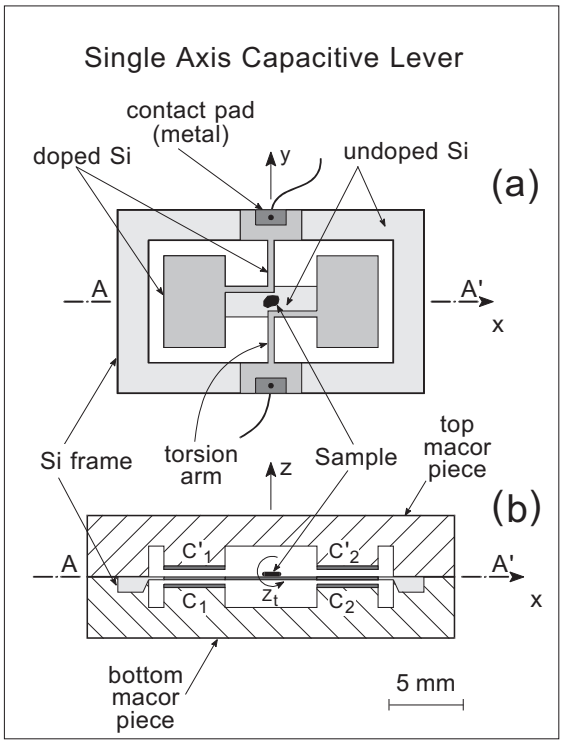

Figure 10.3: *(a) Schematic top view of the torsion lever with its frame. (b) Side view of the lever mounted in the ceramic (macor) support.*

the sensor geometry was chosen to be totally symmetric (see Fig. 10.3a). The flexible torsion lever with its silicon frame is mounted into a ceramic (macor) support which contains two pairs of counterelectrodes. A thin gold layer is patterned on the ceramic surface for the electrical contacts. The torsion lever provides the central electrode, which is positionned in the space between the two pairs of counterelectrodes, forming the capacities C_1, C_1', C_2 and C_2' (see Fig. 10.3b). Any change in position of the lever produces a capacitance variation measured always in a differential mode. Different configurations of electrodes can be chosen, depending on the application. With a specific electronic capacitance bridge, developed by our group, a torque resolution of about $6 \cdot 10^{-13}$ Nm can be achieved.
This novel torquemeter is a powerful tool, not only for further investigations of high-T_c superconductors, but also to study other systems, such as antiferromagnetic compounds [17]. By means of a permanent calibrated magnetic moment (for instance a small piece of Fe_2O_3 audio tape) we were able to calibrate the torquemeter very accurately. On the other hand, with a strong permanent magnet, i.e. NdFeB, the sensor acts as a very sensitive gaussmeter with a typical resolution better than 10 nT.

10.3.2 Doping dependence of superconducting properties in $HgBa_2CuO_{4+\delta}$ single crystals.

High-T_c superconductors show a strong doping dependence of their superconducting properties. Upon increasing the charge carrier concentration, starting from the insulating or semiconducting mother compounds, the critical temperatur T_c increases in the underdoped regime, reaches a maximum for optimal doping and decreases again in the overdoped regime. In the underdoped regime, T_c was found to show a parabolic dependence on the inverse

square of the in-plane penetration depth $\lambda_{ab}^{-2}(0) \propto n_s/m_{ab}^*$, where n_s is the density and m_{ab}^* the effective in-plane mass of the superconducting charge carriers [18]. A monotonic increase of the effective mass anisotropy $\gamma = \sqrt{m_c^*/m_{ab}^*}$ with decreasing doping was observed in different experiments using torque magnetometry and other techniques in $YBa_2Cu_3O_{7-\delta}$ [19] and $La_{2-x}Sr_xCuO_4$ [20]. In order to clarify these universal trends, we performed torque measurements on $HgBa_2CuO_{4+\delta}$ single crystals with different oxygen doping δ.

The single crystals were grown using a high pressure growth technique [21]. They were annealed in an Ar or an O_2 atmosphere in order to change δ. We were able to vary δ between 0.05 and 0.11. The superconducting transitions were rather sharp giving evidence for a quite homogeneous oxygen distribution within the samples.

In the layered high-T_c compounds the magnetic moment $\vec{m}$ points preferentally along the c-axis and experiences a magnetic torque $\vec{\tau} = \vec{m} \times \vec{B}_a$ in an applied magnetic field $\vec{B}_a$. In a rotation measurement this magnetic torque is recorded as a function of the angle θ between $\vec{B}_a$ and the ab-plane of the sample. Field dependent measurements at a fixed angle can be performed as well. From the Meissner slope observed at low fields the torque meter can be calibrated.

The $HgBa_2CuO_{4+\delta}$ micro crystals (masses between 1 and 9 μg) were mounted on a small piezoresistive cantilever [22]. Rotation measurements were performed at different temperatures in an applied field $B_a = 1.4$ T. They were analysed using a 3D anisotropic London model [23], revealing the effective mass anisotropy γ, the in-plane penetration depth λ_{ab}, and the upper critical field along the c-axis B_{c2}^c at a given temperature. From the temperature dependence of λ_{ab} and B_{c2}^c their low temperature values were extrapolated. Fig. 10.4a

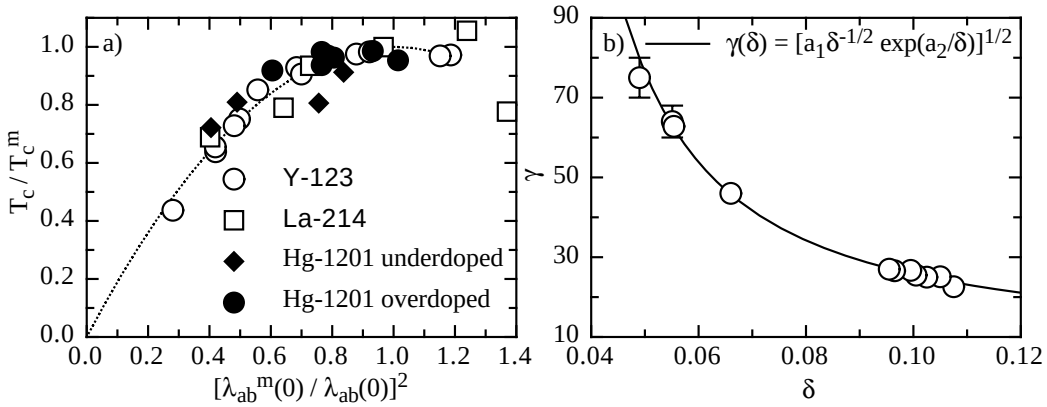

Figure 10.4: *a) $\overline{T_c}$ as a function of $1/\overline{\lambda}_{ab}^2$ for our samples together with earlier reported data (from Ref. [18]). The dotted line represents the parabolic ansatz $\overline{T}_c = 2/\overline{\lambda}_{ab}^2(1-1/(2\overline{\lambda}_{ab}^2))$. b) Effective mass anisotropy as a function of doping δ. The solid line is based on a (bi)polaronic model of high-T_c superconductivity (see text).*

shows the reduced critical temperature $\overline{T}_c = T_c/T_c^m$ as a function of the inverse square of the reduced penetration depth $\overline{\lambda}_{ab} = \lambda_{ab}(0)/\lambda_{ab}^m(0)$ (T_c^m and $\lambda_{ab}^m(0)$ are the values at optimal doping) together with earlier reported data from [18] (Uemura plot). The data in the underdoped regime are well described by the parabolic ansatz $\overline{T}_c = 2/\overline{\lambda}_{ab}^2(1-1/(2\overline{\lambda}_{ab}^2))$ [18]. The data for our overdoped samples seem to fall on the same branch, pointing towards an increase of $\lambda_{ab}(0)$ in the overdoped regime with increasing doping. This increase cannot be an artifact due to an overestimation of the superconducting volume, since our calibration of $\lambda_{ab}(0)$ does not depend on the sample volume.

As shown in Fig. 10.4b, γ is monotonically increasing with decreasing δ over the whole

doping regime investigated. An explanation for this increase can be given by a (bi)polaronic model of superconductivity by Alexandrov and Mott [24] ,which is supported by experimental evidence for polaronic superconducting carriers in the $La_{2-x}Sr_xCuO_4$ system [25]. Within this model γ mainly depends on the (bi)polaronic binding energy which is predicted by theory to be proportional to $1/\delta$ [26]. With this the effective mass anisotropy is given by $\gamma(\delta) = [a_1\delta^{-1/2}\exp(a_2/\delta)]^{1/2}$. This doping dependence is shown as a solid line in Fig. 10.4b. Since high-quality $HgBa_2CuO_{4+\delta}$ single crystals are very small, there is hardly any other experimental technique to investigate them. Therefore several physical parameters entering in a_1 and a_2 are unknown for the $HgBa_2CuO_{4+\delta}$ system. However, the two values a_1 and a_2 obtained from the fit are in a reasonable range.

The increase of the (bi)polaronic binding energy with decreasing doping also leads to an increase of the effective mass of the normal state charge carriers. This might by an explanation for the observed smooth crossover from metallic to insulating or semiconducting behavior upon reducing the charge carrier concentration [27]. Furthermore this (bi)polaronic model also provides a simple explanation for the linear dependence of γ on the number n of CuO_2 layers in the $HgBa_2Ca_{n-1}Cu_nO_{2n+2+\delta}$ family [28].

10.4 EPR study of cuprates

10.4.1 EPR study of low-dimensional cuprates

Although the study of one-dimensional (1D) magnetism has a very long history, the recent discovery of various quasi-1D quantum antiferromagnets and the progress in analytic and numerical theories have significantly advanced this field [29].

Recently, the novel 1D cuprate $Sr_{0.73}CuO_2$ was synthesized under high oxygen pressure at ETH Zürich [30]. This compound is made of edge sharing CuO chains and the average valency of copper is +2.56. Thus, $Sr_{0.73}CuO_2$ provides an unique possibility to study the properties of hole doped copper-oxygen chains. Perhaps the most peculiar feature of $Sr_{0.72}CuO_2$ is a sudden jump in the magnetization observed below ~10 K, indicating a ferromagnetic-like magnetic transition [30]. We performed EPR measurements in order to study the magnetic properties of $Sr_{0.73}CuO_2$ on a microscopic level [31].

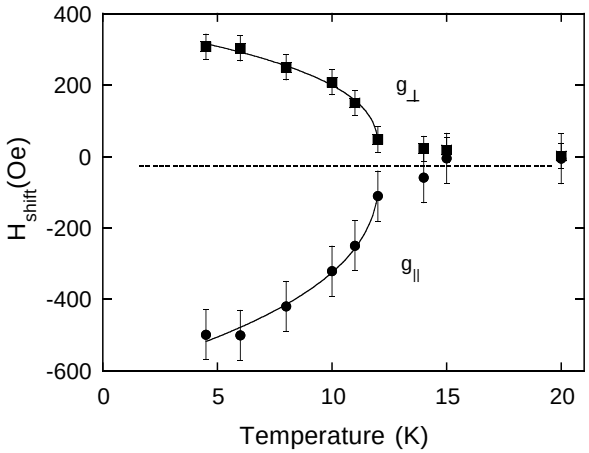

Figure 10.5: *Temperature dependencies of the position of the extra peaks relative to the $g_{||}$ and $g_\perp$ components. The solid lines correspond to a power-law fit (1-T/T_c)$^\beta$ with T_c=12.05(5) K and β=0.34(5).*

The most important results can be summarized as follows. In the paramagnetic regime

the EPR signal corresponds to powder averaged spectra with $g_{||}$=2.21(1) and $g_{\perp}$=2.015(5), which is characteristic for Cu^{2+} ions in an axial crystal electric field. Below ~12 K, two new lines split from the main EPR line. With decreasing temperature one line splits from the $g_{||}$ peak and shifts to lower fields, while another line splits from the $g_{\perp}$ peak and shifts to higher fields. The splitting of the EPR line demonstrates that below Tc a well defined internal field develops in $Sr_{0.73}CuO_2$ due to 3D long-range magnetic order. The temperature dependence of the EPR line splitting, which represents a measure of the internal magnetic field present in the sample, is shown in Fig. 10.5. The solid line corresponds to a power-law fit $(1\text{-}T/T_c)^{\beta}$ with T_c=12.05(5) K and β=0.34(5). Our preliminary zero-field μSR measurements on the same sample also confirmed a sharp magnetic transition below Tc [32].

Thus magnetization, EPR, and μSR measurements provide evidence that below T_c ~12 K a long-range magnetic order with a small spontaneous ferromagnetic moment $M_s = 3.2(2) \cdot 10^{-3}\mu_B$/Cu occurs in $Sr_{0.73}CuO_2$ [31]. The observation of magnetic order is very unusual in view of the high hole doping of the copper-oxygen chains, where each hole renders a CuO unit to become nonmagnetic due to the Zhang-Rice singlet formation. Further experimental work is necessary to clarify the microscopic mechanism of this unusual magnetic transition.

10.4.2 EPR study of high-T_c cuprates

There is increasing evidence that inhomogeneous distribution of charge carriers is a common, if not universal, feature of cuprates and that ordering of charge into modulated structures may play a key role in high-temperature superconductivity [33]. However, neither the exact nature of these inhomogeneities nor their influence on the electronic properties are well understood. EPR of magnetic rare earth ions in high-T_c cuprates is a highly sensitive local method, which allows to study spatial variation of structural and electronic properties on a microscopic level [34]. We performed EPR measurements of Yb^{3+} doped to $YBa_2Cu_4O_8$ (Y124) with 1% of the Y replaced by Yb^{3+}. Structurally, Y124 is unique in the sense that it has fixed oxygen stoichiometry with saturated double CuO chains, providing a test case free of ambiguities due to oxygen disorder and nonstoichiometry.

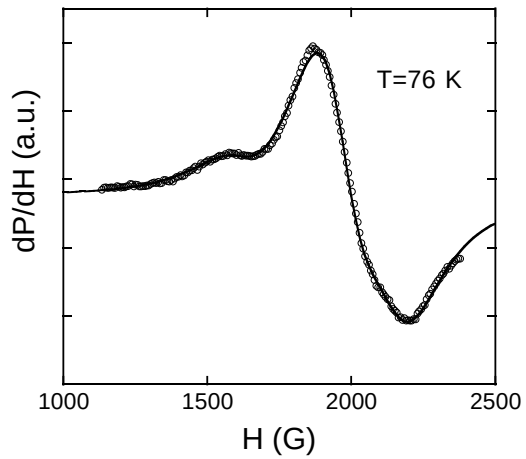

Figure 10.6: *Yb^{3+} EPR spectra of $Y_{0.99}Yb_{0.01}Ba_2Cu_4O_8$ at 76 K. The solid line is a fit using the sum of three Lorentzians with different g-factors.*

Fig. 10.6 shows EPR spectra of Yb^{3+} at 76 K. From Fig. 10.6 one can see that the Yb^{3+} spectra have an asymmetric lineshape with shoulders at the low and high field side of the central line. We found that the spectra can be well described by a sum of three Lorentzian

lines of the same linewidth, but with different g-factors. This very likely indicates three different surroundings of Yb^{3+} in Y124 due to crystal electric field variation. It is worth noting that inelastic neutron scattering measurements in $ErBa_2Cu_3O_x$ samples also revealed three different types of clusters in the CuO_2 planes [35]. We plan to extend our measurements to higher frequencies and on magnetically oriented samples in order to clarify this interesting question in more detail.

10.5 Studies of oxygen isotope effects

10.5.1 Oxygen isotope effects in the manganites

The manganese-based perovskites $La_{1-x}Me_xMnO_3$ (Me = Ca, Sr, and Ba) have recently been the subject of intensive investigations because of the discovery of the colossal magnetoresistance (CMR) effect. The manganites exhibit a broad range of electronic and magnetic phases, ranging from low-resistivity ferromagnetic metals to high-resistivity insulators, which are extremely sensitive to variation of composition, temperature and pressure. Such sensitivity also extends to the oxygen isotope exchange: replacing ^{16}O with ^{18}O in $La_{0.8}Ca_{0.2}MnO_{3+y}$ [36], produces an unusually large change in the magnetic properties (a 21 K decrease in the Curie temperature). There are also large oxygen isotope effects on other physical properties such as the thermal-expansion coefficient jump at T_C [37] and the EPR intensity [38]. These isotope-effect experiments provide crucial evidence for the existence of small polarons (JT polarons [39]) in these JT perovskites, and place important constraints on the microscopic mechanism of the colossal magnetoresistance effect.

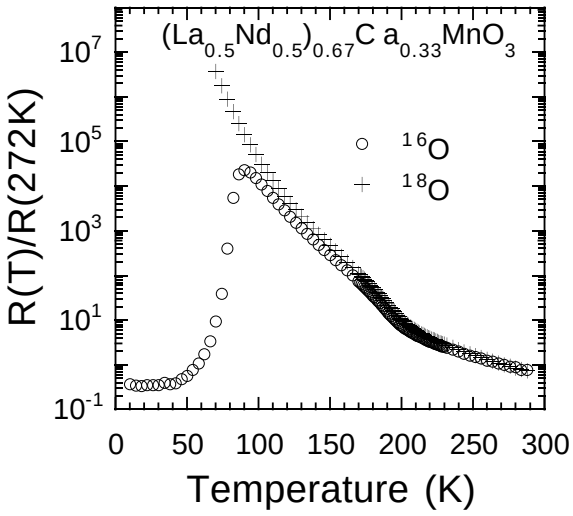

Figure 10.7: *The temperature dependence of the resistivity (normalized to the resistivity at 272 K) for the ^{16}O and ^{18}O samples of $(La_{0.5}Nd_{0.5})_{0.67}Ca_{0.33}MnO_3$.*

We have extended our studies of the oxygen-isotope effects in some chosen manganites such as $(La_{0.5}Nd_{0.5})_{0.67}Ca_{0.33}MnO_3$. This material has a smaller ionic radius at A-site $<r_A>$ and much lower T_C than $La_{0.67}Ca_{0.33}MnO_3$. This compound undergoes an insulator-metal transition as it is cooled below $\sim$ 100 K. But it is very surprising that after substituting ^{18}O for ^{16}O, the compound remains in an insulating state down to 5 K (see Fig. 10.7). Note that at low temperatures the resistivity for the ^{18}O samples is too high to measure. This novel isotope effect has never been expected by any conventional theory in condensed matter physics. By considering the presence of both lattice and magnetic polarons in this material,

we might be able to explain this experimental result [40]. Recently, this novel insulator-metal transition induced by oxygen isotope exchange was confirmed by a Russian group [41].

To understand the origin of this novel isotope effect, we have also done neutron scattering, magnetostriction and thermal-expansion experiments on this material with both ^{16}O and ^{18}O isotopes. We show that the ^{18}O sample exhibits an antiferromagnetic, charge ordered, and insulating ground state, while the ^{16}O sample has a phase separation: a ferromagnetic state in some regimes and an antiferromagnetic state in other regimes. Upon replacing ^{16}O with ^{18}O, the ferromagnetic regimes transform into the antiferromagnetic regimes. All these results consistently suggest that charge carriers in manganites are strongly coupled to the local JT distortions and magnetic moments, so that small polarons (quasiparticles dressed by both the local JT distortions and spin polarizations) can be formed. This is crucial for the understanding of the physics in the colossal magnetoresistive manganites.

10.5.2 Oxygen isotope effect in $La_{2-x}Sr_xCuO_4$

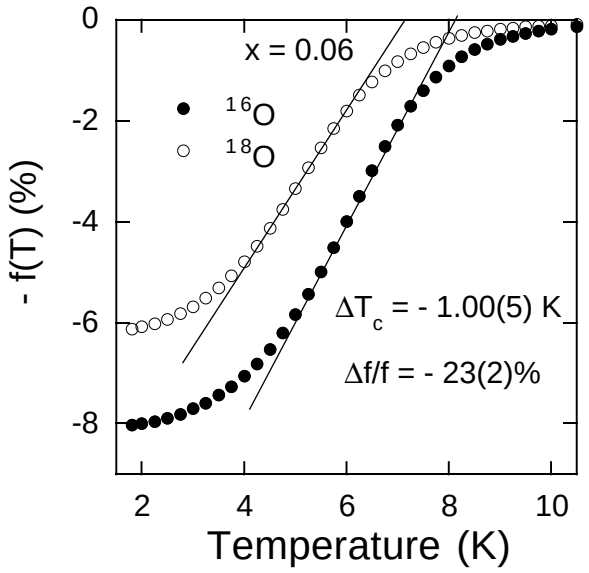

Figure 10.8: *Temperature dependence of the Meissner effect for ^{16}O and ^{18}O samples of $La_{2-x}Sr_xCuO_4$ with $x = 0.06$.*

The microscopic pairing mechanism for high-T_c superconductivity (HTSC) is one of the most controversial issues in condensed matter physics. Eleven years after the discovery of the high-T_c cuprate superconductors by Bednorz and Müller [42], there have been no microscopic theories that can describe the physics of high-T_c superconductors completely and unambiguously. The high values of T_c (>30 K) in the cuprate superconductors were not expected from a conventional phonon-mediated pairing mechanism, so many non-phonon mediated mechanisms have been proposed. A great number of experimental results appear to support some of these unconventional mechanisms. On the other hand, there is increasing experimental evidence that a strong electron-phonon coupling is present in cuprates. Such strong electron-phonon interaction may lead to the formation of polaronic charge carriers. Still, direct evidence that polarons exist in the copper oxides has been lacking, although some indirect evidence comes from their recent discovery [36] in the structurally similar but nonsuperconducting manganite $La_{1-x}Ca_xMnO_3$.

To show that polaronic charge carriers exist and condense into supercarriers, one has to

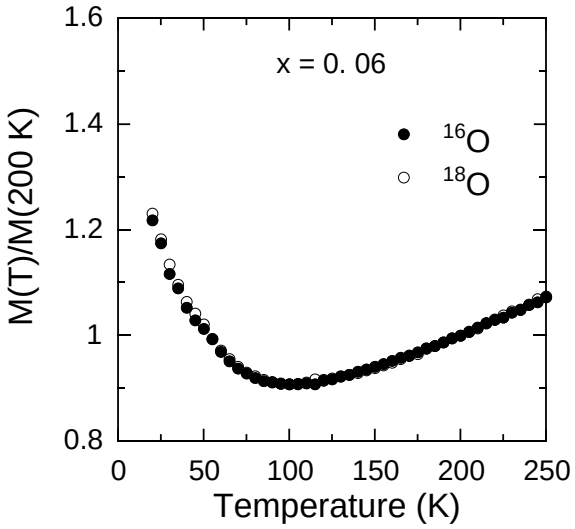

Figure 10.9: *Normal-state susceptibility for ^{16}O and ^{18}O samples of $x = 0.06$. From the doping dependence of the normat-state susceptibility, we estimate that the difference in the hole concentrations of the two isotope samples must be less than 0.0002 per cell.*

demonstrate that the effective supercarrier mass depends strongly on the ionic mass M. This is because the effective mass of polarons depends strongly on M (Ref. [24]). When the polarons condense into supercarriers by whatever pairing mechanism, the effective supercarrier mass will also depend on M. We have performed magnetization measurement on samples of the one-layer cuprates $La_{2-x}Sr_xCuO_4$ as a function of x ($0.06 \leq x \leq 0.15$). From magnetization measurements on the fine-grained and decoupled samples in the Meissner state, we find substantial oxygen-isotope effects on both the penetration depth $\lambda(0)$ and T_c (see Fig. 10.8) [25]. From normal-state susceptibility measurements, we are able to show that there is a negligible oxygen-isotope effect on the carrier density n (see Fig. 10.9). The combined results strongly suggest that there is an oxygen-isotope effect on the effective supercarrier mass m^{**}, which is huge for $x = 0.06$, and reduced to a smaller value for $x = 0.15$. From the normal-state susceptibility, we have also determined the normal-state gap as a function of x on the basis of small (bi)polaron theory [26]. We discuss the isotope effects, supercarrier mass anisotropy, normal-state gap, in-plane penetration depth and mid-IR spectra for $x \leq 0.09$ on the basis of the small polaron theory of superconductivity. We find that the agreement between the calculated and experimental results is excellent without any adjustable parameters.

10.6 Detection of small thermal effects in basic and applied condensed matter physics

An important source of progress in experimental condensed-matter physics is the development of new measuring techniques with very high accuracy. The application of high-precision techniques already allowed for the observation of very small thermodynamic effects such as phase transitions of the vortex matter in cuprate superconductors[43, 44, 45], that finally led to exciting new insights into the fundamentals of material properties limiting current transport. These innovative experimental methods shall be extended at our institute, not only with the aim to further increase the sensitivity for testing bulk thermal properties of solids, but also to develop novel tools to thermally characterise thin-film samples, surfaces, and small artificial structures.

We intend to study the possibility of measuring thermal effects locally, e.g. on single crystals or thin films. There are already several apparatuses described in the literature that produce rough thermal images of solid-state surfaces at or above room temperature [46]. A logical improvement is to detect locally small changes in temperature as a function of time (the knowledge of which is necessary to calculate a specific heat), and to finally place such an experiment into a cryostat. Natural applications of such a device are the (notably non-destructive) imaging of thermal properties of materials showing domains or a coexistence of thermodynamic phases, the measurement of the thermal conductivity on thin-film samples (e.g., thermoelectric materials), and the thermal imaging of artificial structures like microelectronic control elements, sensors, and circuits under operation, at or below room temperature.

References

[1] S.L. Lee *et al.*, Phys. Rev. Lett. **75**, 922 (1995).

[2] D.McK. Paul *et al.*, Phys. Rev. Lett. **80**, 1517 (1998).

[3] S.L. Lee *et al.*, Phys. Rev. Lett. **71**, 3862 (1993).

[4] C.M. Aegerter *et al.*, Phys. Rev. B **54**, R15661 (1996).

[5] S.L. Lee *et al.*, Phys. Rev. Lett. **79**, 1563 (1997).

[6] C.M. Aegerter *et al.*, Phys. Rev. B **57**, 1253 (1998).

[7] R. Cubitt *et al.*, Nature **365**, 407 (1993).

[8] S.H. Lloyd *et al.*, submitted to Phys. Rev. Lett. (1998).

[9] S.L. Lee *et al.* Phys. Rev. B **55**, 5666 (1997).

[10] B. Khaykovich *et al.* Phys. Rev. Lett. **76**, 2555 (1996).

[11] C.M. Aegerter *et al.*, submitted to Phys. Rev. B (1998).

[12] M. Willemin *et al.*, J. Appl. Phys. **83**, 1163 (1998).

[13] R. Griessen *et al.*, Phys. Rev. B **16**, 4385 (1977).

[14] H. Schnack, PhD Thesis, *Vrije Universiteit*, Amsterdam, (1995).

[15] Physics Today **51**, 14 (1998).

[16] C. Rossel and M. Willemin, IBM Technical Disclosure Bulletin **40**, 119 (1997).

[17] G.I. Meijer *et al.*, to appear in Europhys. Lett. (1998).

[18] T. Schneider and H. Keller, Phys. Rev. Lett. **69**, 3374 (1993); Int. J. Mod. Phys. **8**, 487 (1993).

[19] T. R. Chien *et al.*, Physica C **229**, 273 (1994).

[20] M. Suzuki and M. Hikita, Phys. Rev. B **44**, 249 (1991).

[21] J. Karpinski *et al.*, Physica C **234**, 10 (1994).

[22] C. Rossel *et al.*, J. Appl. Phys. **79**, 8166 (1996).

[23] V.G. Kogan, M.M. Fang, and S. Mitra, Phys. Rev. B **38**, 11958 (1988).

[24] A.S. Alexandrov and N.F. Mott, Int. J. Mod. Phys. **8**, 2075 (1994).

[25] G.M. Zhao *et al.*, Nature **385**, 236 (1997).

[26] A.S. Alexandrov, V.V. Kabanov, and N.F. Mott, Phys. Rev. Lett. **77**, 4796 (1996).

[27] H. Takagi *et al.*, Phys. Rev. B **40**, 2254 (1989).

[28] J. Hofer, unpublished results.

[29] E. Dagotto and T.M. Rice, Science **271**, 618 (1996).

[30] J. Karpinski *et al.*, Physica C **274**, 99 (1997).

[31] A. Shengelaya *et al.*, Phys. Rev. Lett. (1998) in press.

[32] A. Shengelaya *et al.*, (unpublished).

[33] See, for instance, *Phase separation in Cuprate Superconductors*, edited by K.A. Müller and G. Benedek (World Scientific, Singapore, 1993).

[34] A. Jánossy *et al.*, Physica C **171**, 457 (1990).

[35] J. Mesot *et al.*, Phys. Rev. Lett. **70**, 865 (1993).

[36] G.M. Zhao *et al.*, Nature **381**, 676 (1996).

[37] G.M. Zhao, M.B. Hunt and H. Keller, Phys. Rev. Lett. **78**, 955 (1997).

[38] A. Shengelaya *et al.*, Phys. Rev. Lett. **77**, 5296 (1996).

[39] K.-H, Höck, H. Nickisch, and H. Thomas, Helv. Phys. Acta. **56**, 237 (1983).

[40] G.M. Zhao *et al.*, Solid State Commun. **104**, 57 (1997).

[41] N.A. Babushkina *et al.*, Nature **391**, 159 (1998).

[42] J.G. Bednorz and K.A. Müller, Z. Phys. B **64**, 189 (1986)

[43] A. Schilling and O. Jeandupeux, Phys. Rev. B **52**, 9714 (1995).

[44] A. Schilling *et al.*, Nature **382**, 791 (1996).

[45] A. Schilling *et al.*, Phys. Rev. Lett. **78**, 4833 (1997).

[46] J. Kölzer *et al.*, Microelectronic Engineering **31**, 251 (1996).

11 Surface Physics

T. Greber, R. Holzner, E. Wetli, S. Dangel, T. J. Kreutz, H. Neff,
H. Schmid, P. Schwaller, J. Wider, W. Auwärter, F. Baumberger, S. Berner
M. Hoesch, A. Schneider, W. Deichmann, J. Osterwalder

In the surface physics laboratory we study well-defined surfaces of solid materials as well as adsorbed atomic and molecular monolayers and ultrathin films, prepared under ultrahigh-vacuum (UHV) conditions. In order to obtain detailed information on the geometric arrangement of the atoms within the first few monolayers of the surface we apply predominantly electron-based techniques such as X-ray photoelectron diffraction (XPD), medium-energy electron diffraction (MEED), low-energy electron diffraction (LEED), and most recently also scanning-tunneling and atomic force microscopy (STM/AFM - see below). A time-resolved MEED experiment is being developed with a temporal resolution in the picosecond range. Based on a new experimental geometry for XPD, where photoelectron diffraction effects are measured near a node of the photoexcited electron wave, the concept of photoelectron holography is tested as to whether it could finally fulfill its promises as a direct structural technique on surfaces.

Angle-resolved UV photoelectron spectroscopy (ARUPS) gives access to the electronic band structure of solids and surfaces. Specifically, our experimental setup permits us to directly map sections through the Fermi surfaces of such systems, which represent the electronic degrees of freedom relevant for transport properties, magnetic interactions and phase transitions. We could also extend the measuring range of photoemission above the Fermi level to observe thermally excited electrons within the band structure. An important asset of all these experiments is that the same probe (photoemission) gives structural, electronic and magnetic information, and we can therefore study the interplay between these different degrees of freedom on the same sample.

In a common project with H. Keller we were able to purchase a combined STM/AFM system (Park Scientific) with one measuring head in UHV complementing our electron-scattering based techniques and one head working at ambient pressure serving as a general purpose surface characterization tool for the Physics department and other interested departments. The UHV head is currently being mounted in a dedicated chamber as a stand-alone experiment. After extensive tests this chamber will be connected to our photoelectron spectrometer. The ambient head has found frequent use within our own group and by a group from the Physical Chemistry department (R. Timm, P. Willmott, J. R. Huber).

With this same group we have also had a fruitful collaboration in which they were able to profit from our unique instrumentation for efficiently measuring XPD patterns. It permitted them to perform structural analyses of a large batch of TiN [1] and TiC_xN_{1-x} thin films grown under various conditions. Likewise, we profit from their excellent thin film preparation capabilities using pulsed reactive crossed-beam laser ablation, a technique which was developed in their laboratory, and which is a very clean and versatile version of laser ablation in which the ablated material is brought onto the substrate by a pulsed molecular beam [2].

11.1 The magnetic phase transition of nickel metal

In collaboration with P. Aebi and L. Schlapbach,
Institut de Physique, Université de Fribourg

Nickel metal is the prototypical band ferromagnet. Nevertheless, it has proven difficult to describe the ferromagnetic-to-paramagnetic phase transition, which occurs at $T_c = 631K$, within one consistent theory [3]. A major puzzle remains that neutron scattering experiments find local magnetic moments and spin waves persisting above T_c [4], while photoemission experiments see a Stoner-like collapse of the exchange splitting $\Delta\epsilon_{ex}$ measured between majority ($\uparrow$) and minority ($\downarrow$) bands [5].

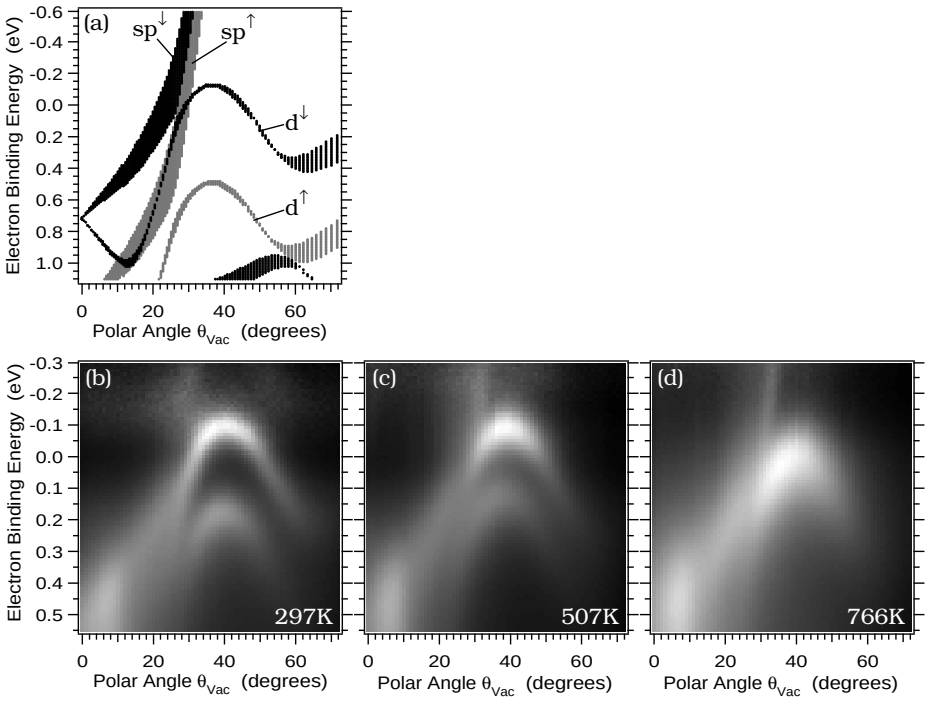

Figure 11.1: (a) - Spin-polarized Korringa-Kohn-Rostoker band structure calculation covering the section in reciprocal space covered by our measurements. Majority spin bands are given in gray, minority bands in black. (b)-(d) : He I excited polar angle scans of photoemission spectra taken from Ni(111), measured at three different temperatures. The data have been divided by the Fermi-Dirac distribution function on the energy scale in order to remove the occupation numbers from the observed bands. The linear gray scale ranges from minimum intensity (white) to maximum intensity (black). The sample temperatures were (b) $T = 0.47T_c$, (c) $0.80T_c$ and (d) $1.21T_c$ from Ref. [6]

.

We have addressed this issue specifically by looking more closely at those regions in wavevector space where the minority d band crosses the Fermi level ϵ_F [6]. Any shift of this band changes the occupation number in this band and is thus directly associated with the average magnetic moment per Ni atom. By means of our clean and intense UV photon source (Gammadata VUV 5000 He discharge lamp with toroidal grating monochromator) we are able to measure band dispersion above ϵ_F in the tail of the Fermi-Dirac distribution function. In Fig. 11.1 b-d the measured bands near the top of the partially occupied d band are shown at different temperatures. Band occupation numbers have been removed by dividing

each spectrum, i.e. each vertical line of pixels in these grey-scale plots, by the Fermi-Dirac distribution function. The room temperature data (Fig. 11.1 b) are well described by a band structure calculation for the ground state (Fig. 11.1 a), except for a roughly twofold expansion of the energy scale due to the neglect of on-site Coulomb correlation effects. Nevertheless, all measured bands can be clearly identified, including the fast dispersing sp bands near the apex of the minority d band parabola [7].

The data sets of Fig. 11.1 b-d provide two significant new aspects concerning the magnetic phase transition in Ni:

(1) We have identified a region in $\vec{k}$ space where the minority d band and the two sp bands cross the Fermi level at the same $\vec{k}$ and with nearly the same group velocity. The existence of such a configuration has important implications for the single-particle excitation spectrum. The Stoner gap, normally associated with spin-flip transitions $d^{\uparrow} \rightarrow d^{\downarrow}$, may here be reduced to zero, because transitions of the type $sp^{\downarrow} \rightarrow d^{\downarrow}$ can be strong. In this scenario, the sp band acts as a minority-spin electron reservoir, permitting $d^{\downarrow}$ states to be filled before the $d^{\uparrow}$ band starts being depopulated upon raising the temperature. The related reduction of the average magnetic moment, and thus of $\Delta\epsilon_{ex}$ supplies the positive feedback which drives the phase transition.

(2) A further indication that we have located the magnetically active region which drives the phase transition is, that, above T_c, the top of the coalesced d band is found to lie precisely at the Fermi level. This means that, for this $\vec{k}$ vector the creation of a spin flip costs no energy. Fluctuating local moments and spin waves in the paramagnetic phase are thus fully consistent with our measurements. Indeed, the anomalously large width observed for the normalized spectrum above T_c (Fig. 11.1 d) might be a consequence of these fluctuations.

11.2 Doping-dependent electronic structure of Bi-cuprates

In collaboration with P. Aebi and L. Schlapbach, Institut de Physique, Université de Fribourg, and H. Berger and L. Forro, EPF Lausanne

A current topic in the research field of cuprate high-temperature superconductors is the evolution of the normal state electronic structure with the hole concentration x in the Cu-O layers. The superconducting transition temperature T_c in these materials strongly depends on this concentration. This is illustrated in the inset of Fig. 11.2 where T_c is shown as function of x for $Bi_2Sr_2CaCu_2O_8$ (Bi2212) [8]. Basically three different doping regimes can be distinguished: It exists an optimal doping x_{opt} where the maximum T_c is achieved (labelled *OPT*). T_c decreases if the hole concentration is higher than x_{opt} (overdoped regime, *OD*), as well as for hole concentrations below x_{opt} (underdoped regime, *UD*). Undoped cuprates ($x = 0$) are not superconductors but antiferromagnetic insulators.

The electronic structure of Bi2212 has been investigated by angle-resolved ultraviolet photoelectron spectroscopy (ARUPS) [9]. Our experimental setup [10] allows to measure directly full $k_{||}$-maps of electronic bands of cuprates [11]. We applied this technique to study the doping dependence of the Fermi surface of Bi2212 at 300K. Full Fermi surface maps of overdoped ($T_c = 60K$), optimally doped ($T_c = 84K$) and underdoped Bi2212 ($T_c = 30K$) samples have been measured. The corresponding He I ($21.2eV$ photon energy) excited $k_{||}$-maps are shown in Fig. 11.2a-c. In each pattern the outer circle represents grazing photoelectron emission, the center point normal emission. The photoelectron intensities are represented in a linear grey scale with high intensity given in white. At **k**-locations of Fermi level crossings high intensities occur.

The analysis of these maps yields that the Fermi surface at optimal doping consists

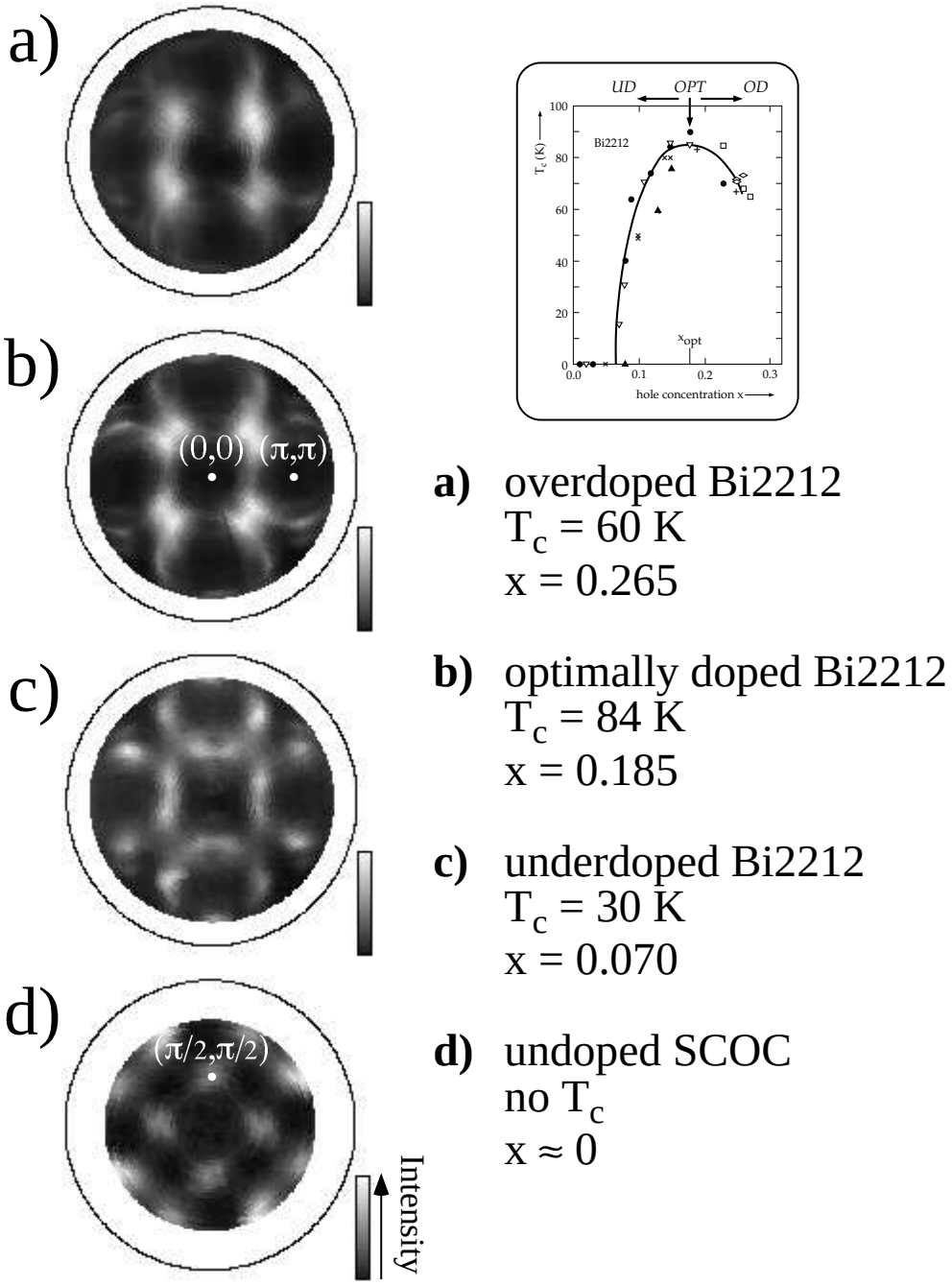

Figure 11.2: He Iα excited photoemission $k_{||}$ maps of cuprates at different doping levels: a) Fermi surface of overdoped Bi2212; b) Fermi surface of optimally doped Bi2212; c) Fermi surface of underdoped Bi2212; d) Valence band maximum map of insulating SCOC. The Fermi surfaces in a-c are raw data, the picture in d has been four-fold averaged. The intensity in all four maps is given in a linear grey scale. The inset shows an experimental T_c vs. hole concentration curve of Bi2212 taken from Ref. [8].

of barrels centered at the (π,π) points, forming a so-called *large Fermi surface* (see Fig. 11.2b). Clearly one can see that the area inside a barrel around (π,π) is shrinking if the hole concentration is lowered. For overdoped and optimally doped Bi2212 we found that this area scales with $(1+x)$, x beeing the hole concentration [11]. For strongly underdoped Bi2212 with a T_c of $30K$ (Fig. 11.2c) a significant deviation from this $(1+x)$ behavior is observed. A second strong difference is that the intensity in the $(\frac{\pi}{2},\frac{\pi}{2})$ region is much higher for underdoped Bi2212 compared to the data at high doping (Fig. 11.2a,b). In underdoped Bi2212 more weight is observed in the same region where the valence band maximum of undoped $Sr_2CuO_2Cl_2$ (SCOC, Fig. 11.2d) is located. This may indicate that the Fermi surface topology is changed at low doping and that small pockets around $(\frac{\pi}{2},\frac{\pi}{2})$ (so-called *hole pockets*) are formed.

We also studied the influence of high flux UV radiation on the surface region of Bi2212. At room temperature the surface layer of Bi2212 is rather inert to residual gases in ultra-high vacuum. However, strong aging effects under the influence of UV radiation are observed, which limit the measuring time on a pristine surface. A careful analysis of these effects lead us to the conclusion that the UV light is underdoping the surface region of Bi2212 samples [11]. This offers the unique possibility to control the doping level in the surface region and to study the doping dependence of the electronic structure on the same cleaved surface.

11.3 Subsurface oxygen on Rh(111)

In a traditional view of heterogeneous catalysis one pictures all molecular processes to take place on top of a more or less static catalytic surface. The only role of the catalyst is to chemisorb and dissociate the reacting molecules. There have, however, been indications that also the subsurface region of the catalyst may be involved in certain reactions. One system where a subsurface species of oxygen might play an important role as an oxygen reservoir is Rh(111) [12]. We have used XPD in order to observe the occupation of subsurface sites by oxygen atoms directly [13].

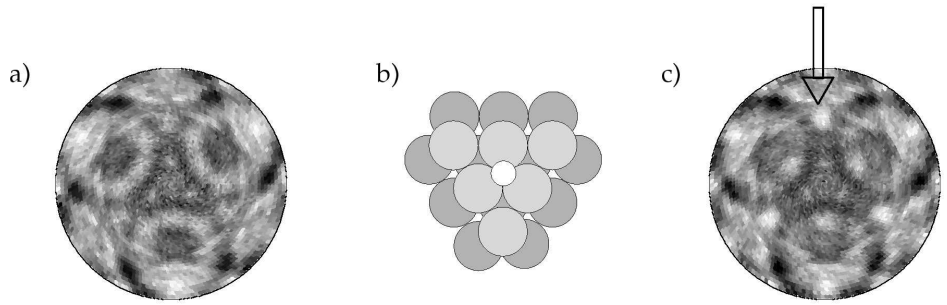

Figure 11.3: a) Mg Kα excited O1s diffractogramm after exposure of 10 L oxygen on Rh(111). The three circular features indicate backscattering from the substrate atoms and allow the identification of the on top adsorbtion site. b) A cluster with two layers of rhodium and one oxygen atom on the surface in the fcc site c) Mg Kα excited O1s diffractogramm after exposure of 10^5 L oxygen. The arrow indicates sharp forward scattering peaks that stem from an ordered subsurface oxygen species.

In Fig. 11.3 a we show the O 1s XPD pattern from a Rh(111) surface which has been exposed to 10 L (1 L (Langmuir) $= 1.33 \cdot 10^{-6}$mbar sec) oxygen at room temperature. Under

these conditions it is known that a "clean" adsorbate structure is formed with oxygen atoms occupying so-called fcc sites (Fig. 11.3 b) 1.25Å above the top Rh layer [14], and with no subsurface oxygen present. In a preliminary analysis using single-scattering cluster (SSC) calculations we can well account for all features seen in the XPD pattern, and we can thus fully confirm the structural model obtained by a quantitative LEED study [14].

In Fig. 11.3 c we show the XPD pattern obtained for a surface exposed to 10^5L oxygen at elevated temperature (470 K), conditions that favour the formation of subsurface oxygen. The pattern remains rather similar to the one of Fig. 11.3 a, since the fcc adsorbate site occupation remains predominant. However, significant intensity enhancements appear as indicated by the arrow. Fig. 11.4 a represents a difference plot where the adsorbate site contribution has been removed by subtracting from this data the 10 L data, leaving only subsurface site emission. The resulting pattern is well described by an SSC calculation (Fig. 11.4 b) assuming the occupation of an octahedral site between the first and second Rh layer, which is just underneath the fcc adsorption site. Surprisingly, we find that in the close vicinity of such a subsurface oxygen species the adsorbed oxygen is now occupying hcp adsorption sites (Fig. 11.4 c). This site switch may be highly relevant for the catalytic properties of the oxygen covered Rh(111) surface.

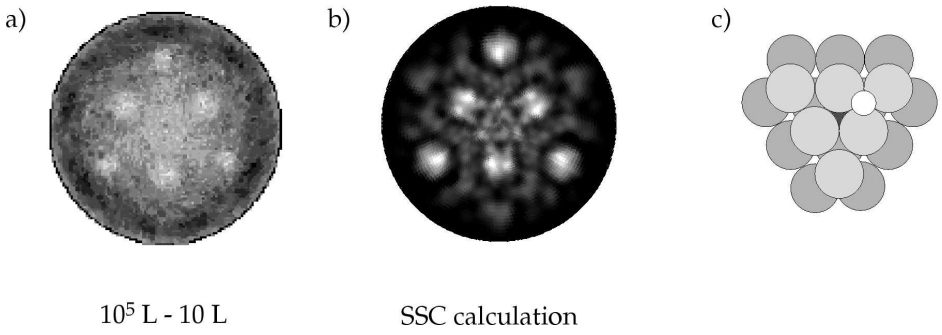

Figure 11.4: a) Difference between Fig. 11.3 c and Fig. 11.3 a. The remaining features are assigned to the subsurface oxygen b) Single scattering cluster calculation (SSC) for the structure as displayed in c). c) Subsurface oxygen in the octahedral site between the first and second rhodium layer. Note the site switch of the on top oxygen (see Fig. 11.3 b).

11.4 Hexagonal boron nitride films on Ni(111)

Monolayers of hexagonal boron nitride have been prepared by the reaction of benzene-like borazine $(BN)_3H_6$ with Ni(111) at 1100 K [15]. A bare nickel surface is a good catalyst for the removal of the hydrogen and therefore the $h-$BN growth rate drops by more than two orders of magnitude after completion of the first layer of boron nitride on Ni(111). The resulting layers are analyzed by means of Si Kα excited N1s and B1s X-ray photoelectron diffraction. In Fig. 11.5 the experimental results are summarized. From the three fold rotational symmetry of the N1s and B1s diffraction pattern it is concluded that the system discriminates fcc from hcp adsorption sites. The higher diffraction anisotropy of the B1s emission pattern compared to that of the N1s pattern indicates that boron emission leads to forward scattering above the surface. From this it is concluded that the $h-$BN layer is corrugated and that nitrogen terminates the surface. The result is in agreement with an existing LEED analysis on the same system with the structure as shown in Fig. 11.5d) [16]. In the near future these $h-BN$ layers will serve as an insulating spacer layer between nickel and other magnetic materials in order to study the magnetic coupling across insulators.

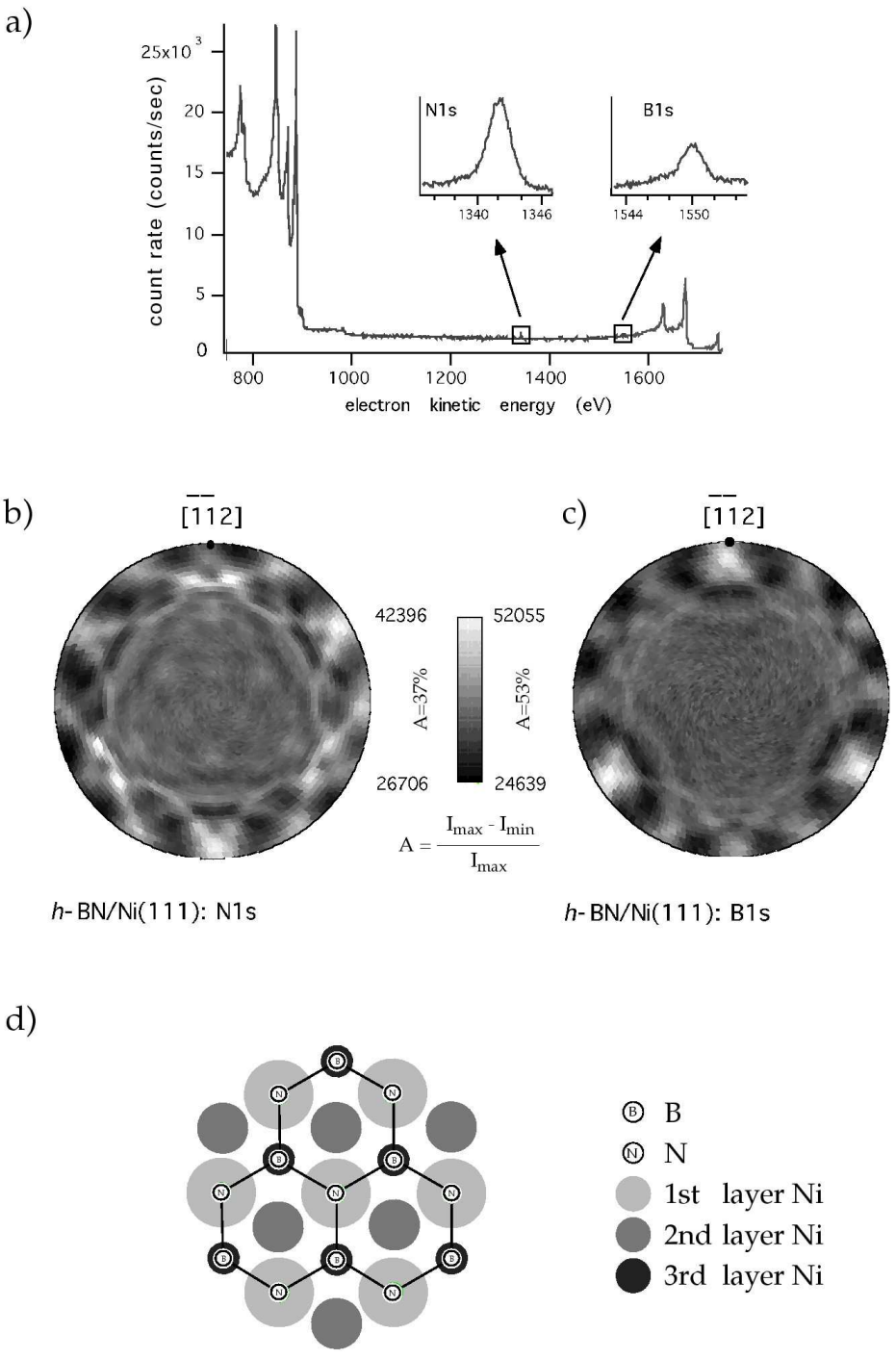

Figure 11.5: Photoelectron diffraction from a monolayer $h-$BN on Ni(111). In a) the photoemission spectrum along the surface normal is shown. The insets indicate the B1s and N1s emission respectively. These emission intensities are stereographically projected in b) (N1s) and c) (B1s) on a linear gray scale for 5044 different emission directions into the hemisphere above the surface. In d) the structure as proposed by Gamou et al. [15] is shown.

11.5 Near-node photoelectron holography

Recently it was shown theoretically that Gabor's idea of photoelectron holography for solving new and unknown structures may be realized if forward scattering is suppressed [17, 18]. In an unusual geometry for photoelectron diffraction the photoemission current is measured near a node of the photoelectron source wave. As a consequence forward scattering that obscures holographic reconstruction in the standard geometry is faded out [18].

In May 1997 we started the set up of a new photoelectron diffraction experiment that will meet the requirements for near-node photoelectron holography. To date the chamber with the monochromatized Al Kα X-ray source and the electron analyzer is pumped and set under ultra high vacuum below $5 \cdot 10^{-11}$mbar. In a next step a 2π goniometer that is produced according to an advanced design in our machine shop will be implemented in the experiment (see Fig.11.6). After tests in the standard geometry the analyzer will be moved to the near node geometry.

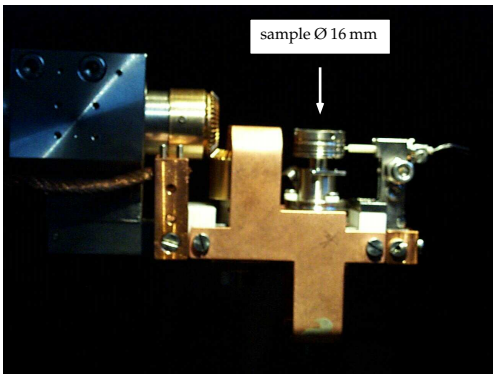

Figure 11.6: Photograph of the new 2π sample goniometer head as produced in our machine shop.

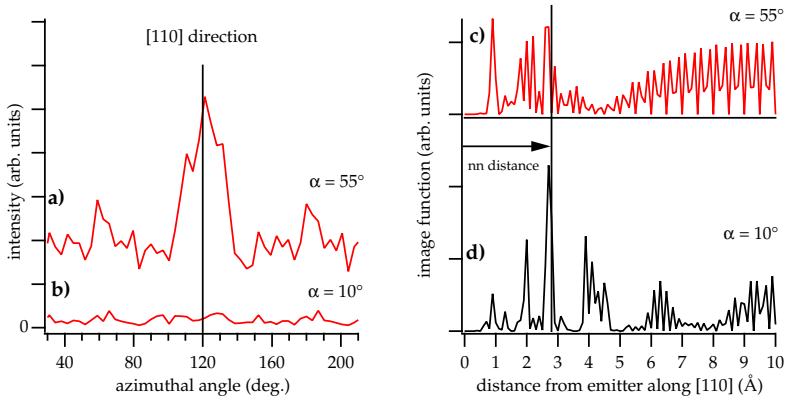

Figure 11.7: Single scattering cluster calculations for Al Kα excited Al2s emission from Al(111). The simulations show an azimuthal scan with a polar angle of 36°. a) Standard geometry with an angle α of 55° between the incoming X-rays and the electron detector b) near-node geometry with an angle α of 10° between the incoming X-rays and the electron detector. It is seen that the forward scattering peak along the [110] direction is suppressed for the near-node geometry. c) and d) show corresponding holographic reconstructions along the [110] direction for c) the standard and d) the near-node geometry. It shows that for the near node geometry the nearfield contribution of forward scattering is suppressed and that the most prominent peak can be interpreted as an image of an atom close to the nearest neigbour (nn) distance.

With further single scattering cluster calculations candidate systems for the first experimental demonstration of near-node photoelectron holography have been evaluated. Since the photoemission intensity drops substantially in measuring the photoemission current near a node of the source wave it is appropriate to start with the analysis of a bulk substrate where several atomic layers contribute to the emission instead of a single layer as proposed in [17]. In Fig.11.7 it is shown that Al is a valuable candidate for the demonstration of holographic reconstruction from near node photoelectron emission data.

11.6 Time-resolved medium-energy electron diffraction

In collaboration with M. Aeschlimann, Institut für Technische Chemie, ETHZ

We have been working on the design of an experimental method for obtaining structural information on solid surfaces on a very short time scale. We are following a scheme where we generate a pulsed electron beam of typically 2 keV energy and measure the angular distribution of the backscattered electrons on a channelplate detector (medium-energy electron diffraction (MEED), also named secondary electron imaging (SEI) - this technique has been largely developed by M. Erbudak at ETHZ [19]). Figure 11.8 shows the realised experimental setup with the home built electron gun (following the design of Ref. [20]), the channelplate electron detector, and the sample holder which can be cooled and rotated. For sample cleaning we have the possibility of ion bombardment. With the same electron detector we can run Auger electron spectroscopy for chemical surface analysis.

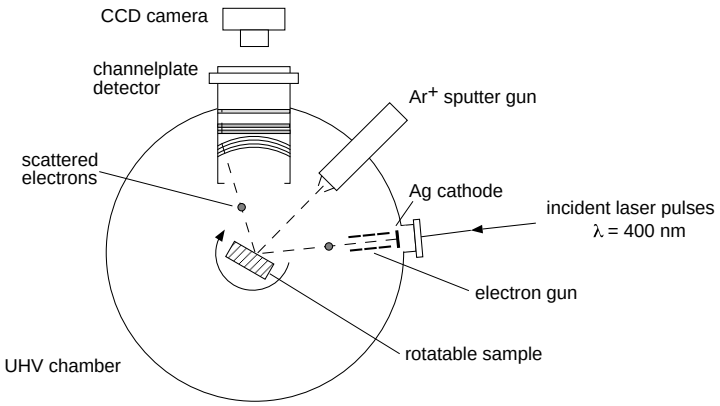

Figure 11.8: Experimental setup of the MEED chamber. Incoming electrons hit the surface at an incidence angle of 85° with respect to the center of the electron detector.

The electron pulses are produced by shining femtosecond laser pulses (duration about 100 fs) on a photocathode. Considering the electron optical properties of our electron gun we expect electron pulses of a few picoseconds in width. The number of electrons in a single pulse is naturally not sufficient to create a measurable diffraction pattern on the screen and we thus have to operate the experiment in a pump-probe mode where we periodically prepare the surface in a defined way at a certain time t_0 and have the electron pulse impinge on the surface with a defined delay dt. In order to achieve picosecond resolution in the delay, the preparation step must necessarily be triggered by a laser pulse which is temporally correlated with the probe electron pulse.

We have a Ti:saphire laser system (Figure 11.9) available in our laboratory producing femtosecond pulses of nanojoule energies. This laser works at a wavelength of 800 nm. For the production of the electron pulses at the photocathode we have to double the optical frequency. For that purpose we use a nonlinear single crystal (BBO). To enhance the photoelectron cur-

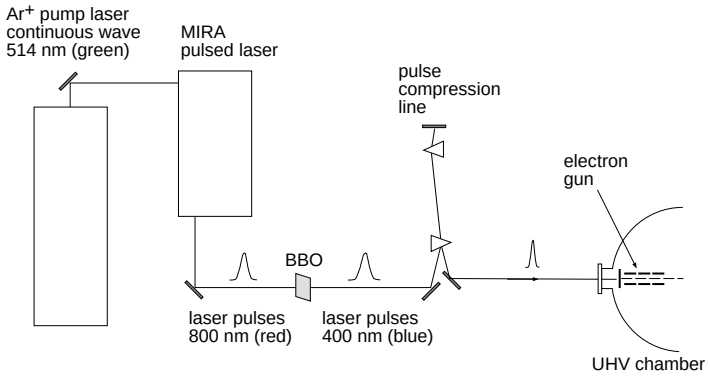

Figure 11.9: Setup for the production of pulsed electrons by a fs-laser system

rent on the cathode we have built a pulse compression line for higher photoemission efficiency. We can use a fs-laser Coherent/Mira borrowed from the Physical Chemistry department for the laser puls production which is pumped by our Ar ion laser. In the next future we will change to a Verdi pump laser by Coherent and move the experiment into a new laboratory. At the moment our MEED scattering chamber is working nicely and first experiments with our pulsed electron gun have proved the feasibility of this experiment.

In our setup the electrons can hit the sample surface at grazing incidence for enhancing the surface sensitivity of the MEED experiment. To explore this sensitivity we use a well known Si(001) surface as a test sample. Si(001) undergoes a dynamical structural change in the topmost atomic layer at 250 K. At room temperature the clean Si(001) surface exists in a reconstructed (2x1) dimers configuration and changes to a c(4x2) structure below 250 K. This change can easily be observed by LEED as a change in the surface periodicity. The MEED technique may potentially deliver information on the atomic arrangement within the surface unit cell in real space if the surface sensitivity can be sufficiently enhanced. Figure 11.10 shows recorded MEED patterns of the Si(001) surface at 200 K, taken at three different sample rotation angles. The visible intensity features show the angle dependent scattering of the incoming electrons. The rotation angles of the sample and of the diffraction features are the same - this behaviour is typical for processes in real space.

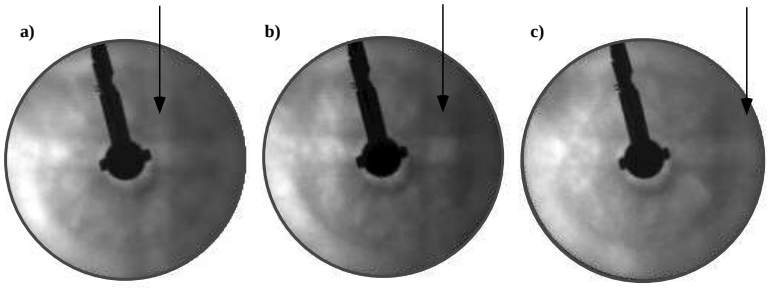

Figure 11.10: MEED patterns of Si(001) at different sample rotational angles: a) 10°, b) 20°, c) 30°. The arrows indicate intensity features, rotating with the sample. The shadow of the second electron gun is visible in the center of the detector.

A particular feature, which is associated with scattering along the [001] direction, is indicated by the arrows. Most of the observed features are rather bulk sensitive. Our current analysis tries to unravel subtle changes that occur at the phase transition temperature, and that would indicate top layer sensitivity.

11.7 Towards a 2d-vapor of sodium atoms

When a surface is exposed to sodium vapor in a UHV chamber at room temperature, sodium atoms may be deposited on the surface either as single atoms, clusters or as a thin 2-dimensional film. Our aim is to demonstrate under these conditions laser-atom-interaction effects previously observed in a normal, three dimensional vapor [21]. One of these effects, called beamswitching [22], where one circularly polarized laser beam switches off another laser beam of opposite circular polarization may be of interest with regard to nanoscale all optical logical gates. Two dimensional in this context means, that the sodium atoms can freely move in two dimensions while their propagation in the third dimension is restricted to less than about 0.5 microns which is about the wavelength of the atomic D1 transition of sodium.

On our way to this goal we have developed a sandwich type sodium vapor cell which can be "loaded" by an electrical current operated sodium dispenser in UHV (fig.11.11).

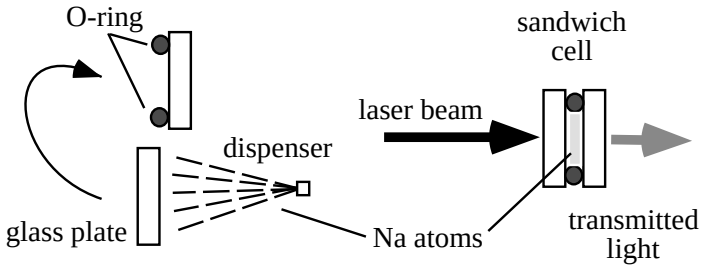

Figure 11.11: Loading of a sandwich cell by a sodium dispenser in UHV

After one glass plate has been sufficiently coated it can be rotated and closes the cell by pressing against the Viton O-ring mounted on the other glass plate. A suitable laser beam, which may or may not be resonant to the atomic D1 transition of sodium, is then directed through the sandwich cell. Due to absorption in the coating the cell heats up and sodium atoms evaporate inside the cell.

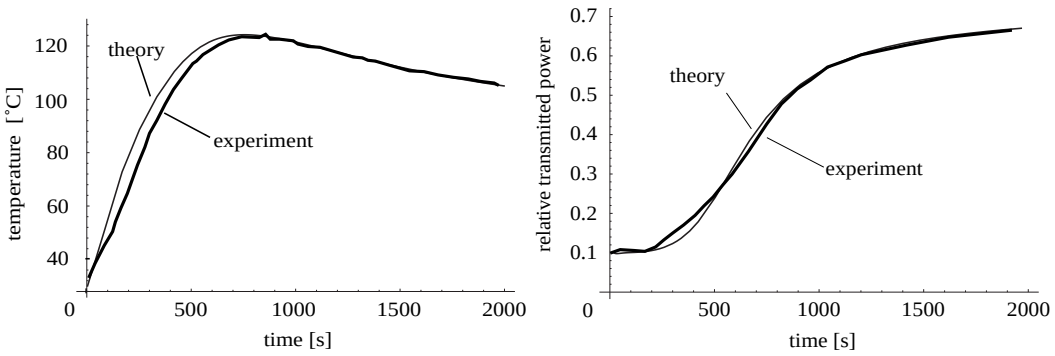

Figure 11.12: Comparison between the measured and the calculated cell temperature and light transmission of the sandwich cell

The cell temperature as well as the transmitted light from the laser beam are measured and compared (fig.11.12) to the values from an according model for the energy flows between the glass plates, the conversion between the input light, sticking coefficients of sodium on glass as well as energy losses due to black body radiation, heat conduction to the UHV chamber and the leakage rate of the cell. In a next step the spacing between the plates is reduced to about 0.5 microns in order to obtain the wanted 2d sodium vapor.

References

[1] R. Timm, P. R. Willmott, J. R. Huber, Appl. Phys. Lett. **71** (1997) 1966.

[2] P. R. Willmott, R. Timm, P. Felder, J. R. Huber, J. Appl. Phys. **76** (1994) 2657.

[3] H. Capellmann, *Metallic Magnetism* (Springer, Berlin, 1987).

[4] G. Shirane, O. Steinsvoll, Y. J. Uemura, J. Wicksted, J. Appl. Phys. **55**, 1887 (1984).

[5] M. Donath, Surf. Sci. Rep. **20**, 251 (1994).

[6] T. Greber, T. J. Kreutz, J. Osterwalder, Phys. Rev. Lett. **79**, 4465 (1997).

[7] T. J. Kreutz, PhD thesis, University of Zürich (1997).

[8] W. A. Groen, D. M. de Leeuw, and L. F. Feiner, Physica C, **165** (1990) 55.

[9] Z.-X. Shen, W. E. Spicer, D. M. King, D. S. Dessau, and B. O. Wells, Science **267**, (1995) 343.

[10] T. Greber, O. Raetzo, T. J. Kreutz, P. Schwaller, W. Deichmann, E. Wetli, and J. Osterwalder, Rev. Sci. Instrum. **68**, (1997) 4549.

[11] P. Schwaller, PhD thesis, University of Zürich (1997).

[12] K. A. Peterlinz, S. J. Sibener, J. Phys. Chem. **99**, 2817 (1997).

[13] J. Wider, T. Greber, E. Wetli, T. J. Kreutz, P. Schwaller, J. Osterwalder, submitted to Surf. Sci.

[14] S. Schwegmann, H. Over, V. De Renzi, G. Ertl, Surf. Sci. **375**, 91 (1997).

[15] Y. Gamou, M. Terai, A. Nagashima, C. Oshima, Sci. Rep. RITU **A44**, 221 (1997).

[16] A. Nagashima, N. Tejima, Y. Gamou, T. Kawai, C. Oshima, Phys. Rev. B **51**,4606 (1995).

[17] T. Greber, J. Osterwalder, Chem. Phys. Lett. **256**,653 (1995).

[18] T. Greber, J. Osterwalder, Prog. Surf. Sci. **53**,163 (1997).

[19] M. Erbudak, M. Hochstrasser, E. Wetli, and M. Zurchkirch, Surf. Rev. Lett. **4** (1997) 179.

[20] M. Aeschlimann, E. Hull, J. Cao, C.A. Schmutternmaer, L.G. Jahn, Y. Gao, H.E. Elsayed-Ali, D.A. Mantell, and M.R. Scheinfein, Rev. Sci. Instrum. **66** (2) (1995) 1000.

[21] R. Holzner, J. Simonet, L. Flepp, B. Röhricht, P. Eschle, S. Dangel, U. Rusch, H. Schmid, and E. Brun. Using nuclear spins, radio waves, sodium atoms, and laser light to investigate spatiotemporal nonlinear systems. *Optical Engineering*, 34:2315–2323, 1995.

[22] S. Dangel, P. Eschle, B. Röhricht, U. Rusch, H. Schmid, and R. Holzner. Dynamics of laser beam switching in sodium vapor. *J. Opt. Soc. Am. B*, 12(4):681–686, 1995.

12 Laser Dynamics

S. Dangel, A. Schneider, R. Holzner

A main part of our research activities, besides the laser related projects described in the section on surface physics, is the investigation of nonlinear spatio-temporal effects caused by the interaction of resonant laser beams with sodium atoms in the gas phase. A circularly polarized laser beam propagating through sodium vapor can optically pump sodium atoms into a nonabsorbing ground state (optical pumping). This strongly nonlinear mechanism which occurs even at very low light intensities causes an intensity dependent refractive index gradient along as well as transverse to the laser beam propagation direction which may give rise to a number of nonlinear spatio-temporal intensity and polarization pattern creating processes.

Probably the first observations of optical pumping of sodium atoms as beeing the cause for laser beam shape modifications were self-focusing, self-defocusing and self-trapping of the beams [1]. Since then a large number of optical pumping related effects have been observed by various research groups. A collection of effects which we have observed in experiments and described by appropriate models [2, 3, 4, 5] are displayed in fig.12.1.

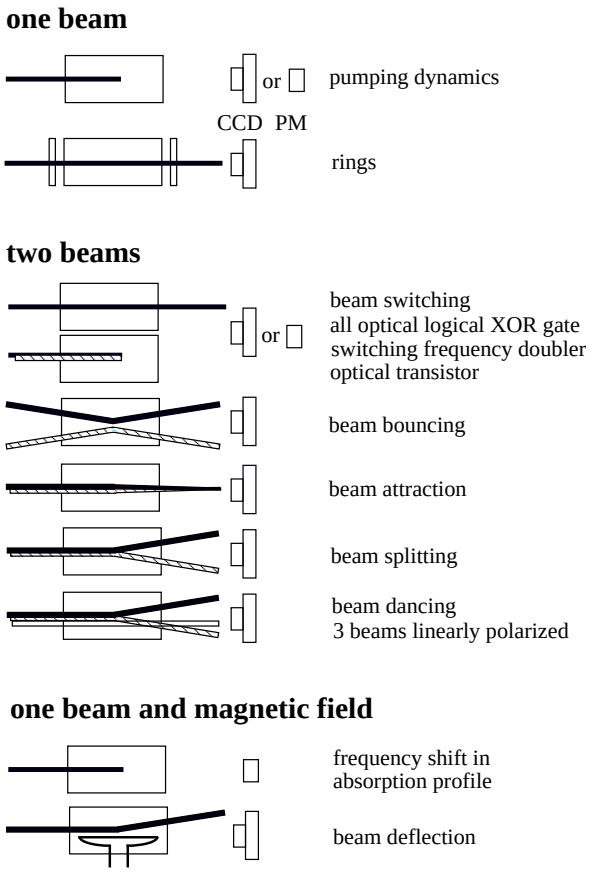

Figure 12.1: Collection of observed effects when circularly polarized laser beams propagate through sodium vapor. CCD: recording by a CCD camera, PM: recording by a photo multiplier.

One of the most basic cases of dynamic behavior, where only a single circularly polarized

beam "pumps" its way through the medium, is an important test case for the theory [6] since it demonstrates disagreement by about an order of magnitude between the time scale of optical pumping observed in experiments [7, 6] and predicted by the commonly used $J = \frac{1}{2}$ model. It needed our recently developed model [3], which includes the hyperfine structure of the atomic transition, to obtain the realistic (slower) time scale.

The observed ring patterns [8] caused by a single near circularly polarized laser beam represent a novel phenomenon which combines two processes. The first one is induced gyrotropy in the case of a near-resonant atomic vapor. The second process is that of spatial separation of polarization components which made its first appearance in the form of filaments with opposite circular polarization in sodium vapor [9], but has more recently been observed to occur in a *cylindrically symmetric* manner when an elliptically-polarized beam propagates through a collisionally-broadened $J = \frac{1}{2}$ system.

The effect of beam splitting [10] represents a polarization instability, where an initially "pseudo-linearly" polarized beam breaks up into two circularly polarized beams. Polarization instabilities play an important role e.g. in sodium vapor related work with regard to optical bistability and multistability, polarization switching, self oscillations or chaotic behavior.

Beam bouncing, beam splitting and the mutual attraction of two laser beams shine new light on the related classic experiments of Tam and Happer [9]. In their experients, Tam and Happer observed two major effects. One is the mutual repulsion of two equally circularly polarized beams or the mutual attraction of two opposite circularly polarized beams (beam bouncing or beam attraction) and the other one is the spontaneous break-up of a linearly polarized beam into two distinct beams of opposite circular polarization (beam splitting). Their explanation of the observed effects by introducing gradient forces or ponderomotive forces however is inconsistent [11]. Tam and Happer base their semiclassical and semi-quantitative theory on the belief that the force is transmitted between the beams by sodium atoms in much the same way that virtual photons are believed to transmit the force between the charged particles. Their explanation of the bending of the laser beams is based on the assumption that a sodium atom with "spin up" is repelled by a σ^+ and an atom with "spin down" by a σ^- circularly polarized beam. As a result, the beams bend under the force of reaction. However, in a vapor the atoms fly in all possible directions. The net reaction force therefore vanishes and no beam bending takes place. Furthermore, even if the atoms prefer a flight path between the beams, attraction between two σ^+ beams can not be explaned because the above mentioned reaction force is allways repulsive. An alternative theory [11] assumes an interaction between photons which is mediated by an axial photon [12] (axial vector torsion) leading to a long range spin-spin interaction enhanced by the optically pumped and therefore spin polarized sodium vapor. Fitting the theory to the experimentally determined beam separations of [9] as a function of sodium density, Naik et al. found a coupling strength of the new spin-spin interaction which is about 10^{-9} times smaller than that of the usual electromagnetic spin-spin interaction. This is less than the weak interaction. Its contribution to QED phenoena in vacum is negligeably small but may manifest itself in astrophysical processes through the possibility of photon- neutrino interaction. The force would be Coulomb like and would allow for a photon photon scattering in second order of the coupling strength rather than in fourth order as is the case in usual QED photon-photon scattering. This theory, however, which would have implications related to the debate about a spin dependent fifth force, the stability of the electron or to the existence of an analogous Aharonov-Bohm Effect for photons and contributions to the hyper fine level splitting, has been questioned by Oblukhov et.al. [13]. Until today this interesting subject has not been fully understood. Unfortunately the second observation of Tam and Happer, the beam splitting, has not been adressed by these autors at all. Considering our own results in connection with beam bouncing in the presence of

buffergas, which enhances optical pumping, reduces atomic diffusion and allows for models explaining all observed behavior, we favour a more simple explanation in terms of refractive index gradients which attract or repell the beams depending on their circular polarization.

The occurence of beam splitting is most likely due to optical pumping effects combined with fluctuations of the atomic density, the laser beam intensity, the polarization, small residual magnetic fields and deviations of the beam intensity distribution from an ideal Gauss profile. These imperfections break the cylindrical symmetry and can initiate beam splitting of a linearly polarized beam. The full theoretical treatment would involve Doppler broadening and nonlocal polarization effects due to atomic motion between the laser beams which is not yet included in our present models.

Involving magnetic fields is of particular interest since they affect the optical pumping induced alignment of the atomic magnetic moments. A most striking example is the large apparent shift of absorption profiles [14] in the case of a single circularly polarized laser beam propagating through sodium. The effect is caused by the combination of three well known effects "optical pumping", "light-shift" and "Larmor precession".

A further astonishing effect (described in more detail in the following subsection) due to the combination of optical pumping and magnetic fields is the deflection of a laser beam by the inhomogeneous magnetic field of a current carrying wire.

While the steady state behavior of these effects has been observed and described in the past, only recently the modeling of the dynamics of the pattern formation processes has become possible by considering all hyperfine states of the atomic D_1 transition.

Beam deflection by a current carrying wire

A circularly polarized laser beam propagating through sodium vapor is deflected [15] by the inhomogeneous magnetic field from a nearby electric current-carrying thin wire aligned parallel to the beam (fig.12.2).
The effect arises from the refractive index gradient induced by magnetic-field-modified optical pumping. The time of order 100 ns needed for the beam to switch between undeflected and deflected positions is determined by the average Larmor precession period and is two orders of magnitude shorter than the optical pumping time. The electric current of 60 mA needed to produce an appreciable steady-state beam deflection—28 μm measured at the cell output window as shown in Fig. 12.2 —gives rise to a slight temperature change in the wire. After about 5 ms the heating effect causes the local sodium density to rise and leads to an increase of beam deflection. "Steady-state" deflections, shown in Fig. 12.2(right), are recorded between 1–30 μs after current initiation; sufficiently delayed to avoid the initial transients in beam displacement but before the onset of thermal effects.

The basic mechanism can be understood by considering the effect in terms of an encoding/diffraction sequence. A somewhat over-simplified view (which ignores the spatial variation of intensity across the beam as well as absorptive effects) is that the optically-pumped medium can be approximately described as a glass prism of refractive index less than unity. The 'thick' edge of the prism is adjacent to the wire where the high magnetic field inhibits optical pumping, and the medium has near-normal refractive index. Further from the wire, where the magnetic field is insufficiently large to suppress optical pumping, the medium is bleached with a refractive index tending towards free space; here, the prism has its 'thin' edge. The net effect of the prism is to phase encode the laser beam and bend the propagation direction away fom the wire.

An important issue is that the steady-state density distribution of absorbing atoms can change much faster by the application of a transverse magnetic field gradient than by optical

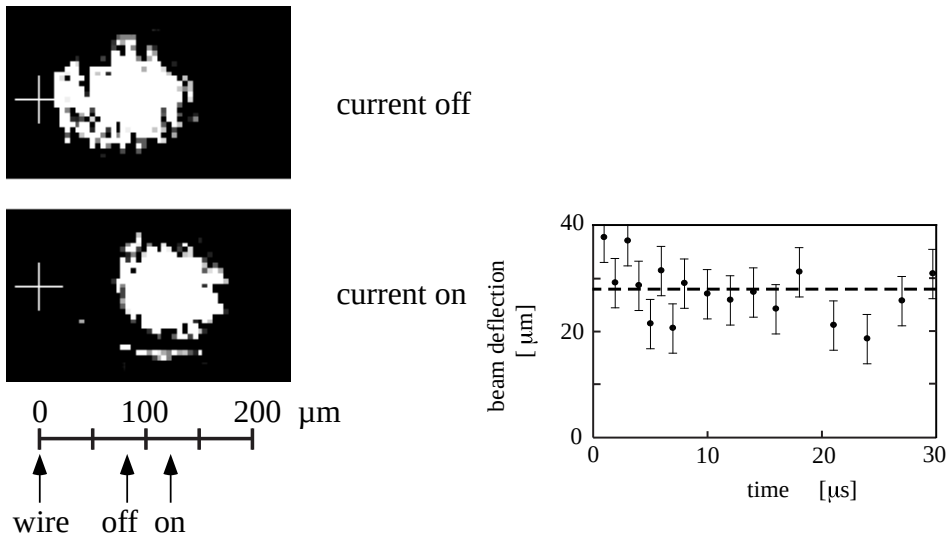

Figure 12.2: Left: Undeflected and deflected beam spots at the output window of the sodium vapor cell before and after the electric current through the wire has been switched on. For the determination of the beam positions only pixels brighter than 50% of maximum are considered. Right: Beam deflection during the first 30 μs after the current has been switched on. Error bars indicate the standard deviation of 10 measurements taken within 3 minutes. The main causes for the scatter of single measurements are the fluctuation of the input laser intensity as well as density fluctuations inside the vapor cell. The dashed line marks the mean deflection of (28$\pm$2) μm averaged over the displayed series of 17 times 10 measurements.

pumping.

In Fig. 12.3 we present simulation results showing how the spatial distribution of the field intensity evolves.

When there is no electric current, the beam establishes an undeflected steady-state profile after about 20 μs (Fig. 12.3(a)). Upon application of the current at $t = 0$ the beam quickly deflects to its final position: Fig. 12.3(b) gives the situation after 50 ns. The reason for this rapid response is that the magnetic field depolarizes the ground state within a fraction of an average Larmor period (i.e. sub-microsecond). Although the deflection suffers little further change the output intensity at beam center continues to grow as optical pumping becomes more complete, and eventually a steady state is achieved, as shown in Fig.12.3(c), 20μs after the current is turned on. The simulated beam deflection in the final steady-state, 34μm, is in good agreement with experiments shown in Fig.12.2, given that all parameters used in the theory correspond to experimentally determined values without fitting. The destruction rate Γ_l of the ground-state orientation includes the effects of radiation trapping and is determined as described in [14].

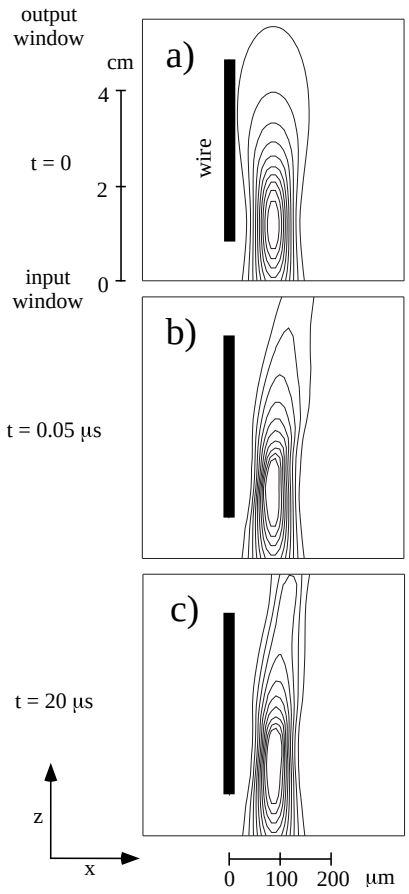

Figure 12.3: Intensity contour plots of the laser beam in the $y = 0$ plane from the simulation: (a) steady-state with no current; (b) 50 ns after the current is turned on; (c) steady-state 20 μs after current is turned on. The wire is parallel to the z axis at $x = 90$ μm, $y = 0$. From 6 mW input-beam power, 5.5 mW penetrates the vapor in (a) and 1.8 mW in (c).

References

[1] J.E. Bjorkholm and A. Ashkin. Cw self-focusing and self-trapping of light in sodium vapor. *Phys. Rev. Lett.*, 32:129–132, 1974.

[2] R. Holzner and S. Dangel. Optical pumping-induced spatio-temporal modifications to propagation, polarization and intensity of laser beams in sodium vapour. *J. Europ. Opt. Soc. B*, 10:R1–R22, 1998.

[3] S. Dangel and R. Holzner. Semi-classical theory for the interaction dynamics of laser light and sodium atoms including the hyperfine structure. *Phys. Rev. A*, 56:3937–3949, 1997.

[4] S. Dangel and R. Holzner. Dynamics of light pattern formation for polarized laser beams propagating through sodium vapor. *J. Opt. Soc. Am. B*, 15:594–606, 1998.

[5] R. Holzner, J. Simonet, L. Flepp, B. Röhricht, P. Eschle, S. Dangel, U. Rusch, H. Schmid, and E. Brun. Using nuclear spins, radio waves, sodium atoms, and laser light to investigate spatiotemporal nonlinear systems. *Optical Engineering*, 34:2315–2323, 1995.

[6] S. Dangel, P. Eschle, B. Röhricht, U. Rusch, H. Schmid, and R. Holzner. Dynamics of laser beam switching in sodium vapor. *J. Opt. Soc. Am. B*, 12(4):681–686, 1995.

[7] D. Suter. Optically excited Zeeman coherences in atomic ground states: nuclear-spin effects. *Phys. Rev. A*, 46(1):344–350, 1992.

[8] B. Röhricht, U. Rusch, S. Dangel, H. Schmid, P. Eschle, R. Holzner, and W.J. Sandle. Optical pumping induced ring structures of polarized laser light propagating through sodium vapor. *J. Opt. Soc. Am. B*, 12(8):1411–1415, 1995.

[9] A. C. Tam and W. Happer. Long-range interactions between cw self-focused laser beams in atomic vapour. *Phys. Rev. Lett.*, 38(6):278–282, 1977.

[10] B. Röhricht, A. W. McCord, M. Brambilla, F. Prati, S. Dangel, P. Eschle, and R. Holzner. Spatial separation of circularly polarized laser beams in sodium vapor. *Opt. Comm.*, 118:601–606, 1995.

[11] P.C. Naik and T. Pradhan. Long-range interaction between spins. *J. Phys. A*, 14:2795–2805, 1981.

[12] T. Pradhan and A. Lihiri. Finite quantum electrodynamics. *Phys. Rev. D*, 10:1872–1882, 1974.

[13] Y.N. Oblukhov and I.V. Yakushin. Experimental restrictions on spin-spin interaction in gauge gravity. *Int. J. Theor. Phys.*, 31:1993–2001, 1992.

[14] B. Röhricht, P. Eschle, C. Wigger, S. Dangel, D. Suter, and R. Holzner. Large frequency shifts of absorption profiles due to the combination of optical pumping, light shift, and magnetic fields in sodium vapor. *Phys. Rev. A*, 50(3):2434–2437, 1994.

[15] R. Holzner, P. Eschle, S. Dangel, R. Richard, H. Schmid, U. Rusch, B. Röhricht, R. J. Ballagh, A. W. McCord, and W. J. Sandle. Observation of magnetic-field-induced laser beam deflection in sodium vapor. *Phys. Rev. Lett.*, 78:3451–3454, 1997.

13 Computer Assisted Physics

P. F. Meier, R. M. Dünki, R. Füchslin, P. Gravila, P. Hüsser, S. Schafroth, and J. M. Singer

13.1 Introduction

The Computer Assisted Physics group has continued its research activities in computational physics. Selected examples of progress are presented in the following subsections. They comprise (i) simulations of superconducting tunneling junctions which are being developed at PSI as high resolution photon detectors and (ii) investigations of high-temperature superconductity, in particular cross-over, scaling and quantum critical phenomena. Quantum Monte Carlo simulations were performed to study the phase diagram of the attractive Hubbard model and the occurrence of the so-called spin gap. In addition, (iii) in a collaboration with the Institute for Physical Chemistry calculations for the polymerization of free radicals have been carried out. In a thesis work, the adsorbtion geometry of Na and K on the Si(001) surface has been calculated by means of density-functional methods (iv). Finally, (v) we report on the activities in the analysis of non–linear dynamical systems and biosignals, a project which is pursued in the frame of a collaboration with medical scientists.

13.2 Theoretical study of superconducting tunneling junctions

A photon hitting a superconductor produces quasiparticles and phonons. In a thin superconducting film these quasiparticles can be collected via a tunnel junction, and measuring their number allows to draw conclusions about the energy of the impacting photon. This detector scheme is far from being new, for semiconductors it is well known. Superconductors are of interest as detector materials because the gap energy of a superconductor is about thousand times smaller than that of semiconductor. The same photon energy produces more quasiparticles and therefore allows a higher resolution ($\approx 1/\sqrt{1000}$).

Recent developments in the production of superconducting tunneling junction detectors (STJD) focussed on thin, strip-shaped devices with two junctions (see fig. 13.1), one at each end. They allow in addition to the determination of the energy of the incoming photon a measurement of the position of the impact by comparing the energies collected by each of the junctions.

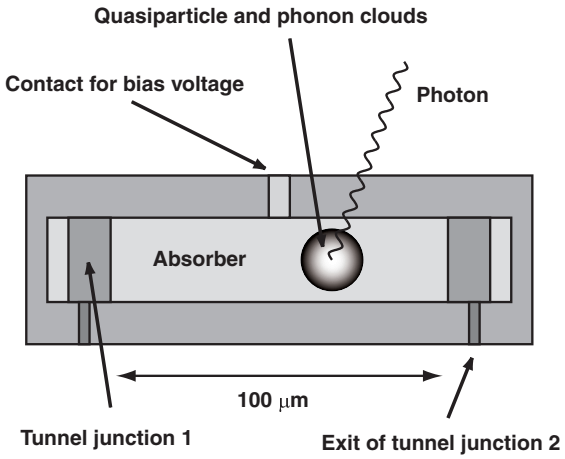

Figure 13.1: Scheme of a detector with two junctions.

In order to simulate the measured signal (the tunnel current in the junctions), one has

to understand the dynamics of a STJD, which is governed mainly be two processes: First, the interaction of quasiparticles with phonons, which are described by a model of Chang and Scalapino. Second, diffusion takes place. We show that under certain circumstances the relaxation due to interactions and the diffusion can be decoupled.

The numerical solution of the Chang - Scalapino equations (CSE) is far from being trivial. It turned out that a direct approach by transforming the CSE, which are a system of integro-differential equations, into a system of ordinary differential equations does not always lead to satisfactory results. The amount of CPU - time needed is very high and occuring numerical problems cannot be neglected. Therefore, we were forced to develop an alternative procedure. By introducing a novel method of calculating specific numerical solution of integro-differential equations, which we call "pseudolinearization", and deriving an also novel method to calculate numerical integrals of a type typically occurring in scattering problems, we were able to overcome these difficulties. We showed that

- the quasiparticle and phonon distribution reach a quasistable state (a state which can be regarded as stationary with respect to time intervals of the order of microseconds) within a material and temperature dependent relaxation time τ_{relax},
- these distributions do not depend on the detailed structure of the initial distributions, but only on the energy of the impacting photon,
- after τ_{relax} and for temperatures below 1/4 T_c most of the energy is stored in the quasiparticle system.

The last fact is especially important because the operating temperature of a STJD is around 0.5 K and, as can be seen in fig. 13.2, materials like tantalum or niobium, which are favored as detector materials also for other reasons, exhibit a practically ideal efficiency.

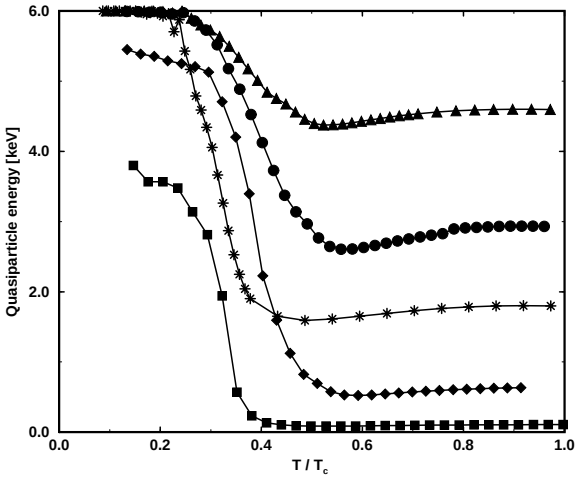

Figure 13.2: Energy of the quasistable quasiparticle distribution as a function of temperature after the impact of a 6keV photon. Ta: (●), Va: (▲), Sn: (♦), In: (■), Nb: (∗).

We could also show that in the investigated systems the diffusion can be decoupled from the relaxation due to quasiparticle-phonon interactions. This fact allows to construct an efficient method to simulate the behavior of an STJD under inclusion of technical details of the measurement apparatus. Together with these simulations, an involved data analysis

procedure could be set up and unknown parameters of the STJD could be calculated. In collaboration with A. Zehnder and his group at the PSI in Villigen, we were able to determine values for the diffusion constant of the quasiparticles and their effective lifetime.

The comparison of our calculations with recent experimental results [1, 2, 3] shows a good agreement. For special cases, theoretical investigations have been carried out by other authors (see for example Kaplan *et al.* [4]). Our results are fully compatible with their calculations. Therefore, we are convinced of the validity of our approach.

13.3 Crossover, scaling and quantum critical phenomena in high-temperature superconductors

We investigate crossover phenomena, universal scaling and quantum critical properties of high-temperature superconductors within three approaches:

13.3.1 Attractive Hubbard model

The first approach is the exploration of the phase diagram of the attractive Hubbard model by numerical quantum Monte Carlo methods as well as the scaling theory of quantum critical phenomena and approximative approaches. The attractive Hubbard model serves as a basic minimal model to give the proper (in view of the cuprates) phase transition phenomenology. We do not propose this model as a realistic high-T_c model itself, but use it to deepen our understanding of the phase diagram and to explore the effects of pairing fluctuations on various thermodynamic properties (density of states, spin susceptibility, etc.). Indeed, from the

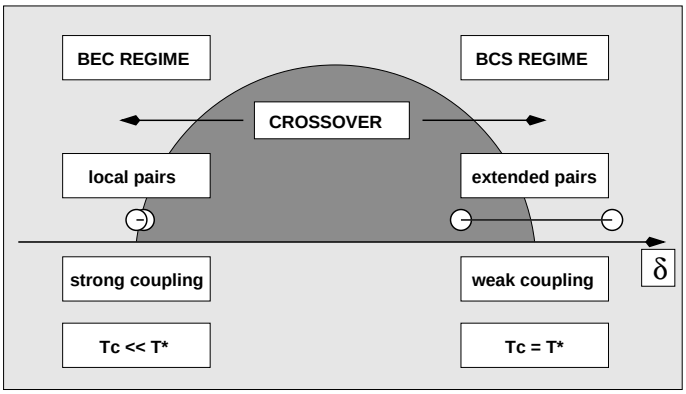

Figure 13.3: "Crossover" from a BCS-like endpoint to a BEC endpoint along the superconducting phase transition line. δ symbolizes a control parameter driving the crossover, which is in this phase diagram associated with the (inverse) coupling strength in case of the attractive Hubbard model and the electronic carrier doping in case of the cuprates.

aspect of universality and critical phenomena our analysis strongly reveals close similarities between the overdoped regime in the cuprates and the weak coupling regime of the attractive Hubbard model (both are close to a superconductor – normal metal endpoint) on the one side, and the underdoped respectively strong coupling regime (which are close to a superconductor to insulator critical endpoint) on the other side. Because of its conceptual simplicity, the attracive Hubbard model allows an easy investigation of the crossover from weak to strong coupling, from extended to local pairs, from BCS-like superconductivity to a Bose-Einstein condensation (BEC) of local pairs, just by tuning the coupling strength U, which acts as a control parameter for the phase transition line in analogy to the carrier doping in case of the cuprates.

13.3.2 Crossover and quantum critical properties in the cuprates

We apply the scaling theory of quantum phase transitions to the experimental phase diagram of high temperature superconductors in the temperature - doping plane. We find that the relation between transition temperature T_c and zero temperature penetration depth, and the sheet resistance become universal in the underdoped limit where the materials are essentially twodimensional and the insulator to superconductor transition occurs. The predominance of phase fluctuations in this doping regime manifests itself as a suppression of the fermionic density of states around the chemical potential, that is, in terms of a pseudogap. This provides a natural explanation of a variety of measurements, which show a pseudogap opening above T_c.

13.3.3 Universality and scaling theory of classical critical phenomena at finite temperature

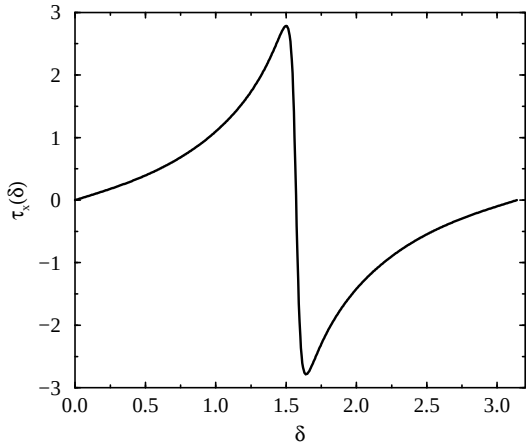

Figure 13.4: Theoretical prediction for the angular dependence of the magnetic torque τ_x for an anisotropic type-II superconductor with effective mass anisotropy $\gamma = 25$ in a regime close to but below T_c. This predictions are consistent with experimental data.

An anisotropic Ginzburg-Landau functional is used for extreme type-II superconductors such as the high-T_c cuprates in the presence of a magnetic field. This allows a formulation of the scaling properties for the singular part of the free energy. We can determine the limiting behavior of the scaling function in the vicinity of the zero-field transition temperature (where critical fluctuations dominate) from the existence of magnetization, a diamagnetic susceptibility and the Meissner effect. This allows predictions for the temperature and field dependence of a variety of quantities, among which angular dependence of the magnetic torque (which results from the noncollinearity of the magntic moment and field) in the superconducting state is shown.

The presented work has been carried out in collaboration with T. Schneider (Uni Zürich), M. Pedersen (U. Geneva), the Zurich University Magnetic Torque group (Prof. Keller and collaborators) and the Zurich University NMR group (Prof. Brinkmann and collaborators).

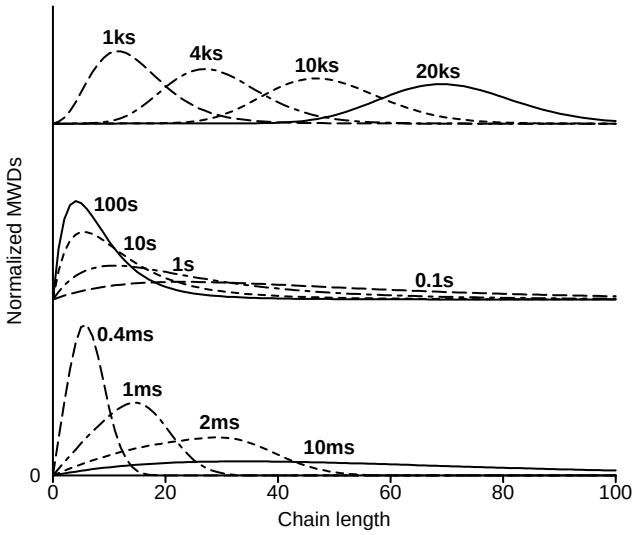

Figure 13.5: Time evolution of the molecular weight distribution (MWD). Traces are grouped and shifted vertically for clearness. Each trace is labeled with the corresponding time.

13.4 "Living" free–radical polymerization

"Living" free–radical polymerization (LFRP) has recently attracted much attention because it may avoid the shortcomings of conventional free-radical polymerization, in which broad polydisperse products are inherently produced. Polymers prepared using LFRP have some very desirable properties, namely low polydispersities and controllable molecular weight.

A model of such a LFRP scheme consists of the following reactions: activation/deactivation exchange between growing and dormant chains, chain propagation and an irreversible chain termination. The dormant chains are formed by a stable free radical and a growing chain. It is evident that the possibility of biradical termination to form dead polymers (polymers which do not react further) will be greatly reduced because of the equilibrium between the growing chain radicals and the stable radicals.

We started a collaboration with the physical chemistry institute to investigate the behavior of the LFRP scheme by a numerical model. The kinetics of the system can be modelled by a set of ordinary first order differential equations. By large-scale numerical simulations we got a more detailed understanding of the mechanisms of LFRP than is possible by analytical studies.

Some typical MWDs (molecular weight distributions) are shown in figure 13.5. For very small times, when the concentration of the stable radical is low, the chain growth is not controlled and the width of the MWD gets very large. At about 10 ms the width reaches a maximum. At this time the controlled chain growth starts. A peak in the MWD for small chain lengths begins to develop and shifts towards longer chain lengths as time and monomer conversion proceed. A monomer conversion of 90% is reached in about 12 hours. At that time the polydispersity index is 1.022 which is very close to the theoretical limit of one. The standard deviation of the MWD is 27 for a mean chain length of 200.

13.5 Theoretical determination of the adsorption geometry of Na on the Si(001) surface

The adsorption of metals on the Si(001) surface is a topic of great interest due to its scientific and technological importance. Many experimental techniques have been developed for investigating surfaces but, unfortunately, there is no single tool for measuring surfaces that has the reliability of X-ray crystallography for bulk. Usually, one has to postulate a surface structure in order to interpret the experimental data. On the other hand, density functional methods became increasingly successful in performing theoretical, *ab initio* calculations for surfaces.

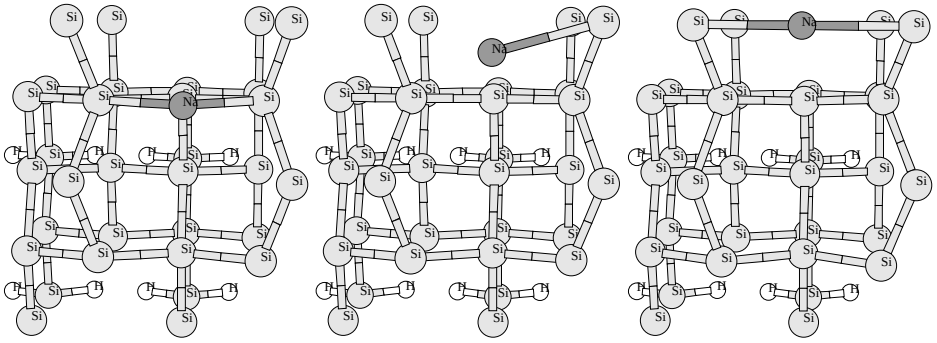

Figure 13.6: Transition of a Na adsorbate from the hollow to the cave site. Top view of the relaxation of the Na/Si(001) surface at a coverage of 1/4. The Na atom in the hollow site moves into the cave site. The starting position, an intermediate frame and the final position in the cave site are displayed.

From all metals, alkali metals such as Na and K are the simplest and the system Na (or K) on Si(001) became a benchmark for combined theoretical and experimental investigations. Many aspects of this surface like adsorption geometry, charge transfer, critical coverage are still debated.

We performed *ab initio* total-energy calculations for Na and K on the Si(001) 2×1 surface at coverages ranging from one-forth to one monolayer by the use of the density-functional method with a plane-wave basis set and a slab with a 2×2 surface cell.

In the initial stages of the energy optimization the Na approaches the surface with a simultaneous relaxation of the substrate atoms. Such a relaxation process is shown in Fig. 13.6. The adsorption of a Na atom in the "hollow" site (atop a Si atom of the third layer) turns out to be instable and the adsorbate moves into the "cave" site (atop a Si atom from the fourth Si layer). The forces acting on the ions are derived from the Hellmann-Feynman theorem. While for the electronic system a full quantum mechanical calculation is performed, the ions are relaxed using a classical Newton dynamics.

We obtained a highest coverage of one monolayer (i.e. two adsorbates per Si-Si dimer) corresponding to a double-layer structure with combined occupation of the hollow and pedestal sites. Thus, in the frame of our 2×2 surface cell, we predict an adsorption scenario with a phase transition during which adsorbates are moving from "cave" to "hollow" sites with increasing coverage.

We investigated the problem of the charge transfer between the alkali metal and the substrate using the difference between a converged density with a Na (or K) adsorbate and a similar slab with a clean Si(001) surface. Both alkali metals displayed a charge distribution pattern at 1/4 coverage that suggests a polarized covalent bond.

13.6 Dynamical systems analysis and biosignals

Our collaboration with the Cantonal Psychiatric Clinic in Rheinau continued. The aim is to explore the extent to which analysis of bio-medical time series by means of nonlinear dynamical systems theory improves current findings. In particular, we analysed the EEG of two groups, namely, 15 patients in the acute schizophrenic state and 15 controls in a healthy state. Both groups where exposed to different mental situations and each such situation resulted in three 30 second segments of EEG to be further analysed.
EEG were recorded according to the international 10-20 standard, which allows for the so-called parallel embedding scheme (Fig. 13.7).

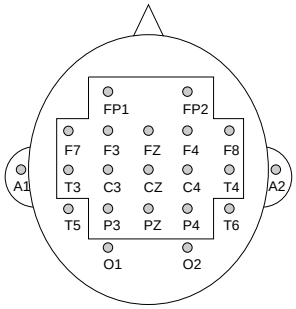

Figure 13.7: EEG-Electrode positions according to the international 10-20 scheme [7]. The measurements of the 15 electrodes from within the rectangle are included into the analysis, thereby building a 15 dimensional phase space.

One hereby regards each electrode as a coordinate in a phase space and includes the simultaneous time series from more and more electrodes in the analysis [5].
Our nonlinear EEG analysis follows a biparametric dimensional technique. In contrast to standard methods, this technique also considers attractor unfolding and the outcomes are several nonlinear measures, namely, the asymptotic correlation dimension (D_2), the so-called unfolding dimension m^* and the relative unfolding χ [6]. In addition, EEG analysis with conventional FFT techniques was performed at the hospital and clinical staff ranked each patient's symptoms on a psychiatric rating scale. First assessments using multivariate statistical techniques indicated significant differences in the EEG of patients and controls. This resulted in constructing a discriminance function which allows to correctly classify 83 % of the probands based on their EEG.

Deeper insight may be gained when relating the outcomes of our nonlinear EEG analysis with clinical measures. An example is shown in Fig. 13.8. The extrapolation of the regression line to symptom rating zero (where healthy probands are expected to reside) displays an interesting finding: This extrapolation does not match with the outcome of the healthy probands. Provided that there are no cumbersome effects due to distortion of the rating instrument, one may hypothesize that the psychotic state with no symptoms present does not imply the healthy state, which may point to the existence of a genuine transition between the two states.

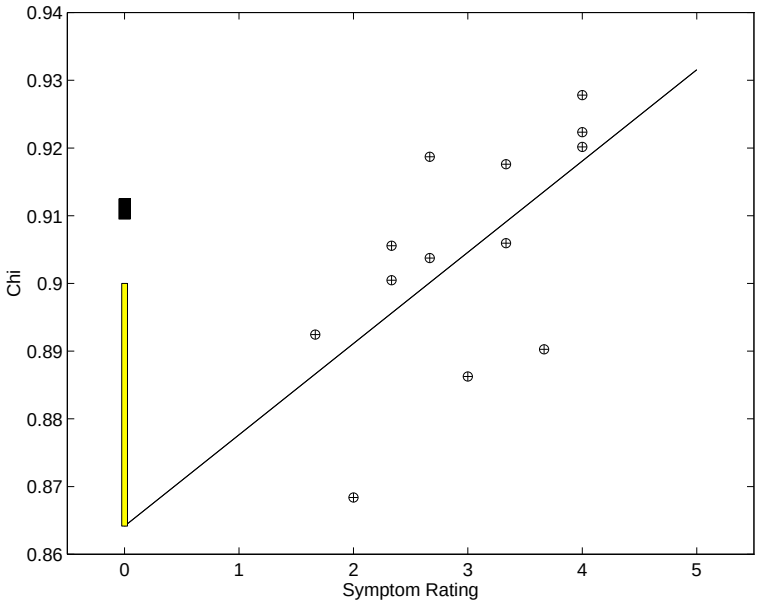

Figure 13.8: An example of symptom rating vs. EEG outcome. The extrapolation to rating zero along the regression line does not meet the average of the healthy probands (black rectangle). This is indicated by the 95% confidence interval (grey bar) for the regression line at this zero point.

References

[1] A. Zehnder, Phys. Rev. B 52, 12858 (1995).

[2] T. Nussbaumer, DISS. ETH, to be published (1998).

[3] K. Segall *et al.*, in the proceedings of LTD7, p. 47, (1997).

[4] S. B. Kaplan et al., Phys. Rev. B 14, p. 4854 (1976).

[5] R.M. Dünki and G.B. Schmid. Unfolding dimension and the search for functional markers in the human electroencephalogram. *Physical Review E*, 57:2115 – 2122, 1998.

[6] G.B. Schmid and R.M. Dünki. Indications of nonlinearity, intraindividual specifity and stability of human EEG: The unfolding dimension. *Physica D*, 93:163 – 190, 1996.

[7] H.H. Jaspers. The ten-twenty electrode system of the international federation. *Electroencephal. Clin. Neurophysiol.*, 10:371 – 375, 1958.

14 Electronic

K. Esslinger

During the 97-98 period of this report, we were occupied principally with repair and further development of existing electronic equipment employed by various groups at our institute.

An alarm system for the detection of mercury was constructed for the group of Prof. W. Kündig (measurement of the gravitational constant) which had to fulfill safety regulations of PSI and SUVA. The device was needed in order to detect changes in the mercury level of two tanks each containing 500 l of mercury. The system for each container consisted of a distance sensor, an optically coupled preamplifier, a signal amplifier with two low impedance outputs (for DVM and ADC/PC), a window discriminator, a logic unit and the alarm. Very stable voltages sources were employed for the distance sensor. Mercury level variations were detected by the distance sensor which produced an output voltage proportional to the level variation. The amplified signals were shown on a digital display and also stored in a PC.

Four separate optical alarm systems were activated for level variations outside of allowed limits (±20 mm) as well as for the loss of the supply voltage and/or the signal lines. The system has been in operation for five months with a long time stability of better than ±0.1 mm.

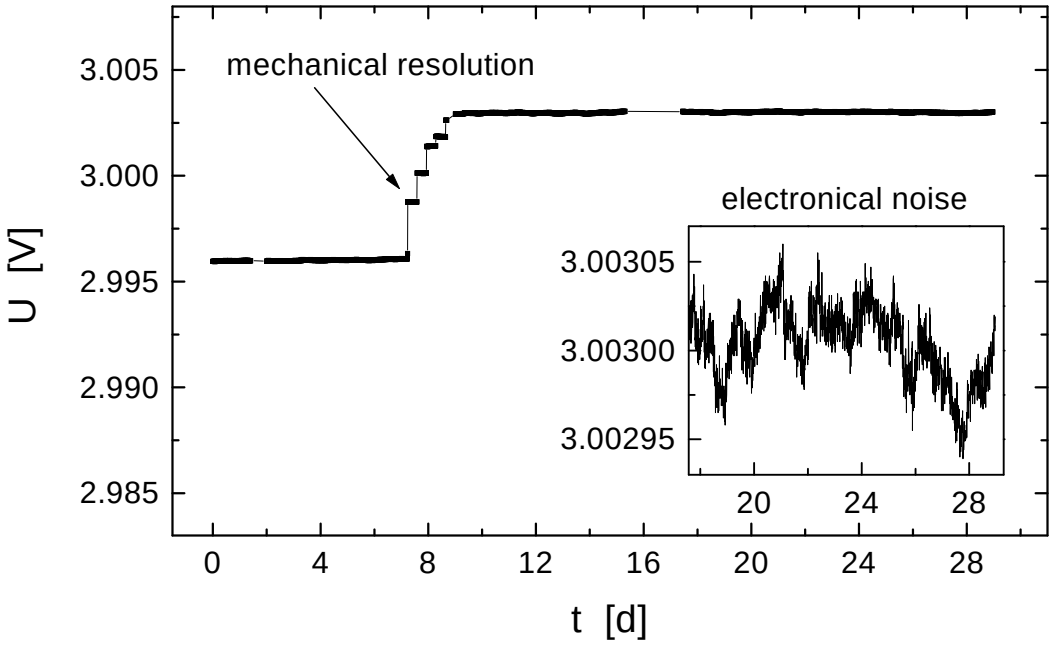

Figure 14.1: *Long time zero voltage fluctuation*

15 Publications

15.1 Research group of Prof. C. Amsler

Articles

- Measurement of the decay distribution of $\eta' \to \pi^+\pi^-\eta$ and evidence for the box anomaly
  A. Abele et al. (Crystal Barrel collaboration)
  Phys. Lett. B 402 (1997) 195
- Study of the $\pi^0\pi^0\eta'$ final state in $\bar{p}p$ annihilation at rest
  A. Abele et al. (Crystal Barrel collaboration)
  Phys. Lett. B 404 (1997) 179
- Momentum Dependence of the Decay $\eta \to \pi^+\pi^-\pi^0$
  A. Abele et al. (Crystal Barrel collaboration)
  Phys. Lett. B 417 (1998) 197
- ρ-ω interference in $\bar{p}p$ annihilation at rest into $\pi^+\pi^-\eta$
  A. Abele et al. (Crystal Barrel collaboration)
  Phys. Lett. B 411 (1997) 354
- Measurement of the $\omega \to \eta\gamma$ decay branching ratio
  A. Abele et al. (Crystal Barrel collaboration)
  Phys. Lett. B 411 (1997) 361
- Decay dynamics of the process $\eta \to 3\pi^0$
  A. Abele et al. (Crystal Barrel collaboration)
  Phys. Lett. B 417 (1998) 193
- Antiproton-proton annihilation into $K_S K_L \pi^0\pi^0$
  A. Abele et al. (Crystal Barrel collaboration)
  Phys. Lett. B 415 (1997) 280
- Antiproton-proton annihilation at rest into $K^0_L K^{\pm}\pi^{\mp}\pi^0$
  - manifestations of isospin interferences
  A. Abele et al. (Crystal Barrel collaboration)
  Phys. Lett. B 415 (1997) 289
- Hadron and Quark Dynamics
  C. Amsler et al. (Nupecc Advisory Group)
  Nucl. Phys. A 622 (1997) 315
- The MUNU experiment, general description
  C. Amsler et al. (MUNU collaboration)
  Nucl. Instrum. and Meth. A 396 (1997) 115
- Experimental status of the scalar and tensor mesons
  S. von Dombrowski
  Proc. LEAP '96 Conf., Dinkelsbühl, 1996, Nucl. Phys. B (Proc. Suppl.) 56A (1977) 125.
- Antiproton-proton anihilation at rest into $K_L K^{\pm}\pi^{\mp}$
  S. Spanier
  Proc. LEAP '96 Conf., Dinkelsbühl, 1996, Nucl. Phys. B (Proc. Suppl.) 56A (1997) 281
- Search for Glueballs at Crystal Barrel
  S. Spanier
  Proc. QCD '96 Conf., Montpellier, 1996, Nucl. Phys. B (Proc. Suppl.) 54A (1997) 362

Articles in press

- Proton-Antiproton Annihilation and Meson Spectroscopy with the Crystal Barrel
  C. Amsler
  Rev. Mod. Phys.
- Exotic $\eta\pi$ State in $\bar{p}d$ Annihilation at Rest into $\pi^-\pi^0\eta p_{spectator}$
  A. Abele et al. (Crystal Barrel collaboration)
  Phys. Lett. B
- $\bar{p}p$ annihilation at rest into $K_L K^{\pm}\pi^{\mp}$
  A. Abele et al. (Crystal Barrel collaboration)
  Phys. Rev. D

Conference reports

- Evidence for $a_0(1450)$ to $K\bar{K}$ in $\bar{p}p$ annihilation at rest
  M. Heinzelmann
  Proc. Hadron '97 Conference, Brookhaven, 1997
- Two-body decays of $f_0(1500)$
  S. Spanier
  Proc. High Energy Physics Conference, Jerusalem, 1997

Invited Lectures

- C. Amsler
  Seminaire, Université de Genève, 24.3.97
  "Mésons exotiques dans l'annihilation nucléon-antinucléon"
- F. Ould-Saada
  Seminar, Saclay, 12.12.97
  "Propriétés électromagnétiques du neutrino et l'expérience du Bugey"
- F. Ould-Saada
  Seminar, Universität Nijmegen, 12.1.98
  "Do neutrinos feel electromagnetism?"
- M. Heinzelmann
  Contributed talk, Hadron '97 Conference, Brookhaven, 26.8.97
  "Evidence for $a_0(1450)$ to $K\bar{K}$ in $\bar{p}p$ annihilation at rest"
- S. Spanier
  Contributed talk, High Energy Physics Conference, Jerusalem, 22.8.97
  "Two-body decays of $f_0(1500)$"
- S. Spanier
  Seminar, SLAC, 6.3.98
  "The scalar groundstate meson and glueball puzzle solution of Crystal Barrel"
- S. Spanier
  Seminar, Carnegie Mellon University, Pittsburgh, 9.3.98
  "Spin-parity analysis in γp"
- S. Spanier
  Seminar, Cornell University, Ithaca, 11.3.98
  "The scalar groundstate meson and glueball puzzle solution of Crystal Barrel"

- S. Spanier
  Seminar, Brookhaven National Laboratory, New York, 13.3.98
  "Search for exotic mesons with Crystal Barrel"

15.2 Research group of Prof. D. Brinkmann

Articles

- The model of singlet–correlated bands for temperatures and doping dependences of Cu(2) Knight shift in blilayered cuprates
  M. Eremin, S. Varlamov, I. Eremin, D. Brinkmann, R. Markendorf, M. Mali, and J. Roos
  Physica B 230–232 (1997) 952
- Electronic spin dynamics in $Ca_{0.85}Sr_{0.15}CuO_2$ – an NMR relaxation study
  F. Raffa, M. Mali, J. Roos, D. Brinkman, M. Matsumura and K. Conder
  Proceedings of 5th Intern. Conf. Materials and Mechanisms of Superconductivity High-Temperature Superconductors (M^2S–HTSC-V), Beijing, 1997, Physica C 282-287 (1997) 1371
- Strong Evidence for an Electronic Crossover around 180 K in $YBa_2Cu_4O_8$, an NMR/NQR study
  A. Suter, M. Mali, J. Roos, D. Brinkmann, and J. Karpinski
  Proceedings of 5th Intern. Conf. Materials and Mechanisms of Superconductivity High-Temperature Superconductors (M^2S–HTSC-V), Beijing, 1997, Physica C 282-287 (1997) 1345
- The paramagnetic phase of the infinite–layer antiferromagnet $Ca_{0.85}Sr_{0.15}CuO_2$ as seen by Cu NMR
  R. Pozzi, M. Mali, M. Matsumura, F. Raffa, J. Roos, and D. Brinkmann
  Phys. Rev. B 56 (1997) 759
- NMR–NQR studies of some key problems in high–temperature superconductors and related antiferromagnets
  D. Brinkmann
  Proc. Specialized Colloque AMPERE/Ramis 97, Poznań, April 1997, Molecular Physics Reports 18/19 (1997) 99
- Electronic crossover in the normal state of $YBa_2Cu_4O_8$
  A. Suter, M. Mali, J. Roos, D. Brinkmann, J. Karpinski and E. Kaldis
  Phys. Rev. B 56 (1997) 5542
- Temperature dependence of the sublattice magnetization in the quasi–2D S=1/2 Heisenberg antiferromagnet La_2CuO_4
  M. Matsumura, M. Mali, J. Roos, and D. Brinkmann
  Phys. Rev. B 56 (1997) 8938
- Spin susceptibility and pseudogap in $YBa_2Cu_4O_8$: An approach via a charge–density–wave instability
  I. Eremin, M. Eremin, S. Varlamov , D. Brinkmann, M. Mali, and J. Roos
  Phys. Rev. B 56 (1997) 11305
- Thermodynamics of the neutral–to–ionic transition as condensation and crystallisation of charge–transfer excitations
  M.H. Lemée-Cailleau, M. Le Cointe, H. Cailleau, T. Luty, F. Moussa, J. Roos, D. Brinkmann, B. Toudic, C. Ayache, and N. Karl
  Phys. Rev. Letters 79 (1997) 1690

Articles in press

- Wide frequency range ^{31}P relaxation in the ionic conductor $LiPO_3$
  S. Berger, J. Roos, A. Zavidonov, and D. Brinkmann
  Solid State Nuclear Magnetic Resonance
- Spin Gap, Electronic Crossover, and Charge Density Waves in Y–Ba–Cu–O Superconductors
  D. Brinkmann
  Zeit. f. Naturforsch.
- Cu(2) NQR studies of $TmBa_2(Cu_{1-x}Zn_x)_4O_8$ superconductors
  A.V. Dooglav, A.V. Egorov, E.V. Krjukov, Yu. A. Sakhratov, M.A. Teplov, D. Brinkmann, M. Mali, J. Roos, J. Karpinski, and E. Kopnin
  Zeit. f. Naturforsch.
- Shape of the Cu(2) NQR spectra in $YBa_2Cu_3O_7$, $TmBa_2Cu_3O_7$ and $TmBa_2Cu_4O_8$: The quantitative analysis in the frame of the motional narrowing model
  A.V. Dooglav, A.V. Egorov, E.V. Krjukov, Yu.A. Sakhratov, M.A. Teplov, D. Brinkmann, M. Mali, J.Roos, J. Karpinski, E. Kopnin, and Yunhui Xu
  JETP

Conference reports

- The paramagnetic phase of the antiferromagnetic $YBa_2Cu_3O_6$ as seen by Cu(2) NMR
  R. Pozzi, M. Mali, J. Roos, D. Brinkmann, A. Erb, and R. Flükiger
  Swiss Workshop on Superconductivity and Novel Metals, Les Diablerets, 29 September - 1 October, 1997
- Isotope effect of the spin gap in $YBa_2Cu_4O_8$ as determined by ^{63}Cu NQR
  F. Raffa, T. Ohno, M. Mali, J. Roos, D. Brinkmann, and K. Conder
  Spring Meeting of Swiss Physical Society, 26/27 February 1998
- Interplane and intraplane coupling in the superconductirng state of $Y_2Ba_4Cu_7O_{15}$
  A. Suter, M. Mali, J. Roos, and D. Brinkmann Spring Meeting of Swiss Physical Society, 26/27 February 1998
- Internes Magnetfeld an Sauerstoffplätzen in antiferromagnetischem $YBa_2Cu_3O_6$
  J. Plaz, M. Mali, J. Roos, D. Brinkmann, and A. Erb Spring Meeting of Swiss Physical Society, 26/27 February 1998
- Pressure dependence of the sublattice magnetization of the antiferromagnetic $Ca_{0.85}Sr_{0.15}CuO_2$
  M. Igarashi, U. Lehmann, M. Mali, J. Roos, and D. Brinkmann
  Spring Meeting of Swiss Physical Society, 26/27 February 1998

Invited Lectures

- D. Brinkmann
  NMR–NQR studies of some key problems in high–temperature superconductors and related antiferromagnets
  Specialized Colloque AMPERE/ RAMIS '97, Poznan, 22–25 April 1997
- D. Brinkmann
  Pseudo gap, electronic crossover, and charge density waves in Y-Ba-Cu-O superconductors
  Kolloquium, MPI für Metallforschung,Stuttgart, 3 June 1997

- D. Brinkmann
  NMR-Streifzug durch die Hochtemperatur-Supraleitung
  Kolloquium, Univ. ZH, 18 June 1997
- D. Brinkmann
  Die Pseudo-Spinlücke in Hochtemperatur-Supraleitern: neue Einsichten mittels NMR-NQR
  Kolloquium, Universität des Saarlandes, Saarbrücken, 26 June 1997
- D. Brinkmann
  Spin gap, electronic crossover and charge density waves in Y-Ba-Cu-O superconductors
  XIV Intern. Symposium on Nuclear Quadrupole Interactions, Pisa, 20 – 25 July 1997
- D. Brinkmann
  NMR-NQR in the normal state of Y-Ba-Cu-O superconductors
  Workshop on *High–temperature superconductivity: Experimental facts, modelling and interpretation* Tellurdie Summer Research Center, Telluride, CO, 3–17 August, 1997
- D. Brinkmann
  Electronic crossover and spin gap in Y-Ba-Cu-O superconductors: new results by NMR-NQR
  Many Body Physics Workshop, Los Alamos Nat. Laboratory, 13–26 August 1997
- D. Brinkmann
  NMR-Untersuchungen zur Spinlücke in Hochtemperatur-Supraleitern
  Physik-Seminar, Universität Stuttgart, 13 January 1998

15.3 Research group of Prof. R. Engfer

Articles

- Improved Limit on the Branching Ratio of $\mu^- \to e^+$ Conversion on Titanium
  J.Kaulard, C.Dohmen, H.Haan, W.Honecker, D.Junker, G.Otter, M.Staringer, P.Wintz, J.Hofmann, W.Bertl, J.Egger, B.Krause, S.Eggli, R.Engfer, Ch.Findeisen, E.A.Hermes, T.Kozlowski, C.B.Niebuhr, M.Rutsche,, H.Pruys, and A.van der Schaaf
  (SINDRUM II Collaboration), Phys. Lett. B **422**, 334 (1998)

Articles in press

- Search for $\mu^- \to e^-$ Conversion on Titanium
  S. Eggli, R. Engfer, Ch. Findeisen, E.A. Hermes, T. Kozlowski, F. Muheim, C.B. Niebuhr, H.S. Pruys, M. Rutsche, and A. van der Schaaf
  in collaboration with: III. Physikalisches Institut B der RWTH Aachen, D-52056, Institut für Teilchenphysik der ETH Zürich, CH-5232 Villigen PSI, and Paul Scherrer Institut, CH-5232 Villigen PSI
  (SINDRUM II Collaboration), Phys. Rev. C.

Conference reports

- Frank Riepenhausen
  Sindrum 2: Searching for $\mu \to e$ Conversion with a Sensitivity of 10^{-14}
  Sixth Conference on the Intersections of Particle and Nuclear Physics (CIPANP97)
  Big Sky, Montana, May 27 - June 2, 1997

Invited Lectures

- R. Engfer
  Graduiertenkolleg an der Universität Tübingen, 19. 12. 1997
  Suche nach einer Leptonenzahl-Verletzung, ein Test von Symmetrien
- R. Engfer
  Seminar, Technische Universität Wien, 24. 3. 1998
  Verbotene μ-Reaktionen, ein Test fundamentaler Symmetrien
- A. van der Schaaf
  Workshop on *A $\mu \to e\gamma$ experiment at PSI?*, PSI, March 16 - 18, 1998
  The Intermediate Imaging Option.
- A. van der Schaaf
  International Symposium on *Lepton and Baryon Number Violation*, ECT, Trento, Italy, April 20 – 25, 1998
  The future of $\mu \to e\gamma$ at PSI.
- P. Wintz
  International Symposium on *Lepton and Baryon Number Violation*, ECT, Trento, Italy, April 20 – 25, 1998
  Results of the SINDRUM II experiment

15.4 Research group of Prof. H. Keller

Articles

- $HgBa_2Ca_{n-1}Cu_nO_{2n+2+\delta}$ and $Y_2Ba_4Cu_{6+n}O_{14+n}$ single crystals: High pressure synthesis and properties
  J. Karpinski, H. Schwer, K. Conder, J. Löhle, R. Molinski, A. Morawski, C. Rossel, P. Bauer, D. Zech, and J. Hofer
  in: *Lecture Notes in Physics - Recent Developments in High Temperature Superconductivity*, ed. J. Klamut *et al.*, Vol. **475** (Springer Verlag, 1996) (pp. 83-102).
- Investigation of vortex behaviour in the organic superconductor κ-(BEDT-TTF)$_2$Cu(SCN)$_2$ using muon spin rotation
  S. L. Lee, F. L. Pratt, S. J. Blundell, C. M. Aegerter, P. A. Pattenden, K. H. Chow, E. M. Forgan, T. Sasaki, W. Hayes, and H. Keller
  Phys. Rev. Lett. **79**, 1563-1566 (1997).
- Using μSR to investigate the vortex lattice in high-temperature superconductors
  C.M. Aegerter and S.L. Lee
  Appl. Mag. Res. **13**, 75-93 (1997).
- Muon-spin rotation studies of the flux lattice in κ-(BEDT-TTF)$_2$Cu(SCN)$_2$
  S. L. Lee, S. J. Blundell, F. L. Pratt, P. A. Pattenden, E. M. Forgan, T. Sasaki, C. M. Aegerter, M. B. Hunt, K. H. Chow, W. Hayes, J. Singleton, H. Keller, and I. M. Savić
  Synth. Met. **85**, 1495-1496 (1997).
- μSR studies of the vortex lattice in high-T_c and other superconductors
  E. M. Forgan, M. T. Wylie, S. Lloyd, M. P. Nutley, S. L. Lee, R. Cubitt, C. Aegerter, H. Keller, and T. W. Li
  Hyperfine Interactions **105**, 61-69 (1997).

- Giant oxygen-isotope shift of the ferromagnetic transition temperature in the colossal magnetoresistive $La_{1-x}Ca_xMnO_{3+y}$: Evidence for Jahn-Teller polarons
  Guo-meng Zhao, K. Conder, H. Keller, and K.A. Müller
  Zeitschrift für Physikalische Chemie **201**, 263-269 (1997).

- Pairing symmetry in single-layer tetragonal $Tl_2Ba_2CuO_{6+\delta}$ from in-plane torque anisotropy
  C. Rossel, M. Willemin, J. Hofer, H. Keller, Z.F. Ren, and J.H. Wang
  Physica C **282-287**, 136-139 (1997).

- EPR evidence of Jahn-Teller polaron formation in $La_{1-x}Ca_xMnO_{3+y}$
  A. Shengelaya, Guo-meng Zhao, H. Keller, and K.A. Müller
  Physica C **282-287**, 190-193 (1997).

- Oxygen isotope effects in the manganites and cuprates: Evidence for polaronic charge carriers
  Guo-meng Zhao, M.B. Hunt, K. Conder, H. Keller, and K.A. Müller
  Physica C **282-287**, 202-205 (1997).

- Flexible cantilevers for torque magnetometry with piezoresistive and capacitive readout
  C. Rossel and M. Willemin
  IBM Technical Disclosure Bulletin **40**, 119-124 (1997).

- Measuring magnetic moments
  University of Zurich and IBM collaboration
  IBM Research **3**, 7-8 (1997).

- *s* and *d* wave symmetry components in high-temperature cuprate superconductors
  K.A Müller and H. Keller
  in *High-Tc Superconductivity 1996: Ten Years after the Discovery*, ed. by E. Kaldis, E. Liarokapis, and K.A. Müller, Series E: Applied Sciences, Vol. **343** (Kluwer Academic Publishers, 1997) (pp. 7-29).

- High pressure crystal growth and properties of
  $HgBa_2Ca_{n-1}Cu_nO_{2n+2+\delta}$, $Sr_{1-x}CuO_2$, $CaCuO_2$ and $Y_2Ba_4Cu_{6+n}O_{14+n}$
  J. Karpinski, H. Schwer, K. Conder, R. Molinski, G. I. Meijer, E. Kopnin, C. Rossel, D. Zech, J. Hofer, A. Wisniewski, and M. Baran
  in *High-Tc Superconductivity 1996: Ten Years after the Discovery*, ed. by E. Kaldis, E. Liarokapis, and K.A. Müller, Series E: Applied Sciences, Vol. **343** (Kluwer Academic Publishers, 1997) (pp. 177-198).

- Novel crossover from a metallic to an insulating ground-state in $(La_{0.5}Nd_{0.5})_{0.67}Ca_{0.33}MnO_3$ by increasing the oxygen mass
  Guo-meng Zhao, H. Keller, J. Hofer, A. Shengelaya, and K.A. Müller
  Solid State Commun. **104**, 57-61 (1997).

- Angular dependent muon-spin rotation on the mixed state of the organic superconductor κ-(BEDT-TTF)$_2$Cu(SCN)$_2$
  C. Ager, S. L. Lee, C. M. Aegerter, F. L. Pratt, S. J. Blundell, S. H. Lloyd, T. Sasaki, E. M. Forgan, and H. Keller
  J. Mag. Mag. Mat. **177 - 181**, 561-562(1998).

- Muon-spin rotation measurements on $Bi_2Sr_2CaCu_2O_{8+\delta}$ in the presence of columnar defects
  S. L. Lee, C. M. Aegerter, C. Ager, E. M. Forgan, S. H. Lloyd, and H. Keller
  J. Mag. Mag. Mat. **177 - 181**, 523-524 (1998).

- Non-local effects and vortex lattice transitions in YNi_2B_2C
  D. McK. Paul, C. V. Tomy, C. M. Aegerter, R. Cubitt, S. H. Lloyd, E. M. Forgan, S. L. Lee, and M. Yethiraj
  Phys. Rev. Lett. **80**, 1517-1520 (1998).
- Angular dependence of the disorder crossover in $Bi_2Sr_2CaCu_2O_{8+\delta}$ from muon spin rotation and torque magnetometry
  C. M. Aegerter, J. Hofer, I. M. Savić, H. Keller, S. L. Lee, C. Ager, S. H. Lloyd, and E. M. Forgan
  Phys. Rev. B **57**, 1253-1258 (1998).
- Piezoresistive cantilever designed for torque magnetometry
  M. Willemin, C. Rossel, J. Brugger, M. Despont, H. Rothuizen, P. Vettiger, J. Hofer, and H. Keller
  J. Appl. Phys. **83**, 1163-1170 (1998).
- Pairing symmetry from in-plane torque anisotropy in $Tl_2Ba_2CuO_{6+\delta}$ thin films
  M. Willemin, C. Rossel, J. Hofer, H. Keller, Z.F. Ren, and J.H. Wang
  Phys. Rev. B **57**, 6137-6144 (1998).
- Doping dependence of superconducting parameters in $HgBa_2CuO_{4+\delta}$ single crystals
  J. Hofer, J. Karpinski, M. Willemin, G. I. Meijer, E. M. Kopnin, R. Molinski, H. Schwer, C. Rossel, and H. Keller
  Physica C **297**, 103-110 (1998).
- Oxygen-isotope effect on the field-induced metal-insulator transition in $Pr_{2/3}Ca_{1/3}MnO_3$
  B. García-Landa, M.R. Ibarra, J.M. De Teresa, G.M. Zhao, and H. Keller
  Solid State Commun. **105**, 567-570 (1998).
- Crystals of $HgBa_2Ca_{n-1}Cu_nO_{2n+2+\delta}$, $Y_2Ba_4Cu_{6+n}O_{14+n}$, $Sr_{1-x}Ca_xCuO_2$ and $Sr_{0.73}CuO_2$, high pressure synthesis and properties
  J. Karpinski, H. Schwer, R. Molinski, G. I. Meijer, K. Conder, E. Kopnin, J. Löhle, C. Rossel, D. Zech, J. Hofer, A. Wisniewski, and R. Puzniak
  in: *Studies of High Temperature Superconductors*, ed. A. Narlikar, Volume **24** (Nova Science Publisher, New York, 1998) (pp. 165-202).

Articles in press

- Ratio of small polarons to free carriers in $La_{2-x}Sr_xCuO_4$ from susceptibility measurements
  K.A. Müller, Guo-meng Zhao, K. Conder and H. Keller
  J.Phys.: Condens. Matter **10**, 291-296 (1998).
- Observation of vortex-lattice melting in twinned $YBa_2Cu_3O_{7-x}$ using neutron small angle scattering
  C. M. Aegerter, S. T. Johnson, W. J. Nuttall, S. H. Lloyd, M. T. Wylie, M. P. Nutley, E. M. Forgan, R. Cubitt, S. L. Lee, D. McK. Paul, M. Yethiraj, and H. A. Mook
  to appear in Phys. Rev. B (1998).
- Oxygen isotope effects in $(La_{0.5}Nd_{0.5})_{0.67}Ca_{0.33}MnO_3$: Relevance of the electron-phonon interaction to the phase segregation
  M. R. Ibarra, G.M. Zhao, J.M. De Teresa, B. García-Landa, Z. Arnold, C. Marquina, P.A. Algarabel, and H. Keller
  to appear in Phys. Rev. B (1998).

- Transition from dimerization to antiferromagnetic order in quasi one-dimensional $Ca_{0.83}CuO_2$
  G.I. Meijer, E.M. Kopnin, M. Willemin, J. Karpinski, H. Schwer, K. Conder, and C. Rossel
  to appear in Europhys. Lett. (1998).
- Microfabricated ultrasensitive piezoresistive cantilevers for torque magnetometry
  J. Brugger, M. Despont, C. Rossel, H. Rothuizen, P. Vettiger, and M. Willemin
  Invited paper, to appear in the *Transducers'97 special volumes of Sensors and Actuators*, submitted to Elsevier Science (1997).
- Single crystals of $HgBa_2Ca_{n-1}Cu_nO_{2n+2+\delta}$ (n=1-5) and layers of $HgBa_2Cu_nO_4$ grown at gas pressure 10 kbar
  J. Karpinski, H. Schwer, E. Kopnin, R. Molinski, G. I. Meijer, K. Conder, J. Hofer, D. Zech
  in: *Proccedings of the International Workshop on Tl- and Hg-based Superconducting Materials*, Cambridge, May 1997, to appear in Journal of Superconductivity (1998).
- Spontaneous magnetization and antiferromagnetic correlations of the CuO_2 chains in $Sr_{0.73}CuO_2$
  A. Shengelaya, G.I. Meijer, J. Karpinski, Guo-meng Zhao, H. Schwer, E.M. Kopnin, C. Rossel, and H. Keller
  to appear in Phys. Rev. Lett. (1998).
- Muon-spin-rotation measurements of the penetration depth in $YBa_2Cu_4O_8$ superconductors
  A. Shengelaya, C.M. Aegerter, S. Romer, H. Keller, P.W. Klamut, R. Dybzinski, B. Dabrowski, J. Klamut, and I.M. Savić
  to appear in Phys. Rev. B (1998).

Conference reports

- Angular dependence of the dimensional crossover in $Bi_2Sr_2CaCu_2O_{8+\delta}$ single crystals by μSR and torque magnetometry
  C. M. Aegerter, S. L. Lee, H. Keller, J. Hofer, E. M. Forgan, I. M. Savić, C. Ager, and S. H. Lloyd
  Vortex Matter Monte Veritá, International Workshop on the inverstigation of Vortex Matter in Superconductors, Ascona, Switzerland, 14-21 June, 1997.
- A μSR and SANS investigation of the phase diagram of $Bi_2Sr_2CaCu_2O_{8+\delta}$
  C. M. Aegerter, S. L. Lee, H. Keller, M. B. Hunt, E. M. Forgan, C. Ager, S. H. Lloyd, S. Romer, D. McK. Paul, and R. Cubitt
  Vortex Matter Monte Veritá', International Workshop on the inverstigation of Vortex Matter in Superconductors, Ascona, Switzerland,14-21 June, 1997.
- Effects of columnar defects on the pinning strength in $Bi_2Sr_2CaCu_2O_{8+\delta}$
  C. M. Aegerter, S. Romer, S. L. Lee, and H. Keller
  Vortex Matter Monte Veritá, International Workshop on the inverstigation of Vortex Matter in Superconductors, Ascona, Switzerland, 14-21 June, 1997.
- High resolution neutron small angle diffraction study of vortex lattice transitions in YNi_2B_2C
  D. McK. Paul, C. V. Tomy, C. M. Aegerter, R. Cubitt, S. H. Lloyd, E. M. Forgan, S. L. Lee, and M. Yethiraj
  Vortex Matter Monte Veritá, International Workshop on the inverstigation of Vortex Matter in Superconductors, Ascona, Switzerland, 14-21 June, 1997.

- Recent muon-spin rotation measurements on the organic superconductor κ-(BEDT-TTF)$_2$Cu(SCN)$_2$
  S. L. Lee, C. M. Aegerter, F. L. Pratt, S. J. Blundell, T. Sasaki, E. M. Forgan, and H. Keller
  Vortex Matter Monte Veritá, International Workshop on the inverstigation of Vortex Matter in Superconductors, Ascona, Switzerland 14-21 June,1997.
- μSR studies of vortex fluctuations in irradiated crystals of $Bi_2Sr_2CaCu_2O_{8+\delta}$
  S. L. Lee, C. M. Aegerter, S. H. Lloyd, E. M. Forgan, and H. Keller
  Vortex Matter Monte Veritá, International Workshop on the inverstigation of Vortex Matter in Superconductors, Ascona, Switzerland, 14-21 June, 1997.
- Flux lattice structures observed in untwinned YBCO using SANS
  E. M. Forgan, S. T. Johnson, S. H. Lloyd, S. L. Lee, R. Cubitt, C. M. Aegerter, D. McK. Paul, and M. Yethiraj
  Vortex Matter Monte Veritá, International Workshop on the inverstigation of Vortex Matter in Superconductors, Ascona, Switzerland, 14-21 June, 1997.
- Flux lattice melting in twinned and untwinned YBCO observed by SANS
  E. M. Forgan, S. T. Johnson, S. H. Lloyd, S. L. Lee, R. Cubitt, C. M. Aegerter, D. McK. Paul, and M. Yethiraj
  Vortex Matter Monte Veritá, International Workshop on the inverstigation of Vortex Matter in Superconductors, Ascona, Switzerland ,14-21 June, 1997.
- Investigation on superconducting thin films by high sensitivity torque magnetometry
  M. Willemin, C. Rossel, J. Hofer, and H. Keller
  European Conference on Applied Superconductivity (EUCAS), Eindhoven, NL, 30 June - 3 July, 1997.
- High resolution neutron small angle diffraction study of vortex lattice transitions in YNi_2B_2C
  C. M. Aegerter, D. McK. Paul, C. V. Tomy, R. Cubitt, S. H. Lloyd, E. M. Forgan, S. L. Lee, and M. Yethiraj
  5th PSI Summer School on Neutron Scattering: 'Cold Neutrons: Large Scales - High Resolution', Zuoz, Switzerland, 9-15 August, 1997.
- Effects of columnar defects on the pinning strength in $Bi_2Sr_2CaCu_2O_{8+\delta}$
  S. Romer, C. M. Aegerter, S. L. Lee, and H. Keller
  Swiss Workshop on Superconductivity and Novel Metals, Les Diablerets, Switzerland, 29 September - 1 October, 1997.
- Piezoresistive cantilever designed for torque magnetometry
  M. Willemin, C. Rossel, J. Brugger, M. Despont, H. Rothuizen, P. Vettiger, J. Hofer, and H. Keller
  Swiss Workshop on Superconductivity and Novel Metals, Les Diablerets, Switzerland, 29 September - 1 October, 1997.
- Doping dependence of superconducting parameters in $HgBa_2CuO_{4+\delta}$ single crystals
  J. Hofer, Guo-meng Zhao, J. Karpinski, M. Willemin, G. I. Meijer, E. M. Kopnin, R. Molinski, H. Schwer, C. Rossel, and H. Keller
  Swiss Workshop on Superconductivity and Novel Metals, Les Diablerets, Switzerland, 29 September - 1 October, 1997.
- High pressure synthesis and properties of $HgBa_2Ca_{n-1}Cu_nO_{2n+2+\delta}$ (n=1-5), infinite chain $A_{1-x}CuO_2$ (A:Sr,Ca,Ba) and infinit layer $Sr_{1-x}Ca_xCuO_2$ compounds
  J. Karpinski, H. Schwer, R. Molinski, G. I. Meijer, E. Kopnin, K. Conder, C. Rossel,

J. Hofer, M. Willemin, A. Shengelaya, and H. Keller
Swiss Workshop on Superconductivity and Novel Metals, Les Diablerets, Switzerland, 29 September - 1 October, 1997.

- Spontaneous magnetization and antiferromagnetic correlations of the CuO_2 chains in $Sr_{0.73}CuO_2$
A. Shengelaya, G.I. Meijer, J. Karpinski, Guo-meng Zhao, H. Schwer, E.M. Kopnin, C. Rossel, and H. Keller
Swiss Workshop on Superconductivity and Novel Metals, Les Diablerets, Switzerland, 29 September - 1 October, 1997.
- New sensors for torque magnetometry
M. Willemin, C. Rossel, J. Brugger, H. Rothuizen, P. Vettiger, J. Hofer, and H. Keller
Swiss Physical Society Meeting, Bern, 26-27 February, 1998.
- Doping dependence of superconducting parameters in $HgBa_2CuO_{4+\delta}$ single crystals
J. Hofer, Guo-meng Zhao, J. Karpinski, M. Willemin, G. I. Meijer, E. M. Kopnin, R. Molinski, H. Schwer, C. Rossel, and H. Keller
Swiss Physical Society Meeting, Bern, 26-27 February, 1998.

Invited Lectures

- H. Keller
Ringvorlesung
Volkshochschule Zürich, 13 January, 1997
"Physik des Lichts II: Von der Glühlampe zum Laser"
- H. Keller
Seminar
Kazan State University, Kazan, Russia, September 1997
"Probing high-temparature superconductivity' with positive muons"
- C. M. Aegerter
Invited talk
Solid State Physics Colloquium, Laboratoire CRISMAT, Caen France, 10 June, 1997
"Le diagramme de phase du réseau de vortex dans $Bi_2Sr_2CaCu_2O_{8+\delta}$ investigué à l'aide de rotation de spin de muon et de la diffraction de neutrons à petit angle"
- C. M. Aegerter
Invited talk
Swiss Workshop on Superconductivity and Novel Metals, Les Diablerets, Switzerland, 29 September - 1 October, 1997
"SANS investigation of vortex lattice melting in twinned $YBa_2Cu_3O_{7-x}$"
- A. Schilling
Invited talk
Swiss Workshop on Superconductivity and Novel Metals, Les Diablerets, Switzerland, 29 September, 1997
"Anisotropic latent heat of vortex-lattice melting in untwinned $YBa_2Cu_3O_7$"
- A. Shengelaya
Invited talk
International Laboratory of High Magnetic Fields and Low Temperatures, Wroclaw, Poland, December, 1997
"Muon-spin-rotation measurements of the penetration depth in $YBa_2Cu_4O_8$ superconductors"

- M. Willemin
  Invited lecture
  Institut jurassien des sciences, des lettres et des arts, Tramelan, 25 September, 1996.
  Cahiers de l'Institut jurassien des sciences, des lettres et des arts **4**, 23 (1997). "Les galaxies et leur évolution"
- Guo-meng Zhao
  Invited talk
  Electron-Phonon Interaction and Phase Transition, Erice, Italy, June 9-15, 1997
  "Oxygen isotope effects in the magnetoresistive manganites and superconductive cuprates: Evidence for polaronic charge carriers"
- Guo-meng Zhao
  Invited talk
  International School of Physics "Erico Fermi" Course: Models and Phenomenology for Conventional and High-Temperature Superconductivity, Varenna, Italy, 24 June - 4 July, 1997
  "Oxygen isotope effects in the manganites and cuprates: Evidence for polaronic charge carriers"
- Guo-meng Zhao
  Invited talk
  Dynamical Properties of Solids (DYPROSO XXVI), Davos, Switzerland, 21-26 September, 1997
  "Giant oxygen isotope effects in the CMR manganites"
- Guo-meng Zhao
  Invited talk
  Swiss Workshop on Superconductivity and Novel Metals, Les Diablerets, Switzerland, 29 September - 1 October, 1997
  "Evidence for polaronic supercarriers in the cuprate $La_{2-x}Sr_xCuO_4$"

15.5 Research group of Prof. W. Kündig

Articles

- Gravitational Constant Measured by Means of a Beam Balance
  J. Schurr, F. Nolting, and W. Kündig
  Phys. Rev. Lett. **80**, 1142 (1998).

Articles in press

- Direct Measurements of the Neutrino Masses
  E. Holzschuh
  In Neutrino physics, 2nd edition, ed. K. Winter, Cambridge University Press.
- A new experiment to measure G by means of a beam balance
  F. Nolting, J. Schurr, and W. Kündig
  Proceedings of the Eigth Marcel Grossman Meeting in General Relativity, Jerusalem, Israel June 1997.

Conference reports

- A new experiment to measure G by means of a beam balance, presented by F. Nolting, Eigth Marcel Grossman Meeting in General Relativity, Jerusalem, Israel June 1997.

- Präzisionsmessung der Gravitationskonstante, presented by J. Schurr, spring meeting of the German Physical Society, Regensburg März 1998.

Invited Lectures

- W. Kündig
  Experimente zur Gravitation
  Physikalische Gesellschaft Zürich, 29. Januar 1998

15.6 Research group of Prof. P. F. Meier

Articles

- J. M. Singer, M. Pedersen, T. Schneider,
  From BCS-like superconductivity to condensation of local pairs:
  A numerical study of the attractive Hubbard model.
  Physica B **230-232**, 955 (1997).
- J. Schneider, M. Dankesreiter, W. Fettes, I. Morgenstern, M. Schmid, J. M. Singer,
  Search-space smoothing for combinatorial optimization problems.
  Physica A **243**, 77 (1997).
- T. Schneider and J. M. Singer,
  Universal Critical Quantum Properties of Cuprate Superconductors.
  in: *Fluctuation Phenomena in High Temperature Superconductors*,
  A. Ausloos and A. Varlamov (Eds.), Kluwer Academic, Dordrecht, 1997
- T. Schneider and J. M. Singer,
  Crossover and quantum critical phenomena in high-temperature superconductors.
  Europhysics Letters **40**, 79 (1997).
- J. M. Singer and P. F. Meier,
  Hubbard model predictions for the Knight shift in cuprates.
  Physica C **282-287**, 1795 (1997).
- E. Stoll, C. Stern, J. M. Singer, P. Stucki,
  Doping high T_c superconductors with oxygen and metallic atoms: A molecular dynamics study.
  J. Mater. Res. **12**, 2901 (1997).
- P. Gravila,
  Ph.D. thesis,
  University of Zürich (1997)
- N. Paschedag, H. U. Suter, P. F. Meier,
  Comparative calculations on the hyperfine parameters of bond-centered impurities in silicon using high-level ab initio techniques.
  Hyperfine Interactions **105**, 351 (1997).
- H. U. Suter, E. P. Stoll, P. Hüsser, S. Schafroth, P. F. Meier,
  A theoretical study of the local electronic structure of two adjacent Cu-O-planes in $YBa_2Cu_3O_7$.
  Physica C **282-287**, 1639 (1997).
- P. Hüsser, S. Schafroth, E. Stoll, H. U. Suter, P. F. Meier,
  First-Principles Calculation of Electric-Field Gradients at the Cu Sites in $YBa_2Cu_3O_7$.
  Helv. Phys. Acta **70**, Separanda 2 (1997), S25.

- E. Stoll, C. Stern, P. Stucki,
  A User Project: System Architecture for Parallel Particle Simulation in Real-Time: Model Calculation and Visualization in Molecular Dynamics.
  CrosSCutS, **6**(1), 26 (1997).
- C. Stern, P. Stucki, E. Stoll,
  A toolkit for interactive molecular dynamics simulation and visualization,
  Nuclear Instruments and Methods in Physics Research Section A: Accelerators, Spectrometers, Detectors and Associated Equipment, **389**(1-2), 69 (1997).
- Erich Stoll,
  A fast cluster counting algorithm for percolation on and off lattices,
  Computer Physics Communications, **109**(1), 1 (1998).
- R. M. Dünki and G. B. Schmid,
  Unfolding dimension and the search for functional markers in the human electroencephalogram,
  Physical Review E **57**, 2115 (1998).
- G. B. Schmid and R. M. Dünki,
  Indications of nonlinearity, intraindividual specifity and stability of human EEG: The unfolding dimension,
  Physica D **93**, 163 (1996).

Articles in press

- J. M. Singer, T. Schneider, M. H. Pedersen,
  On the Phase Diagram of the Attractive Hubbard Model:
  Crossover and Quantum Critical Phenomena
  to appear in European Physical Journal B **1**, 1998.
- J. Schneider, I. Morgenstern, J. M. Singer,
  Bouncing towards the optimum – Improving results of Monte Carlo optimization algorithms
  to appear in Physical Review E, 1998.
- T. Schneider and J. M. Singer,
  A Phase Transition Approach to High Temperature Superconductivity
  "Troisieme Cycle de la Physique en Suisse Romande",
  semestre d'hiver 1997-98, Ecole Polytechnique Federal Lausanne.
- P. Hüsser, E.P. Stoll, H.U. Suter, and P.F. Meier,
  First-Principles Calculation of Electric-Field Gradients at the Cu Sites in $YBa_2Cu_3O_7$,
  to appear in Physica C (1998).

Invited Lectures

- R. M. Fuchslin,
  Physics Seminary, Univ. Zuerich, November 1997.
- R. M. Fuchslin,
  18th μSR seminar in Repino, Russia.
- R. M. Fuchslin,
  CAP Seminar, University of Zurich, 1997.

- P. F. Meier,
  Telluride Summer Research Center Workshop on High Temperature Superconductivity,
  Telluride, CO, USA, August 1997.
- P. F. Meier,
  Dept. of Psychology, University of British Columbia, Vancouver, CA, Februar 1998.
- J. M. Singer,
  Aspen Winter Conference on Strongly Correlated Systems,
  Aspen, CO, USA, Januar 1997.
- J. M. Singer,
  Telluride Summer Research Center Workshop on High Temperature Superconductivity,
  Telluride, CO, USA, August 1997.
- J. M. Singer,
  Swiss Workshop on Superconductivity, Les Diablerets, September 1997.
- J. M. Singer,
  IRRMA und Dept. of Physics, Colloquium, EPFL Laussanne, Januar 1998.

15.7 Research group of Prof. J. Osterwalder

Articles

- Suppressed forward scattering in photoelectron holography
  T. Greber and J. Osterwalder
  Prog. in Surf. Sci. 53 (1996) 163
- Fermi surface mapping by photoemission
  J. Osterwalder
  Surf. Rev. Lett. 4 (1997) 391
- Angle–scanned photoemission on Bi–type high Tc superconductors: Fermi surfaces and thin metal films
  P. Aebi, P. Schwaller, J. Osterwalder, R. Fasel, H. Berger, C. Beeli, and L. Schlapbach
  Proceedings of ECASIA 95, 6th European Conference on Applications of Surface and Interface Analysis, H. J. Mathieu, B. Reihl, D. Briggs, eds. (John Wiley & Sons, Chichester 1997), p. 733
- Surface alloy formation and interdiffusion in $\sqrt{5}$x$\sqrt{5}$R27 – Yb/Al(001): a combined low–energy electron diffraction and photoelectron diffraction study
  R. Fasel, M. Gierer, H. Bludau, P. Aebi, J. Osterwalder, and L. Schlapbach
  Surf. Sci. 374 (1997) 104
- Electronic and atomic structure of $\sqrt{5}$x$\sqrt{5}$R27 – Yb/Al(001)
  R. Fasel, P. Aebi, T. Greber, J. Osterwalder, and L. Schlapbach
  Surf. Rev. Lett. 4 (1997) 1155
- Real–space mapping of the surface atomic environment via low–energy ion scattering spectroscopy
  R. G. Agostino, P. Aebi, J. Osterwalder, J. Hayoz, and L. Schlapbach
  Surf. Sci. 384 (1997) 36
- Structural and spectroscopic investigation of the Yb/Al(001) interface in the submonolayer coverage range
  R. Fasel, P. Aebi, J. Osterwalder, and L. Schlapbach
  Surf. Sci. 394 (1997) 129

- The temperature–dependent electronic structure of nickel metal
  T. J. Kreutz
  PhD Thesis, Physik-Institut, Universität Zürich, 1997
- Photoemission above the Fermi level: the top of the minority d band in nickel
  T. Greber, T. J. Kreutz, and J. Osterwalder
  Phys. Rev. Lett. 79 (1997) 4465
- A photoelectron spectrometer for k–space mapping above the Fermi level
  T. Greber, O. Raetzo, T. J. Kreutz, P. Schwaller, W. Deichmann, E. Wetli, and J. Osterwalder
  Rev. Sci. Instrum. 68 (1997) 4549
- Doping–dependent electronic structure of cuprates: a photoemission study
  P. Schwaller
  PhD Thesis, Physik-Institut, Universität Zürich, 1997
- Semiclassical theory for the interaction dynamics of laser light and sodium atoms including the hyperfine structure
  S. Dangel and R. Holzner
  Phys. Rev. A 56 (1997) 3937
- Dynamics of light pattern formation for polarized laser beams propagating through sodium vapor
  S. Dangel and R. Holzner
  J. Opt. Soc. Am. B 15 (1998) 594
- Nonlinear dynamics of laser light pattern formation in sodium vapor
  S. Dangel
  PhD Thesis, Physik-Institut, Universität Zürich, 1997
  This thesis has received the LEICA price 1997 for excellent scientific work in optics related physics.
- Optical pumping–induced spatio–temporal modifications to propagation, polarization and intensity of laser beams in sodium vapor
  R. Holzner and S. Dangel
  Quantum Semiclass. Opt. 10 (1998) R1
- Observation of magnetic–field–induced laser beam deflection in sodium vapor
  R. Holzner, P. Eschle, S. Dangel, R. Richard, H. Schmid, U. Rusch, B. Röhricht, R. J. Ballagh, A. W. McCord, and W. J. Sandle
  Phys. Rev. Lett. 78 (1997) 3451
- Ablenkung von Licht durch Licht
  R. Holzner
  Neue Zürcher Zeitung, 31.12.1997, p. 22
- Charge–transfer induced particle emission in Gas Surface Reactions
  T. Greber
  Surf. Sci. Rep. 232 (1997) 1
- Verfahren zur Einstellung des Sauerstoffgehaltes in einem sauerstoffhaltigen Volumenbereich eines Festkörpers
  P. Schwaller, T. Greber und J. Osterwalder
  CH-Pat. Ges. No:2510/97
- Comparison of maximal left ventricular intramyocardial artery lumen diameter in 2 aneurysmectomy specimen after TMR and 44 control patients

W. Schweitzer, S. Dangel, M. Schäpman, M. Wagen , D. Maass , S. Cordner, and Th. Hardmeier
Lasermedizin 13 (1998) 83

Articles in press

- High–resolution photoemission study of hcp-Co(0001)
  E. Wetli, T. J. Kreutz, H. Schmid, T. Greber, and J. Osterwalder
  Surf. Sci.
- Complete k–space mappings of cuprates at different doping levels
  P. Schwaller, T. Greber, H. Berger, and J. Osterwalder
  J. Phys. Chem. Solids
- Angle–scanned photoemission: Fermi surface mapping and structural determination
  P. Aebi, R. Fasel, D. Naumovic, J. Hayoz, Th. Pillo, M. Bovet, R. G. Agostino, L. Patthey, L. Schlapbach, F. P. Gil, H. Berger, T. J. Kreutz, and J. Osterwalder
  Surf. Sci.
- Semiconductor–metal transition of the single domain K/Si(100)-(2x1) by Fermi surface determination
  J. A. Martin-Gago, M. C. Asensio, P. Aebi, R. Fasel, D. Naumovic, J. Osterwalder, C. Refolio, J. M. Lopez-Sancho, and J. Rubio
  Phys. Rev. B
- State and orientation dependent N_2 emission in the $N_2O + Cs$ reaction
  M. Brandt, T. Greber, N. Böwering, and U. Heinzmann
  Surf. Sci.
- Copper Electrodeposition onto Alkanothiolate Layers
  O. Cavalleri, A. M. Bittner, H. Kind, K. Kern, and T. Greber
  Z. Phys. Chem.

Conference reports

- Spatio–temporal light–pattern formation due to optical pumping of circularly polarized laser beams propagating through sodium vapor
  R. Holzner and S. Dangel
  First Conference on Polarization Effects in Lasers and Spectroscopy, University of Toronto, Canada, May 24-28, 1997
- Deposition and laser–induced desorption of sodium atoms on plain glass and on glass coated by a self–assembling monolayer of organic molecules
  R. Holzner, H. Neff, and J. Osterwalder
  Conference on Surface and Interface Optics, Ålesund, Norway, June 1-4, 1997
- Probing the heat of hot adatoms by exoemission
  T. Greber
  Poster, Gordon Research Conference on Dynamics at Surfaces, Andover, New Hampshire, 12.8.97
- New modes of data acquisition in ARUPS: studying the temperature dependent electronic structure of nickel
  T. J. Kreutz
  7th International Conference on Electron Spectroscopy, Chiba, Japan, 11.9.97

- Measuring band dispersion of thermally excited electrons
  J. Osterwalder
  17th European Conference on Surface Science (ECOSS-17), Enschede, Holland, 18.9.97
- High-resolution photoemission study of hcp-Co(0001)
  E. Wetli
  Poster, 17th European Conference on Surface Science (ECOSS-17), Enschede, Holland, 18.9.97
- Subsurface oxygen on Rh(111): an x–ray photoelectron diffraction study
  J. Wider
  Poster, 17th European Conference on Surface Science (ECOSS-17), Enschede, Holland, 18.9.97
- Doping–dependent electronic structure of cuprates: a photoemission study
  P. Schwaller
  Poster, Spectroscopy on Novel Superconductors, Cape Cod, Massachussetts, 14.-18.9.97
- Evolution of the Fermi surface of BiSrCaCuO (2212) with doping
  P. Schwaller
  Swiss Workshop on Superconductivity and Novel Metals, Les Diablerets, 29.9.-1.10. 1997
- Controlled underdoping of cuprates by UV radiation
  P. Schwaller
  Jahrestagung der Schweizerischen Physikalischen Gesellschaft, Bern, 27.2.98
- Subsurface Sauerstoff auf Rh(111): eine XPD Untersuchung
  J. Wider
  Jahrestagung der Schweizerischen Physikalischen Gesellschaft, Bern, 27.2.98
- Wachstum und Charakterisierung einer Monolage h-BN auf Ni(111)
  W. Auwärter
  Jahrestagung der Schweizerischen Physikalischen Gesellschaft, Bern, 27.2.98

Invited Lectures

- T. J. Kreutz
  Temperaturabhängige Untersuchungen der elektronischen Struktur von metallischem Nickel mittels winkelgerasterter Photoelektronenspektroskopie
  Seminar, Physik-Institut der Universität Basel, 22.4.97
- S. Dangel
  Dynamik der Musterbildung von polarisierten Laserstrahlen in Natriumdampf
  Promotionsvortrag, Physik-Institut, Universität Zürich, 22.5.97
- T. Greber
  Exoemission als Probe für heissen Sauerstoff auf Oberflächen
  Gruppenseminar Physikalische Chemie der Universität Zürich, 3.6.97
- E. Wetli
  Femtosekunden-Laser-Einsatz in einem Elektronenstreuexperiment
  Gruppenseminar Physikalische Chemie der Universität Zürich, 10.6.97
- J. Osterwalder
  Photoelektronenbeugung zur Untersuchung von Adsorbatstrukturen
  Kolloquium, Fachbereich Physik der Universität Kassel, 19.6.97

- J. Osterwalder
  Photoelektronenbeugung zur Untersuchung von Adsorbatstrukturen
  Invited Talk, International Conference on Auger Spectroscopy and Electronic Structure (IWASES), Jülich, 23-26.6.97
- S. Dangel
  Simulating the dynamics of laser beam pattern formation on the SX–4
  Seminar, CSCS, Manno, 1.9.97
- S. Dangel
  Simulation der Musterbildungsdynamik von Laserlicht in Natriumdampf
  Seminar, Physikinstitut, Universität Münster, 13.10.97
- S. Dangel
  Dynamik der Musterbildung von polarisierten Laserstrahlen in Natriumdampf
  Generalversammlung der Schweizerischen Gesellschaft für Optik und Elektronenmikroskopie (SGOEM), Entgegennahme des "Leica Preises 1997", Universität Zürich, 17.10.97
- P. Schwaller
  Dotierungsabhängigkeit der Fermifläche von Kupraten untersucht mit Photoemissions-experimenten
  Promotionsvortrag, Physik-Institut, Universität Zürich, 30.10.97
- J. Osterwalder
  Photoelectron diffraction and Fermi surface mapping
  Blockkurs in Elektronenspektroskopie, Universität Ulm, 7.11.97
- P. Schwaller
  Doping–dependent electronic structure of cuprates Festkörperseminar, Universität Neuenburg, 25.11.97
- S. Dangel
  Semiklassische Theorie der Wechselwirkung zwischen Laserlicht und Natriumdampf mit Hyperfeinstruktur
  Seminar, Institut für angewandte Physik, Universität Konstanz, 12.12.97
- T. Greber
  Nichtadiabatische Gas-Oberflächenreaktionen: O_2 und N_2O mit Alkalimetallen
  Seminar, Physikalische Chemie der Universität Zürich, 18.12.97
- P. Schwaller
  Dotierungsabhängige elektronische Struktur von Kupraten
  Festkörperseminar, Université de Fribourg, 12.1.98
- T. J. Kreutz
  The temperature–dependent magnetism of nickel studied by photoemission experiments
  Festkörperseminar, Université de Fribourg, 26.1.98
- T. Greber
  Über Bornitride, die polaren Schwestern von Diamant, Graphit und Russ – oder das Photoemissionsexperiment an der Aussenstation Irchel
  Aerosol-Seminar, ETH Zürich, 28.1.98
- P. Schwaller
  The doping dependence of the electronic structure of cuprates
  Seminar, Institut de Physique Appliqué, EPF Lausanne, 29.1.98

- J. Osterwalder
  Struktur atomarer und molekularer Monolagen aus Photoemissionsexperimenten
  Kolloquium, Erich-Schmid-Institut der Oesterreichischen Akademie der Wissenschaften, Leoben, 5.3.98

15.8 Research group of Prof. P. Truöl

Articles

- Experiment E865 at BNL: A search for the decay $K^+ \to \pi^+\mu^+e^-$
  Stefan Pislak
  Thesis Universität Zürich (1997)
- Observation of Events at very High Q^2 in ep collisions at HERA
  H1-Collaboration**, C. Adloff et al.
  DESY 97 – 024
  Zeitschrift für Physik **C74** (1997), 191 - 205
- Diffraction Dissociation in Photoproduction at HERA
  H1-Collaboration**, C. Adloff et al.
  DESY 97 – 009
  Zeitschrift für Physik **C74** (1997), 221 - 235
- A Measurement of the Proton Structure Function $F_2(x, Q^2)$ at Low x and Low Q^2 at HERA
  H1-Collaboration**, C. Adloff et al.
  DESY 97 – 042
  Nuclear Physics **B497** (1997), 3 - 30
- Bose-Einstein Correlations in Deep Inelastic ep Scattering at HERA
  H1-Collaboration**, C. Adloff et al.
  DESY 97 – 075
  Zeitschrift für Physik **C75** (1997), 437 - 451
- Proton Dissociative ρ and Elastic Φ Electroproduction at HERA
  H1-Collaboration**, C. Adloff et al.
  DESY 97 – 082
  Zeitschrift für Physik **C75** (1997), 607 - 618
- Photoproduction of K^0 and Λ at HERA and a Comparison to Deep Inelastic Scattering
  H1-Collaboration**, C. Adloff et al.
  DESY 97 – 095
  Zeitschrift für Physik **C76** (1997), 213 - 221
- Measurement of Event Shape Variables in Deep Inelastic ep Scattering
  H1-Collaboration**, C. Adloff et al.
  DESY 97 – 098
  Physics Letters **B406** (1997), 256 - 270
- Evolution of ep Fragmentation and Multiplicity Distributions in the Breit Frame
  H1-Collaboration**, C. Adloff et al.
  DESY 97 – 108
  Nuclear Physics **B504** (1997), 3 - 23
- Inclusive Measurement of Diffractive Deep-Inelastic ep Scattering
  H1-Collaboration**, C. Adloff et al.
  DESY 97 – 158
  Zeitschrift für Physik **C76** (1997), 613 - 629

- Measurement of the Inclusive Di-Jet Cross Section in Photoproduction and Determination of an Effective Parton Distribution in the Photon
  H1-Collaboration**, C. Adloff et al.
  DESY 97 – 164
  The European Physical Journal **C1** (1998), 97 -107
- Low Q^2 Jet Production at HERA and Virtual Photon Structure
  H1-Collaboration**, C. Adloff et al.
  DESY 97 – 179
  Physics Letters **B415** (1997), 418 - 434
- Thrust Jet Analysis in Deep-Inelastic Large-Rapidity-Gap Events
  H1-Collaboration**, C. Adloff et al.
  DESY 97 – 210
  The European Physical Journal **C1** (1998), 495 - 507

Articles in press

- Photoproduction of $\Psi(2s)$ Mesons at HERA
  H1-Collaboration**, C. Adloff et al.
  DESY 97 – 228
  Physics Letters **B** (1997), in print

Conference reports

- Muon Capture on ^{11}B: Pseudoscalar Coupling and the Hyperfine Effect
  V. Wiaux, J. Deutsch, J. Govaerts, J. Lehmann, T. Otto, R. Prieels, V. Brudanin, V. Egorov, J. Rak, K. Lou, C. Petitjean, and P. Truöl
  Proc. NAN97, Dubna, Russia (July 1997).

Invited Lectures

- Heavy quark and jet production by real and virtual photons
  F. Sefkow
  26. 6. 1997
  17. Int. Conf. on Physics in Collision, Bristol, England.
- Physik mit schweren Quarks in Photoproduktion bei HERA
  M. zur Nedden
  12. 9. 1997
  29. Herbstschule für Hochenergiephysik Maria Laach, Deutschland
- Messungen der Gluonverteilung im Proton
  D. Müller
  24. 3. 1998
  Gruppenvortrag, Tagung der Deutschen Physikalischen Gesellschaft, Freiburg, März 1998

** H1-collaboration (status of March 1998, the actual author list may differ from paper to paper somewhat):

C. Adloff[34], M. Anderson[22], V. Andreev[25], B. Andrieu[28], V. Arkadov[35], C. Arndt[11], I. Ayyaz[29], A. Babaev[24], J. Bähr[35], J. Bán[17], P. Baranov[25], E. Barrelet[29], R. Barschke[11], W. Bartel[11], U. Bassler[29], P. Bate[22], M. Beck[13], A. Beglarian[11,40], O. Behnke[11],

H.-J. Behrend[11], C. Beier[15], A. Belousov[25], Ch. Berger[1], G. Bernardi[29], G. Bertrand-Coremans[4], P. Biddulph[22], J.C. Bizot[27], V. Boudry[28], A. Braemer[14], W. Braunschweig[1], V. Brisson[27], D.P. Brown[22], W. Brückner[13], P. Bruel[28], D. Bruncko[17], J. Bürger[11], F.W. Büsser[12], A. Buniatian[32], S. Burke[18], G. Buschhorn[26], D. Calvet[23], A.J. Campbell[11], T. Carli[26], E. Chabert[23], M. Charlet[4], D. Clarke[5], B. Clerbaux[4], S. Cocks[19], J.G. Contreras[8], C. Cormack[19], J.A. Coughlan[5], M.-C. Cousinou[23], B.E. Cox[22], G. Cozzika[9], J. Cvach[30], J.B. Dainton[19], W.D. Dau[16], K. Daum[39], M. David[9], A. De Roeck[11], E.A. De Wolf[4], B. Delcourt[27], C. Diaconu[23], M. Dirkmann[8], P. Dixon[20], W. Dlugosz[7], K.T. Donovan[20], J.D. Dowell[3], A. Droutskoi[24], J. Ebert[34], G. Eckerlin[11], D. Eckstein[35], V. Efremenko[24], S. Egli[37], R. Eichler[36], F. Eisele[14], E. Eisenhandler[20], E. Elsen[11], M. Enzenberger[26], M. Erdmann[14], A.B. Fahr[12], L. Favart[4], A. Fedotov[24], R. Felst[11], J. Feltesse[9], J. Ferencei[17], F. Ferrarotto[32], M. Fleischer[8], G. Flügge[2], A. Fomenko[25], J. Formánek[31], J.M. Foster[22], G. Franke[11], E. Gabathuler[19], K. Gabathuler[33], F. Gaede[26], J. Garvey[3], J. Gayler[11], M. Gebauer[35], R. Gerhards[11], S. Ghazaryan[11,40], A. Glazov[35], L. Goerlich[6], N. Gogitidze[25], M. Goldberg[29], I. Gorelov[24], C. Grab[36], H. Grässler[2], T. Greenshaw[19], R.K. Griffiths[20], G. Grindhammer[26], C. Gruber[16], T. Hadig[1], D. Haidt[11], L. Hajduk[6], T. Haller[13], M. Hampel[1], V. Haustein[34], W.J. Haynes[5], B. Heinemann[11], G. Heinzelmann[12], R.C.W. Henderson[18], S. Hengstmann[37], H. Henschel[35], R. Heremans[4], I. Herynek[30], K. Hewitt[3], K.H. Hiller[35], C.D. Hilton[22], J. Hladký[30], D. Hoffmann[11], T. Holtom[19], R. Horisberger[33], V.L. Hudgson[3], S. Hurling[11], M. Ibbotson[22], Ç. İşsever[8], H. Itterbeck[1], M. Jacquet[27], M. Jaffre[27], D.M. Jansen[13], L. Jönsson[21], D.P. Johnson[4], H. Jung[21], M. Kander[11], D. Kant[20], U. Kathage[16], J. Katzy[11], H.H. Kaufmann[35], O. Kaufmann[14], M. Kausch[11], I.R. Kenyon[3], S. Kermiche[23], C. Keuker[1], C. Kiesling[26], M. Klein[35], C. Kleinwort[11], G. Knies[11], J.H. Köhne[26], H. Kolanoski[38], S.D. Kolya[22], V. Korbel[11], P. Kostka[35], S.K. Kotelnikov[25], T. Krämerkämper[8], M.W. Krasny[29], H. Krehbiel[11], D. Krücker[26], A. Küpper[34], H. Küster[21], M. Kuhlen[26], T. Kurča[35], B. Laforge[9], R. Lahmann[11], M.P.J. Landon[20], W. Lange[35], U. Langenegger[36], A. Lebedev[25], F. Lehner[11], V. Lemaitre[11], S. Levonian[11], M. Lindstroem[21], B. List[11], G. Lobo[27], V. Lubimov[24], D. Lüke[8,11], L. Lytkin[13], N. Magnussen[34], H. Mahlke-Krüger[11], E. Malinovski[25], R. Maraček[17], P. Marage[4], J. Marks[14], R. Marshall[22], G. Martin[12], H.-U. Martyn[1], J. Martyniak[6], S.J. Maxfield[19], S.J. McMahon[19], T.R. McMahon[19], A. Mehta[5], K. Meier[15], P. Merkel[11], F. Metlica[13], A. Meyer[11], A. Meyer[12], H. Meyer[34], J. Meyer[11], P.-O. Meyer[2], A. Migliori[28], S. Mikocki[6], D. Milstead[11], J. Moeck[26], R. Mohr[26], S. Mohrdieck[12], F. Moreau[28], J.V. Morris[5], E. Mroczko[6], D. Müller[37], K. Müller[11], P. Murín[17], V. Nagovizin[24], B. Naroska[12], Th. Naumann[35], I. Négri[23], P.R. Newman[3], D. Newton[18], H.K. Nguyen[29], T.C. Nicholls[11], F. Niebergall[12], C. Niebuhr[11], Ch. Niedzballa[1], H. Niggli[36], O. Nix[15], G. Nowak[6], T. Nunnemann[13], H. Oberlack[26], J.E. Olsson[11], D. Ozerov[24], P. Palmen[2], E. Panaro[11], A. Panitch[4], C. Pascaud[27], S. Passaggio[36], G.D. Patel[19], H. Pawletta[2], E. Peppel[35], E. Perez[9], J.P. Phillips[19], A. Pieuchot[11], D. Pitzl[36], R. Pöschl[8], G. Pope[7], B. Povh[13], K. Rabbertz[1], P. Reimer[30], B. Reisert[26], H. Rick[11], S. Riess[12], E. Rizvi[11], P. Robmann[37], R. Roosen[4], K. Rosenbauer[1], A. Rostovtsev[24,11], F. Rouse[7], C. Royon[9], S. Rusakov[25], K. Rybicki[6], D.P.C. Sankey[5], P. Schacht[26], J. Scheins[1], S. Schiek[11], S. Schleif[15], P. Schleper[14], D. Schmidt[34], G. Schmidt[11], L. Schoeffel[9], V. Schröder[11], H.-C. Schultz-Coulon[11], B. Schwab[14], F. Sefkow[37], A. Semenov[24], V. Shekelyan[26], I. Sheviakov[25], L.N. Shtarkov[25], G. Siegmon[16], U. Siewert[16], Y. Sirois[28], I.O. Skillicorn[10], T. Sloan[18], P. Smirnov[25], M. Smith[19], V. Solochenko[24], Y. Soloviev[25], A. Specka[28], J. Spiekermann[8], H. Spitzer[12], F. Squinabol[27], P. Steffen[11], R. Steinberg[2], J. Steinhart[12], B. Stella[32], A. Stellberger[15], J. Stiewe[15], U. Straumann[14], W. Struczinski[2], J.P. Sutton[3], M. Swart[15], S. Tapprogge[15], M. Taševský[31],

V. Tchernyshov[24], S. Tchetchelnitski[24], J. Theissen[2], G. Thompson[20], P.D. Thompson[3], N. Tobien[11], R. Todenhagen[13], P. Truöl[37], G. Tsipolitis[36], J. Turnau[6], E. Tzamariudaki[11], S. Udluft[26], A. Usik[25], S. Valkár[31], A. Valkárová[31], C. Vallée[23], P. Van Esch[4], P. Van Mechelen[4], Y. Vazdik[25], G. Villet[9], K. Wacker[8], R. Wallny[14], T. Walter[37], B. Waugh[22], G. Weber[12], M. Weber[15], D. Wegener[8], A. Wegner[26], T. Wengler[14], M. Werner[14], L.R. West[3], S. Wiesand[34], T. Wilksen[11], S. Willard[7], M. Winde[35], G.-G. Winter[11], C. Wittek[12], E. Wittmann[13], M. Wobisch[2], H. Wollatz[11], E. Wünsch[11], J. Žáček[31], J. Zálešák[31], Z. Zhang[27], A. Zhokin[24], P. Zini[29], F. Zomer[27], J. Zsembery[9], and M. zurNedden[37]

[33] Paul Scherrer Institut, 5232 Villigen
[36] Institut für Teilchenphysik, ETH, 8093 Zürich
[37] Physik-Institut der Universität Zürich, 8057 Zürich